

Diagnostic Imaging

NORMAN E. LEEDS, ASHOK J. KUMAR, AND EDWARD F. JACKSON

Magnetic resonance imaging (MRI) performed with and without intravenous (IV) contrast material is the technique of choice for imaging abnormalities of the brain in patients with cancer of the central nervous system (CNS). The technique provides an excellent depiction of anatomic detail in multiple planes and reveals pathologic abnormalities to advantage. The use of an IV contrast medium results in tissue opacification. The major reason for using an IV contrast medium is that it creates a visual distinction between normal brain capillaries and lesions caused by a breakdown in the blood-brain barrier (BBB) or by tumor endothelial cells; these lesions might be present but would otherwise remain invisible. In addition to MRI's visualization of anatomic detail and its ability to detect the presence of pathologic abnormalities, its other advantages are visualization of vascular detail; capability for producing high-resolution images; and use of thin slices to improve anatomic detail, fat saturation for improved tissue visualization, and fast spin-echo and spoiled grass sequences to reduce imaging time. Other techniques for imaging arteries and veins may be added to provide additional anatomic information. Thus, the wide range of pulse sequences and techniques available with MRI make it the ideal imaging technique for most cases.

Computed tomography (CT) still has a role in the evaluation of a patient's CNS cancer. The CT scans are sometimes useful to obtain optimum information on calcification, bony abnormalities, acute hemorrhage, and subarachnoid hemorrhage. Computed tomography is also an excellent modality for examining uncooperative or mobile patients and seriously ill pa-

tients with monitoring equipment and for evaluating subarachnoid spaces and sulci to demonstrate cortical or cerebellar involution.

Magnetic resonance imaging is also advantageous for visualizing the bony structure of the spine, particularly marrow spaces and intraspinal contents, including leptomeninges, pia arachnoid, spinal cord, nerve roots, and ganglia. Use of an IV contrast medium heightens the sensitivity in diagnosis. Magnetic resonance imaging is the technique of choice for demonstrating disease metastatic to osseous structures because it reveals metastasis even when findings from plain roentgenograms of the bone and bone scan are negative. This is possible because MRI visualizes marrow space where metastases can localize, demonstrates seeding of the leptomeninges or pia arachnoid, and may reveal metastases to the spinal cord. Of particular benefit to patients with cord compression, MRI demonstrates to advantage the presence of single or multiple lesions, the site of bony involvement, the extradural component, and the extent of disease, which allows planning of the appropriate therapeutic approach. Thus, by replacing myelography with MRI for lesions affecting the spinal cord, tumor extent and tissue components can be identified within the neoplasm.

Computed tomography scans demonstrate osseous structures to advantage but are not very useful for evaluating intraspinal contents except when contrast medium is introduced into the spinal canal (CT myelography). It is an excellent technique for demonstrating intraspinal pathology, for example, extradural, intradural extramedullary, and intramedullary masses.

Computed tomography myelography will not, however, permit visualization of intraspinal tissue changes except for calcification, fat, or hemorrhage or the presence of a cavity within the central canal (syrinx). Computed tomography or CT myelography is thus a secondary diagnostic option that can be used to obtain complementary information when necessary. CT myelography may be the examination of choice for patients suspected of having cord compression who are unable to undergo MRI.

An MRI examination should not be used for patients who have a pacemaker, paramagnetic aneurysm clips, metal within the orbit, or other paramagnetic devices installed for purposes such as tympanoplasty. The risk that MRI poses to the fetus, especially during the first trimester of pregnancy, is unknown. Most physicians believe, however, that the risk is certainly not as great as that from X-rays; thus, depending on the perceived risk/benefit ratio, MRI may be performed in this setting. The referring physician must recommend this procedure and discuss it with the patient. A signed consent form should be obtained to ensure that the patient has been properly informed of potential risks. After the first trimester, the risk to

the fetus appears to diminish. Nevertheless, the risk/benefit ratio should be explained to the patient, although the probable risks are significantly lessened.

Approximately 10% of CNS cancer patients are claustrophobic, and these patients may need to be sedated before the examination can be performed. The sedative may be sublingual lorazepam in milder cases at a dose of 1.0 to 1.5 mg, depending on patient size, and IV diazepam at a dose of 3 to 5 mg in more severe cases.

This chapter discusses the basic imaging features of brain and spinal cord tumors and is oriented toward the nonspecialist. For a more detailed presentation, the reader is referred to the articles cited in the references.

IMAGING OF PRIMARY BRAIN TUMORS

Cerebral Infiltrating Astrocytomas

Cerebral infiltrating astrocytomas vary from low-grade astrocytomas to high-grade malignant glioblas-

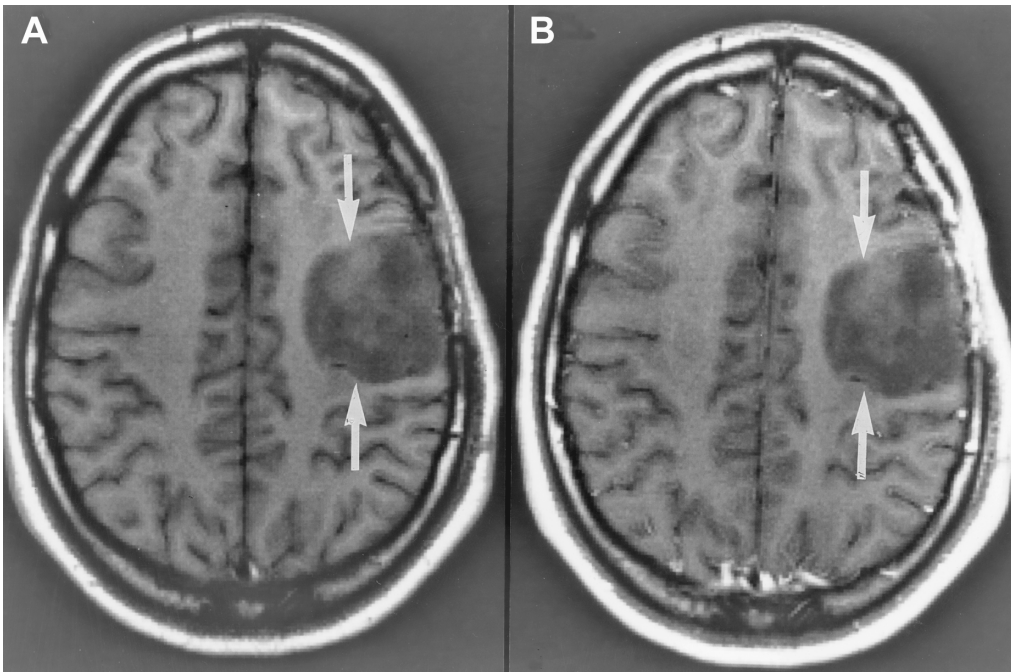


Figure 1-1. Low-grade nonenhancing astrocytoma. Pre-contrast (A) and post-contrast (B) axial MRI images show a nonenhancing tumor (arrows).

toma multiforme. Computed axial tomography and MRI can usually, but not invariably, predict histologic staging of astrocytomas. Low-grade gliomas tend to be nonenhancing to minimally enhancing tumors following the administration of IV contrast material (Fig. 1-1), whereas glioblastoma multiforme shows high-grade heterogeneous enhancement with variable zones of necrosis (Fig. 1-2). Anaplastic astrocytomas, which are graded at an intermediate level, reveal variable degrees of contrast enhancement without necrosis. Brain tumors not only produce multiple neurologic deficits but can also result in symptoms secondary to brain herniations. Occurrences of brain herniations are secondary to occurrences of in-

tracranial masses and associated vasogenic edema within the white matter (Fig. 1-2). MRI, with its multiplanar capability, can easily assess the degree of various types of herniation associated with cerebral tumors (Fig. 1-2). It is important to recognize herniation early because immediate therapy may be necessary to reduce the effect of the mass. The use of glucocorticoids and/or osmotic agents (e.g., mannitol or glycerol) minimizes the degree of edema; likewise, emergency surgical debulking of the tumor may be necessary. Despite aggressive therapy, glioblastoma multiforme can grow like a wildfire, spreading into the ventricular system and subarachnoid space and even metastasizing to the spinal cord

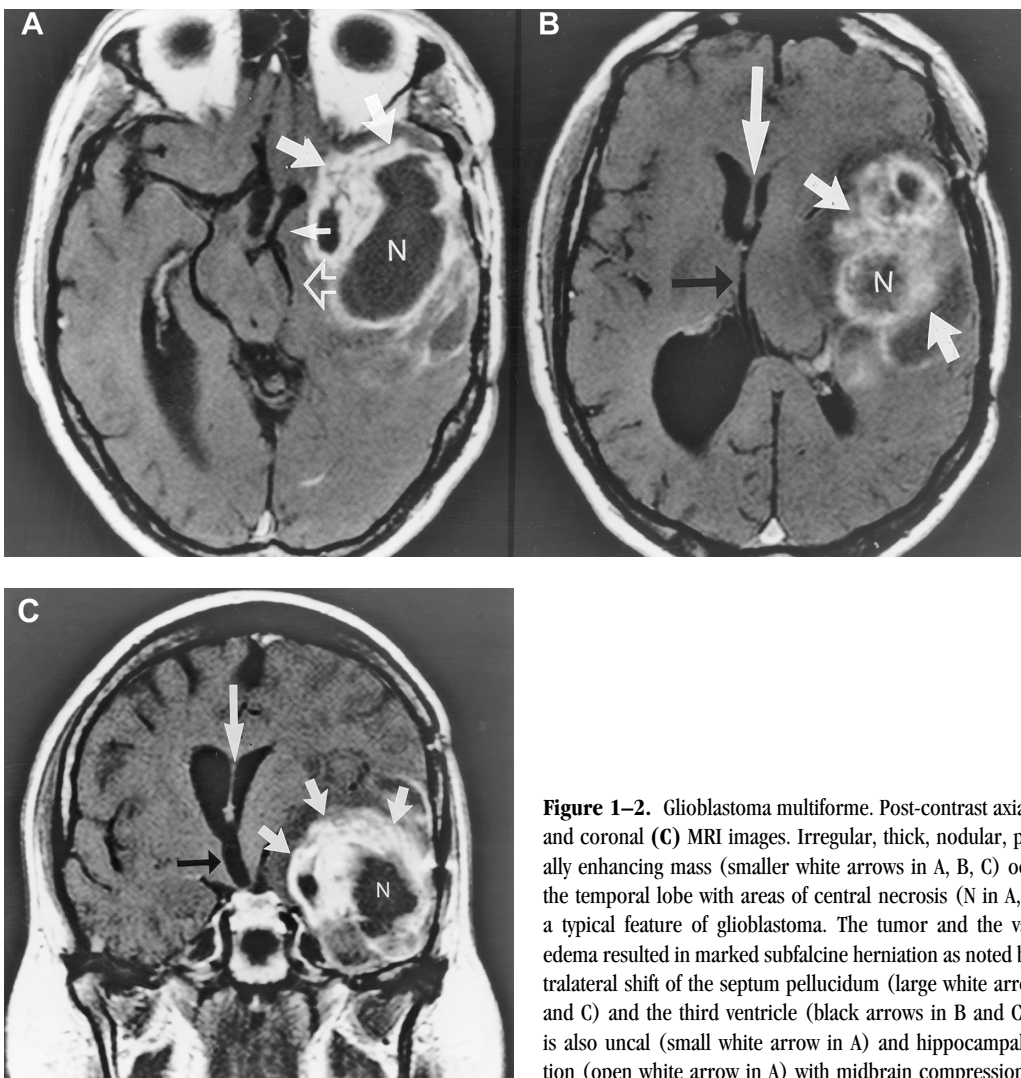


Figure 1-2. Glioblastoma multiforme. Post-contrast axial (A, B) and coronal (C) MRI images. Irregular, thick, nodular, peripherally enhancing mass (smaller white arrows in A, B, C) occupying the temporal lobe with areas of central necrosis (N in A, B, C) is a typical feature of glioblastoma. The tumor and the vasogenic edema resulted in marked subfalcine herniation as noted by a contralateral shift of the septum pellucidum (large white arrows in B and C) and the third ventricle (black arrows in B and C). There is also uncus (small white arrow in A) and hippocampal herniation (open white arrow in A) with midbrain compression.

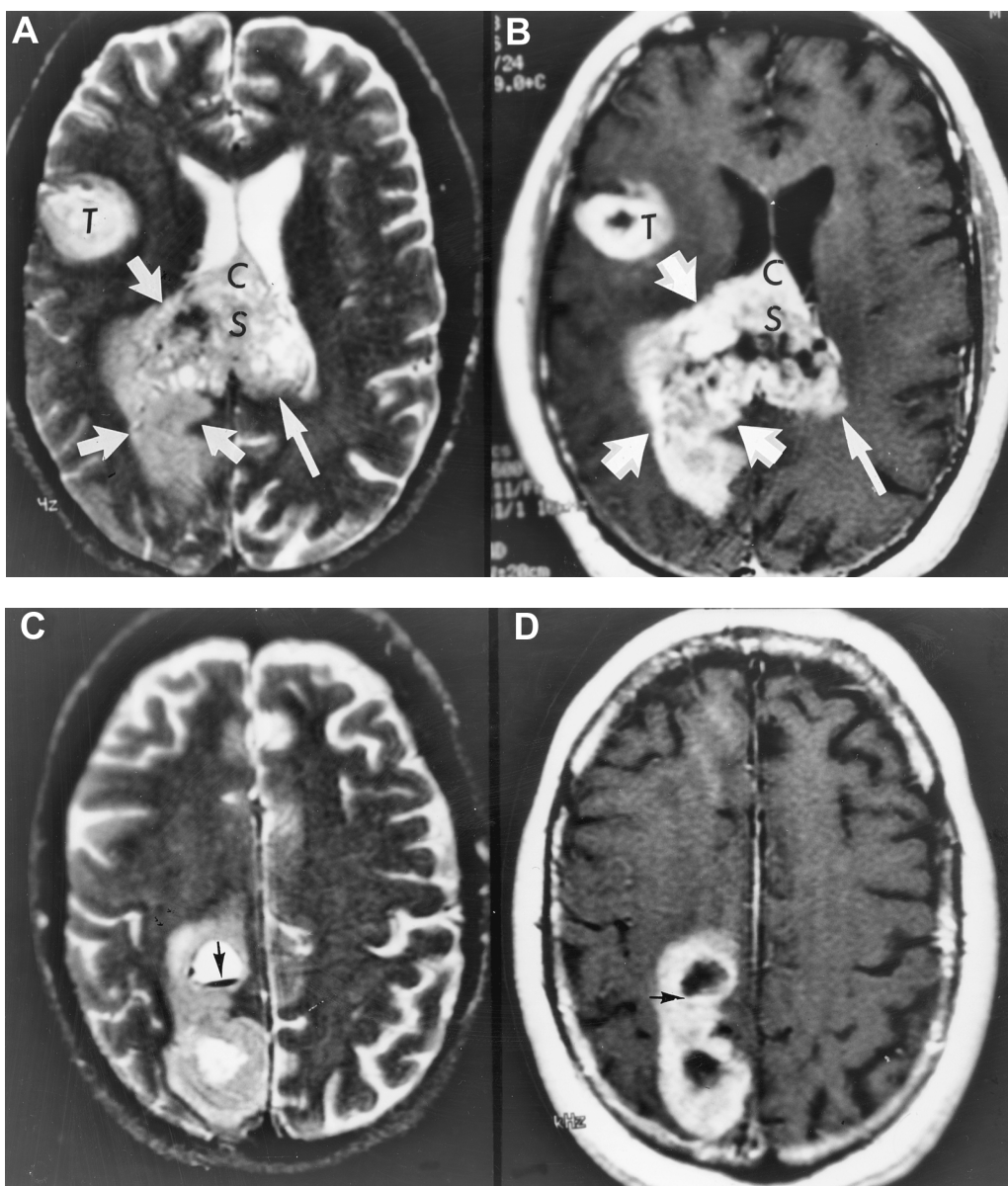


Figure 1-3. Patient with multifocal glioblastoma multiforme. **(A)** T₂-weighted image reveals heterogeneous hyperintensity extending in butterfly fashion from the right parieto-occipital region across the splenium (S) and corpus callosum (C) to the left hemispheres (arrows). Hypointense (dark) foci within the lesion represent intratumoral hemorrhage. A second right frontal focus (T) is seen that probably has transcortical connections to the other lesion despite not being observed. **(B)** Post-contrast T₁-weighted image shows enhancement of the two lesions with a focus of hypointensity within the right frontal convexity lesion not seen in A that represents a focus of necrosis. The hypointense foci within the butterfly lesion probably represent either hemorrhage, as in A, and/or necrotic foci. **(C)** T₂-weighted image through centrum semiovale reveals superior extent of right-sided tumor, which is of heterogeneous hyperintensity with evidence of two round lesions. The more anterior lesion has a fluid level representing a hemorrhagic cavity with sediment that is hypointense (black arrow) with the remainder hyperintense (bright) fluid. The more posterior lesion is round and hyperintense and represents a cystic focus. **(D)** Axial T₁-weighted image post-contrast shows contrast enhancement of the lesion except for the two round foci observed in C that are now hypointense and represent foci of necrosis, with the more anterior hypodense lesion showing reversal of densities from C with sediment now bright (arrow).

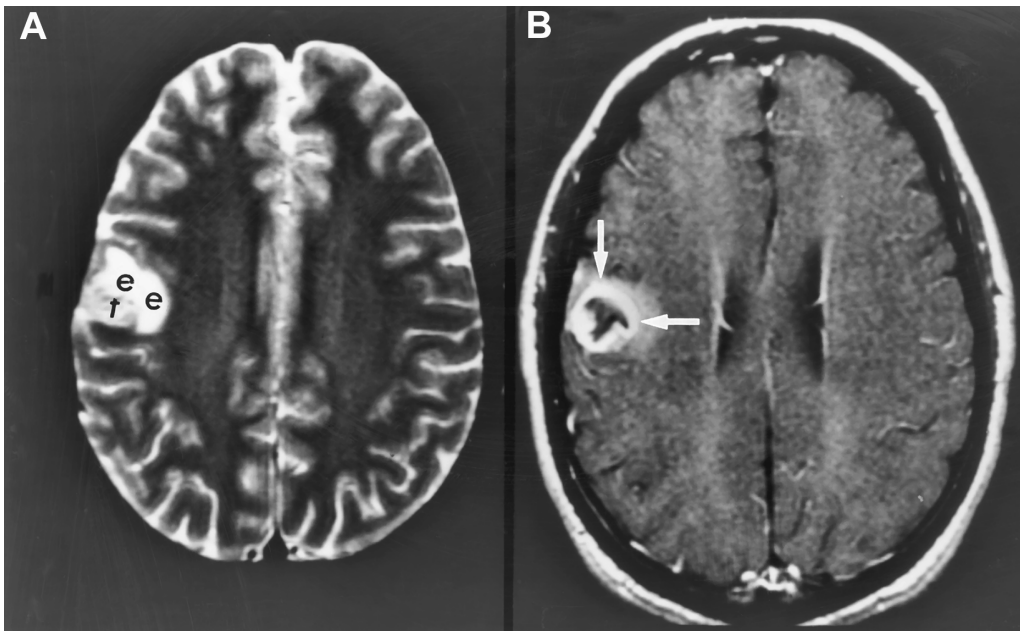


Figure 1-4. Patient with glioblastoma multiforme peripherally situated that looks like metastasis. **(A)** T₂-weighted image reveals peripheral lesion of heterogeneous intensity (t) with surrounding edema (e). **(B)** T₁-weighted image post-contrast shows enhancing peripheral zone (arrows) with central necrosis (hypointensity within tumor).

and spinal subarachnoid space in a relatively short period of time (Choucair et al., 1986; Kyritsis et al., 1993).

When an anaplastic astrocytoma or glioblastoma originates in the corpus callosum, it can extend across the midline to involve the opposite cerebral hemisphere, forming a “butterfly” pattern (Fig. 1-3). Both anaplastic astrocytoma and glioblastoma multiforme can be multifocal in origin (Kyritsis et al., 1993) (Fig. 1-3). Glioblastomas are rarely circumscribed, but on occasion may mimic a metastatic tumor (Fig. 1-4).

Oligodendrogliomas

Oligodendrogliomas are low-grade glial tumors and have a prognosis similar to that of astrocytomas. Oligodendrogliomas are usually slow-growing tumors that elicit chronic symptoms, and patients most often present with seizures. The presence of calcification is a characteristic feature of oligodendrogliomas. Computed tomography is more sensitive than MRI for detecting calcifications. Calcification in a tumor is a use-

ful indicator of the benign nature of the malignant neoplasm. Oligodendrogliomas are sharply demarcated on a cortical surface and show only minimal, if any, enhancement with contrast. As in astrocytomas, various grades may be observed, depending on the degree of anaplasia, vascular endothelial proliferation, and necrosis.

Pilocytic Astrocytomas

Pilocytic astrocytomas are well defined and have a cystic or multicystic component. They usually occur in the suprasellar region, arising from the optic apparatus, and in the posterior fossa. Pilocytic astrocytomas are relatively benign and extremely slow growing. They may be easily removed, depending on their location, because of the presence of a distinct capsule. Thus, they have a relatively favorable prognosis, particularly when located in anatomic areas such as the vermis and the cerebellar hemispheres. Magnetic resonance imaging is more sensitive than CT in differentiating solid from cystic components of pilocytic astrocytomas.

Optic Chiasm and Hypothalamic Astrocytomas

Optic chiasm gliomas are seen most frequently in children and young adults and can occur in association with neurofibromatosis type 1. They are usually low-grade neoplasms that spread along the visual pathways. Hypothalamic gliomas behave more aggressively and produce symptoms earlier, such as diabetes insipidus, inappropriate antidiuretic hormone secretion, or disturbances of temperature, appetite, or metabolism. Frequently, both the optic apparatus and the hypothalamus are affected, and determining the site of origin is difficult.

The specific anatomic structural involvement of optic chiasma/hypothalamic regions by tumor can be best demonstrated by MRI of the sagittal and coronal planes (Fig. 1–5). The tumors are often enhanced with IV contrast medium.

Brain Stem Astrocytoma

Brain stem astrocytomas are more common in children but also occur in adults. Patients usually present with projectile vomiting, ataxia, and multiple cranial nerve palsies. Magnetic resonance imaging is the modality of choice for diagnosing brain stem gliomas, and it can easily detect early tumoral involvement of brain stem and outline the extent of tumor spread. These tumors are known to infiltrate the midbrain, pons, medulla, and upper cervical cord. Grossly enlarged brain stem gliomas can be easily depicted in sagittal views (Fig. 1–6). Brain stem gliomas show variable enhancement with contrast. Magnetic resonance imaging is superior to CT in its ability to clearly differentiate cystic and solid tumor components (Fig. 1–6). A surgical decompression of a cyst can often aid in relieving symptoms caused by compression of vital structures by tumor.

Poorly Differentiated Tumors of Neuronal Cell Origin

Medulloblastomas are tumors that occur in children second in frequency to astrocytomas. They are highly cellular and locally invasive and are best represented in sagittal and axial views of MRI scans. They are characteristically located in the region of the posterior roof of the fourth ventricle. Medulloblastomas are in-

tensely enhanced by IV contrast (Fig. 1–7). These tumors rarely calcify and often seed into the subarachnoid space, ventricular system, and spinal canal.

Intraventricular Tumors

Choroid Plexus Papillomas

Choroid plexus papillomas, which are usually seen in children, originate from the choroid plexus of the lateral ventricles and the fourth ventricle. They account for less than 1% of all intracranial neoplasms.

Magnetic resonance imaging can easily demonstrate the intraventricular location of the mass. Choroid plexus papillomas intensively enhance with IV contrast and are highly vascular. Even when they arise posteriorly in the lateral ventricles with no apparent obstruction, a disproportionate degree of hydrocephalus develops because of overproduction of cerebrospinal fluid (CSF), which is a characteristic feature of choroid plexus papilloma.

Ependymomas

Ependymomas represent about 5% of all primary intracranial gliomas, occurring most frequently in children. They originate from the ependymal lining of the ventricular cavity and are located in the fourth, third, and lateral ventricles. Ependymomas are slow-growing malignant tumors that grow by expansion and infiltration. Ventricular and subarachnoid seeding is common. Magnetic resonance imaging can demonstrate the intraventricular location of the mass (Fig. 1–8). Characteristic imaging features of ependymomas include an intraventricular location, intense enhancement with contrast, and calcification. Ependymomas arising within the fourth ventricular cavity often extend through the foramen of Luschka region into the cerebellopontine angle regions.

Colloid Cysts

Colloid cysts are rare benign tumors that originate from primitive neuroepithelium of the roof of the anterior third ventricle. These tumors are classically located in the foramen of Monro region. Colloid cysts may have a stalk and can cause intermittent hydrocephalus, giving rise to intermittent fainting episodes. Because of the initial location of the mass, tumors as

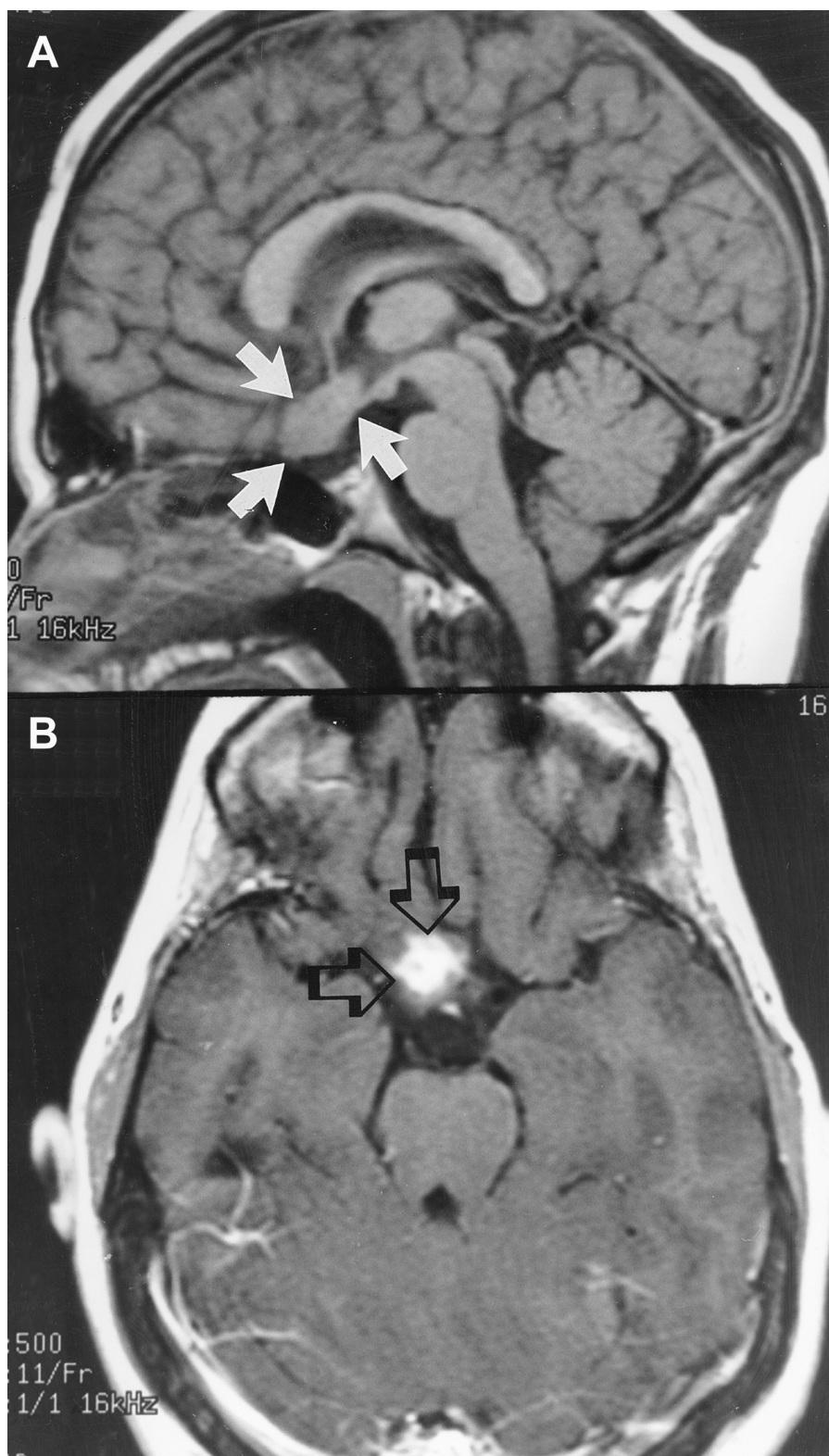


Figure 1-5. Optic chiasma glioma in a patient with neurofibromatosis. Mass involving the optic chiasma (arrows) is clearly shown in a sagittal non-contrast T₁-weighted image of the brain (A). Post-contrast axial T₁-weighted image (B) reveals contrast enhancement (open arrows), a feature of optic chiasma glioma.

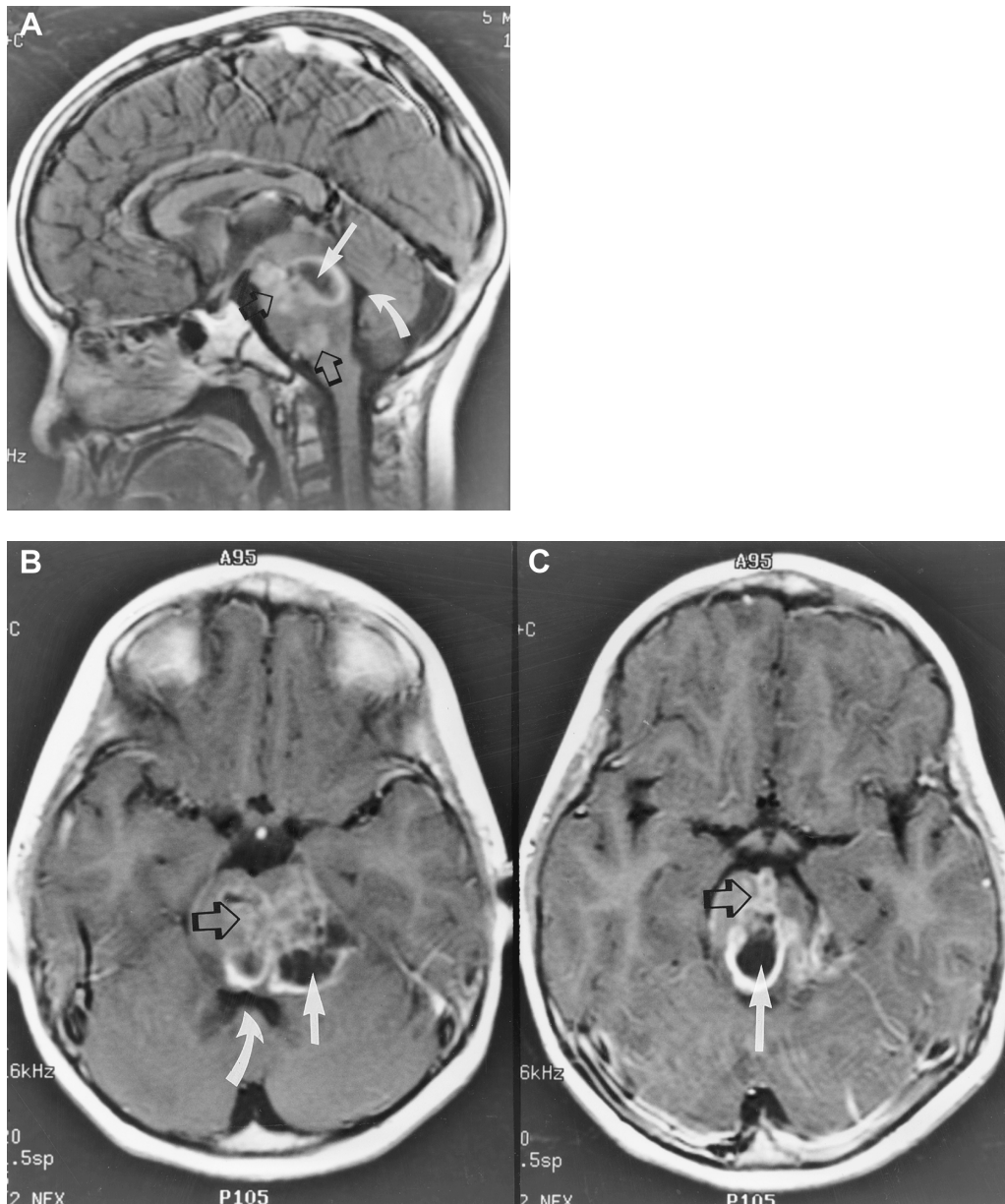


Figure 1-6. Brain stem astrocytoma. Post-contrast sagittal (A) and post-contrast axial MRI scans at the mid (B) and upper (C) pons. The brain stem is markedly expanded by solid (open arrows) and cystic (white arrows) components of tumor. The IV ventricle (curved arrows in A and B) is displaced posteriorly by the brain stem tumor.

small as 1 cm can cause obstructive hydrocephalus. A well-defined nonenhancing mass in the foramen of Monro region should favor the diagnosis of colloid cyst. The diagnosis can be readily made with either CT or MRI.

Subependymal Giant Cell Astrocytomas

Subependymal giant cell astrocytomas involving the lateral ventricles characteristically occur in patients with tuberous sclerosis. These are relatively benign



Figure 1–7. Medulloblastoma. Post-contrast sagittal MRI scan shows the tumor located along the posterior roof of the fourth ventricle (white arrows) with extension to vermis (black arrow) and fourth ventricular (open arrow) areas. The location of the mass and the intense tumoral enhancement are characteristic features of medulloblastoma.

tumors occurring particularly in and around the foramen of Monro region, anterior third ventricle, and frontal horns. These tumors are recognized by their location, intense enhancement on post-contrast CT or MRI examinations, and the presence of calcification (Fig. 1–9).

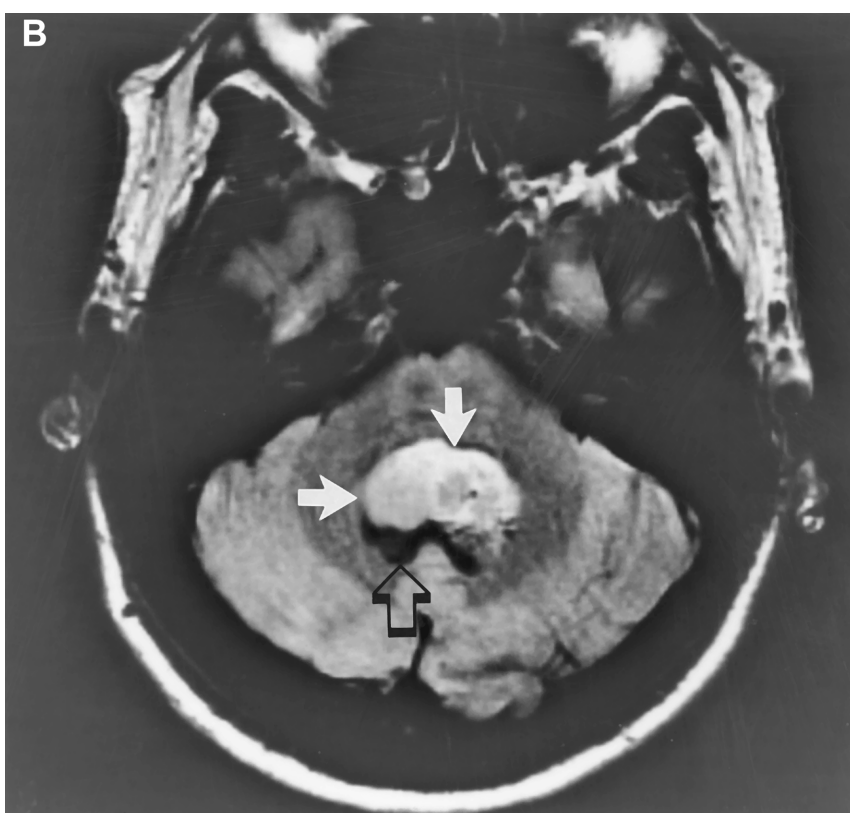
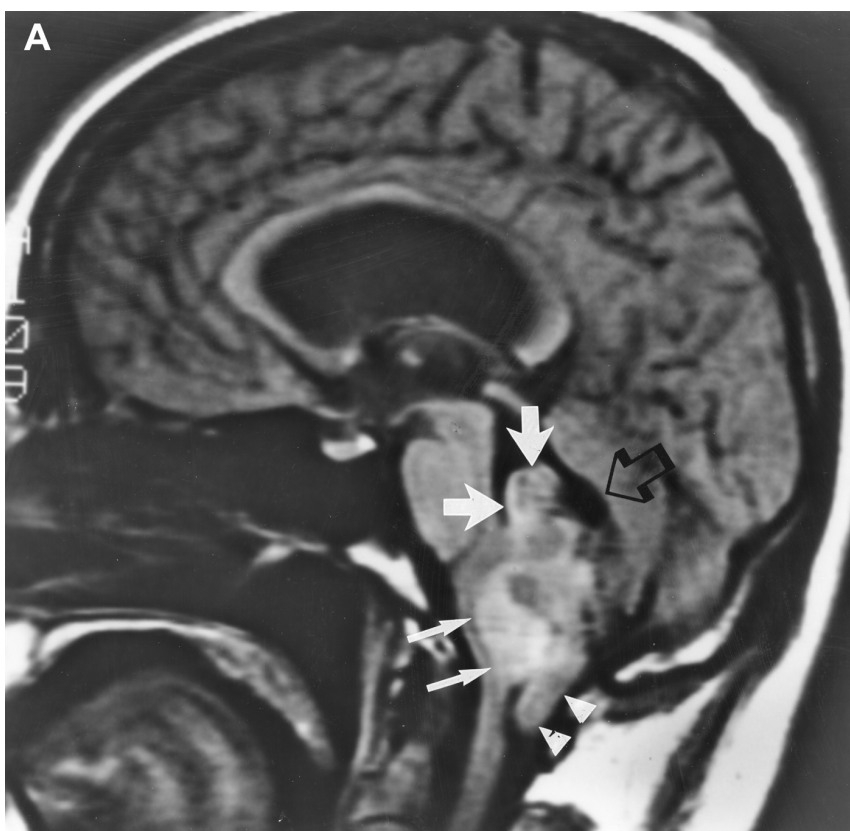
Intrasellar and Suprasellar Tumors

Chromophobe Adenoma

Chromophobe adenomas are the most common intrasellar tumors. They cause the sella to swell into a balloon shape, and they can grow in all directions. Suprasellar extension of the tumor can result in optic nerve and optic chiasma compression, which can cause visual-field defects. The tumors can be easily

diagnosed by MRI examination of the pituitary gland and are best seen in sagittal and coronal planes as soft tissue masses within the sella turcica. Intravenous contrast often results in inhomogeneous enhancement of pituitary tumors (Fig. 1–10).

Other symptoms may develop as a result of hemorrhage or pituitary apoplexy (acute hemorrhage into a pituitary tumor) and may require immediate evaluation to determine the need for surgery. Magnetic resonance imaging is quite sensitive in detecting a hemorrhage into the tumor. When chromophobe adenomas are less than 10 mm in size, they are called *pituitary microadenomas*. Acromegaly and Cushing's syndrome are often caused by microadenomas. Magnetic resonance imaging can detect such tumors as small as 3 mm.



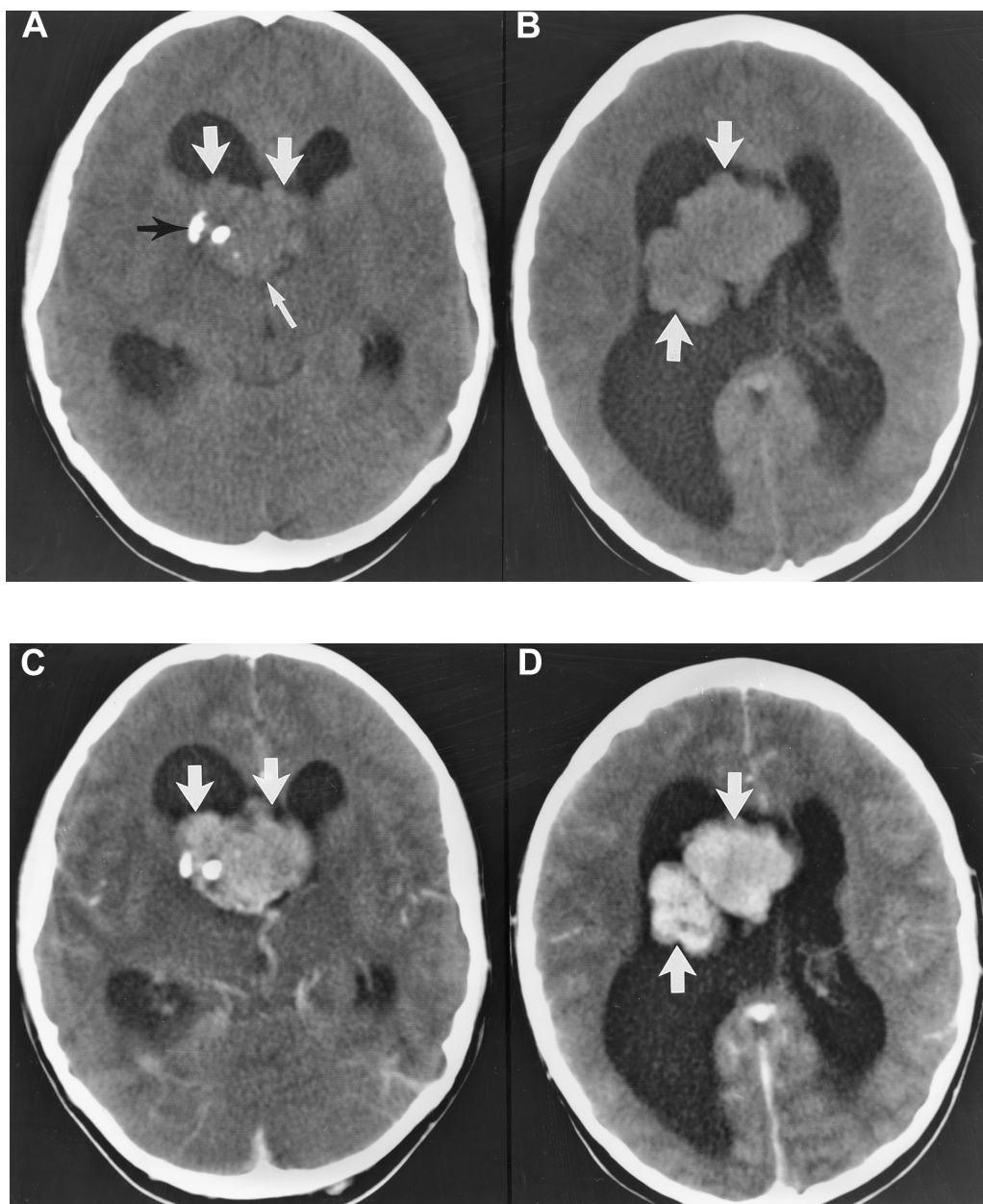


Figure 1-9. An 11-year-old boy with tuberous sclerosis and with intraventricular masses (subependymal giant cell astrocytoma). **(A,B)** Non-contrast CT of the brain. Dense mass with calcifications (black arrow in A) is shown occupying the frontal horns and body of lateral ventricles (arrows) extending down to the foramen of Monro region (small arrow in A). **(C,D)** Intravenous contrast CT of the brain. Enhancing features of the tumor (arrows) are revealed in post-contrast images.

←

Figure 1-8. Ependymoma of the fourth ventricle. Post-contrast sagittal **(A)** and axial **(B)** MRI views. Intraventricular enhancing mass (large arrows) with invasion of medulla (small arrows in A) is clearly depicted by MRI. The mass has produced a tonsillar herniation (arrowheads in A). The fourth ventricle (open arrow) is expanded by the mass.

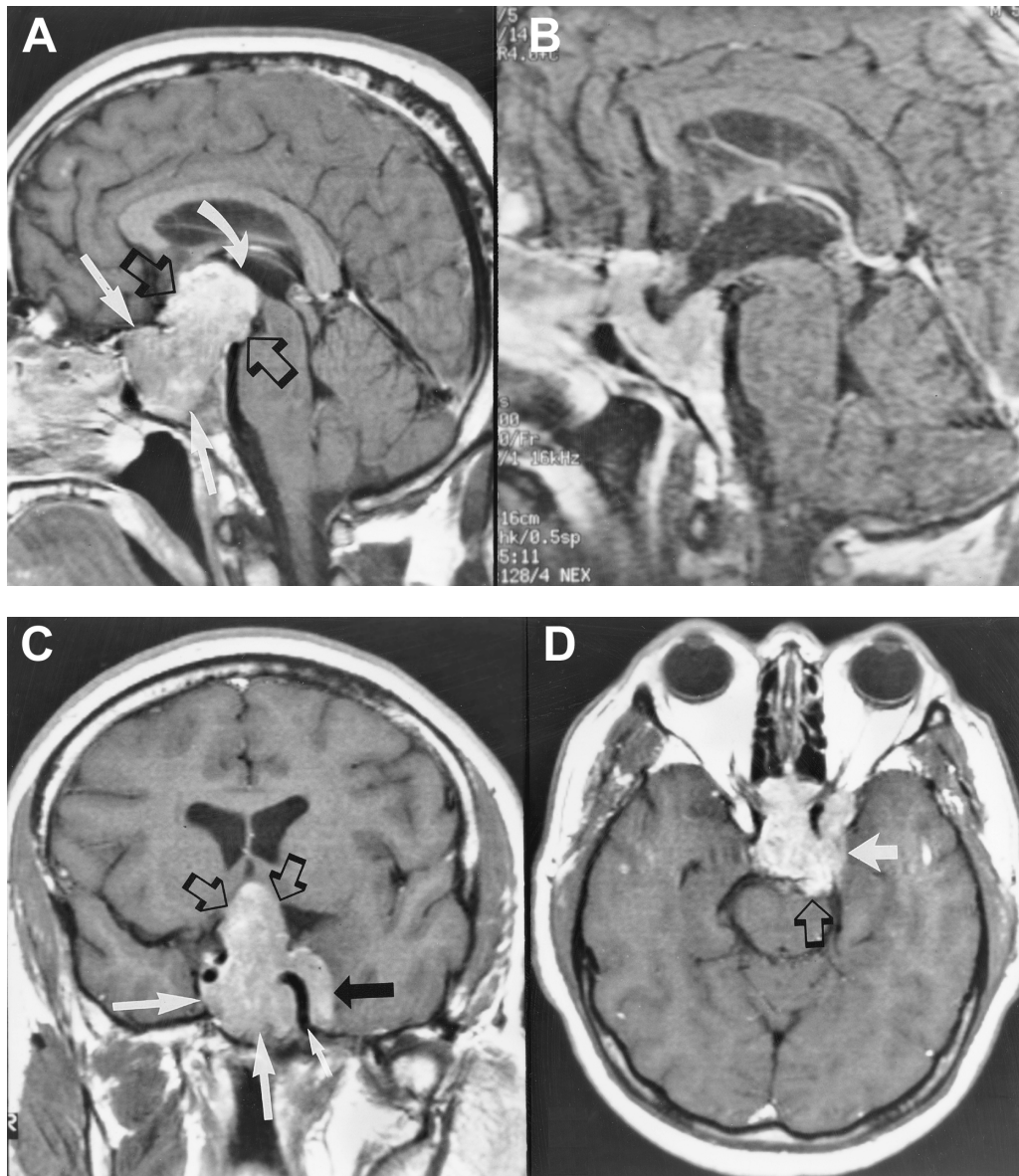


Figure 1-10. Pituitary adenoma (prolactinoma). Post-contrast sagittal MRI scans, pre-bromocriptine (**A**) and post-bromocriptine (**B**) therapy. There is a very large intrasellar mass (arrows) with a suprasellar extension (open arrows) compressing the optic chiasma and anterior third ventricle (curved arrow) as shown in **A**. A dramatic decrease in suprasellar and intrasellar tumor followed bromocriptine therapy (**B**). Post-contrast coronal MRI of the pituitary (before therapy; **C**) reveals the intrasellar mass (large white arrows) and the suprasellar extension (open arrows). The tumor extension to the cavernous sinus (black arrow) and the relationship of the tumor to the internal carotid artery (small arrow) are best demonstrated in this projection. Post-contrast axial MRI of the brain (before therapy; **D**) shows the parasellar (arrow) and posterior fossa (open arrow) extension of the tumor.

Craniopharyngiomas

Craniopharyngiomas originate from the epithelial remnants of Rathke's pouch at the junction of the infundibulum and the pituitary gland. They are the most

common suprasellar tumors in young children. They can also occur in adults in the fifth decade of life. Characteristic imaging features of craniopharyngioma include suprasellar location, tumor containing solid and cystic components, and calcifications.

tions occur in 80% of childhood craniopharyngiomas. Solid portions of the tumor enhance with IV contrast medium.

Pineal Region Tumors

Pineal region tumors are uncommon neoplasms that account for less than 1% of all intracranial tumors. Tumors that occur in this location include germ cell tumors (germinoma, choriocarcinoma, teratoma) and pineal parenchymal tumors (pinealoblastoma, pinealocytoma).

Germinomas

Germinomas are the least differentiated germ cell tumor, occurring predominantly in men (boys and young adult men) and accounting for 50% of all pineal region tumors. Features of these tumors are calcifications and intense enhancement with IV contrast. Germinomas are readily diagnosed by CT or MRI examination (Fig. 1–11). The diagnosis of germinoma is important therapeutically because the tumor is extremely sensitive to radiation and can “melt away” with radiotherapy. Subependymal spread as well as leptomeningeal seeding may occur with germinomas.

Pinealoblastomas and Pinealocytomas

Pinealoblastomas and pinealocytomas are embryonal tumors that arise from neuroepithelial cells of the pineal gland. Pinealoblastoma is a highly aggressive, infiltrative tumor composed of poorly differentiating cells. They occur in children and have a poor prognosis due to subarachnoid metastatic tumor seeding. Pinealocytomas occur in adults. They are well defined, less infiltrative, and less cellular than pinealoblastomas.

Tumors of the Cranial Nerves

Vestibular Schwannomas

Vestibular schwannomas are also called *acoustic neurinoma* and are the most common cranial nerve sheath neoplasm. Vestibular schwannomas, the most commonly occurring cerebellopontine angle tumors, originate from the VIIIth cranial nerve. Sensorineural hearing loss and dizziness are the most common presenting complaints. Magnetic resonance imaging can differentiate acoustic nerve sheath tumors from other masses that may occur in this location, such as meningioma, arachnoid cysts, and epidermoid tumors. Tumors as small as 3 to 4 mm that arise within the internal auditory canal (intracanalicular tumors)

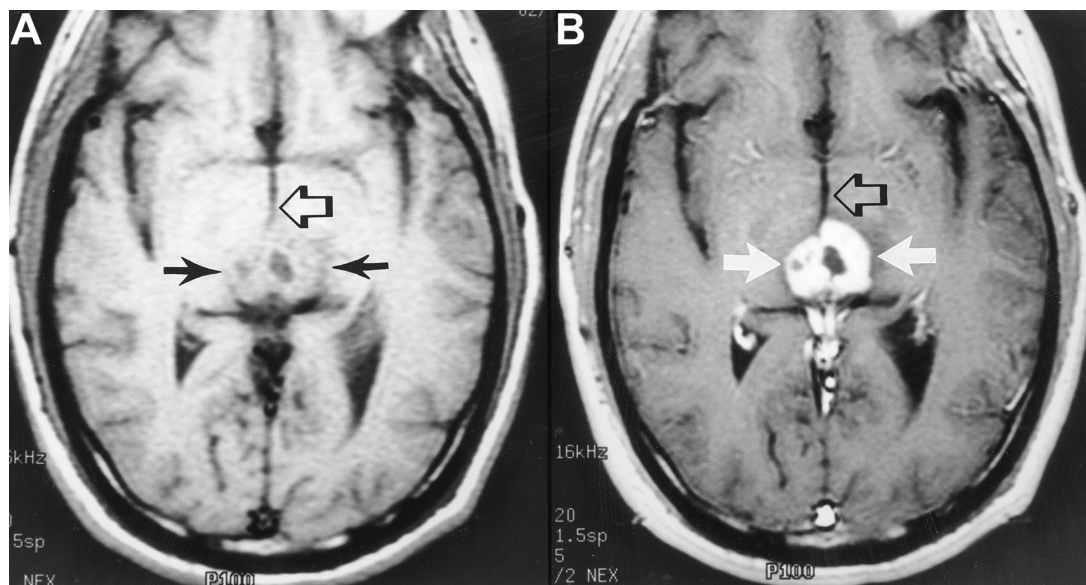


Figure 1–11. Pineal mass (germinoma). Pre-contrast (A) and post-contrast (B) MRI scans reveal enhancing posterior third ventricular and pineal region mass (arrows) produced by pathologically proven germinoma. Open arrows in A and B point to the anterior portion of the third ventricle.



Figure 1–12. Vestibular schwannoma. Post-contrast axial MRI scan shows an enhancing right cerebellopontine angle, partially cystic, mass (arrows) with extension into internal auditory canal (open arrow) in a patient with hearing loss.

can be recognized by MRI due to their contrast-enhancing features (Fig. 1–12). Large acoustic nerve sheath tumors may give rise to symptoms related to brain stem compression.

Trigeminal Schwannoma

Trigeminal schwannomas are recognized by their location in the region of the trigeminal ganglion and its major branches. They occur in and around the region of petrous apex and in the parasellar region, presenting in a dumbbell-like fashion in both the posterior and middle fossae. Trigeminal nerve irritation by tumors can give rise to tic douloureux. Trigeminal neurinoma can be readily diagnosed by CT or MRI examinations by their enhancing features and their

location along the path of the trigeminal nerve and its branches (Fig. 1–13).

Tumors of the Reticuloendothelial System

Primary lymphoma of the brain is rare, occurring in less than 1% of intracranial tumors and usually in individuals in the fifth and sixth decades of life. Primary CNS lymphomas occur in the basal ganglia, hypothalamus, corpus callosum, septum pellucidum, and paraventricular regions. Following injection of an IV contrast medium, the tumors show intense homogeneous enhancement on CT and MRI scans (Fig. 1–14). Cerebral lymphomas are radiosensitive tumors and can disappear after radiotherapy. In some

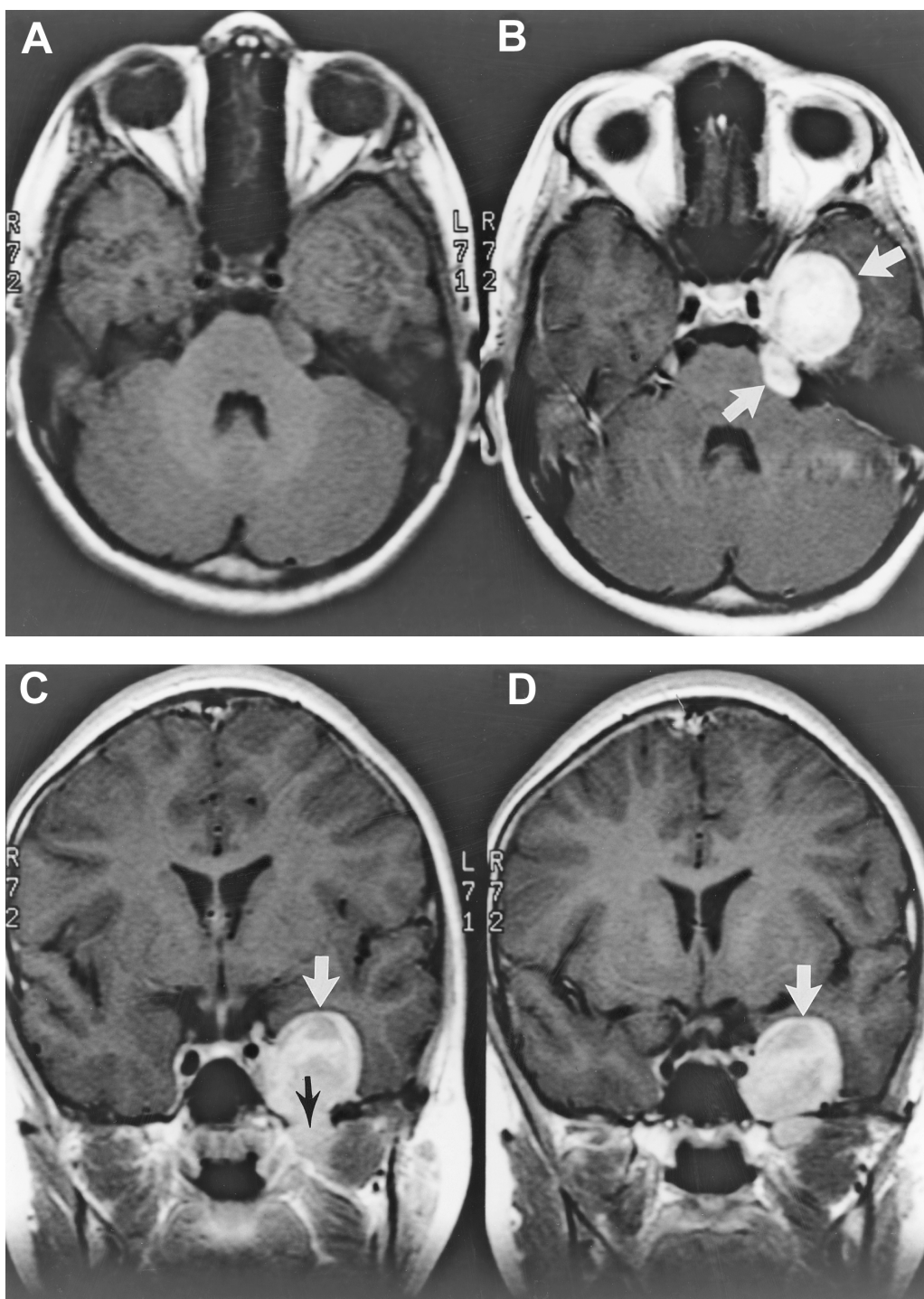


Figure 1-13. Trigeminal schwannoma. Pre-contrast axial (A), post-contrast axial (B), and coronal (C,D) MRI scans. A well-defined enhancing mass (arrows in B, C, and D) is seen along the course of the trigeminal nerve. A small portion of the tumor projects below the skull base enlarging the foramen ovale (black arrow in C).

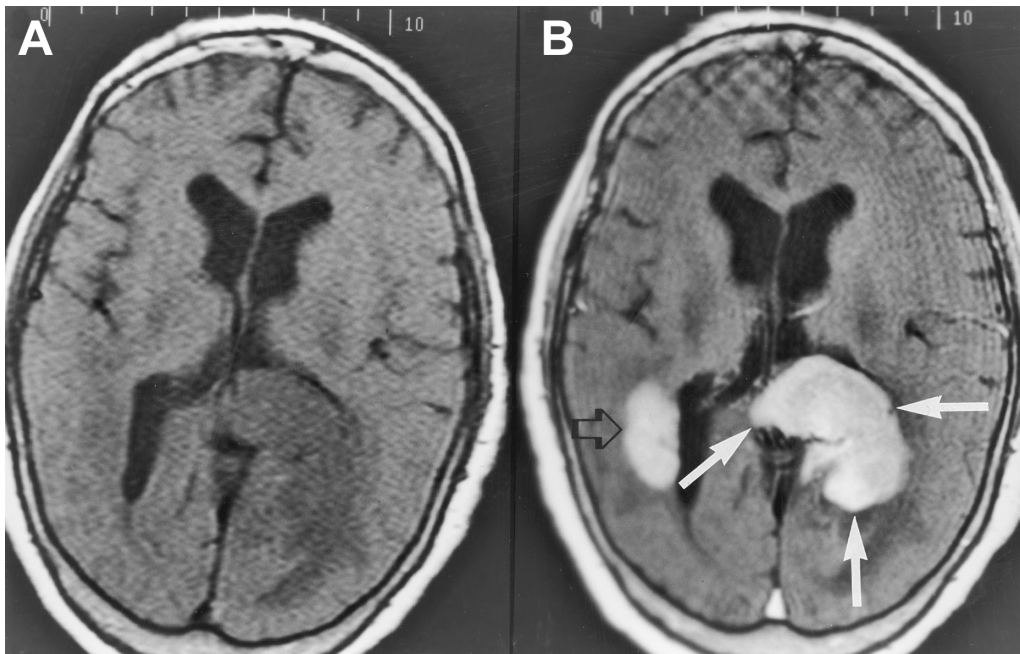


Figure 1-14. Primary lymphoma of the brain. Non-contrast (**A**) and post-contrast (**B**) MRI scans at the level of the lateral ventricles. An enhancing mass involving the splenium of the corpus callosum (arrows) and right paraventricular region (open arrow) is shown. The location of the mass and the homogeneous enhancement of tumor are commonly seen in lymphoma.

instances, glucocorticoids alone are sufficient to reverse the vascular permeability of the tumor and lyse tumor cells. Imaging features of metastatic lymphoma of the brain secondary to systemic lymphoma are similar to those of primary lymphoma, and calvarial and meningeal involvements are frequently observed.

Tumors of Developmental Origin

Lipoma, epidermoid tumors, dermoid tumors, and teratomas are tumors of developmental origin that may occur intracranially, collectively accounting for about 1% of all intracranial tumors.

Epidermoid Tumors

Epidermoid tumors result from the inclusion of ectodermal elements during closure of the neural tube between the third and fifth weeks of gestation. They commonly occur in the cerebellopontine angle cisterns, in the suprasellar region, and within the ventricles, pineal region, and spinal canal. Epidermoid tumors are nonenhancing on CT and MRI examina-

tion but may reveal slight signal increase on proton-weighted and T₂-weighted images (Fig. 1-15). Epidermoid tumors in the cerebellopontine angle region can cause irritation of the trigeminal nerve, and patients may present with tic douloureux.

Dermoid Tumors

Dermoid tumors are infrequently occurring lesions that result from inclusion of epithelial cells and skin appendages (e.g., hair follicles, sebaceous glands, and sweat glands) during closure of the neural tube. They occur within the midline and often contain calcifications and fatty tissue. These tumors can rupture, with spillage of fatty contents into the ventricular cavity and subarachnoid spaces (Fig. 1-16).

Teratomas

Teratomas contain elements of ectodermal, endodermal, and mesodermal germ cells. They are rare and occur in the pineal, anterior third ventricular, and sellar regions.



Figure 1–15. Epidermoid tumor. The tumor is in the left cerebellopontine angle region in a patient presenting with acute tic douloureux. Proton-weighted MRI scan reveals hyperintense mass (arrow).

Lipomas

Lipomas are fatty tissue tumors that are considered an incidental finding and are located in the quadrigeminal plate cistern (Fig. 1–17), suprasellar cistern, and cerebellopontine angle cisterns. The fatty tissue has a unique signal characteristic, as demonstrated by MRI examination, and thus can be easily distinguished from other tumors.

Tumors of Blood Vessel Origin

Hemangioblastomas

Hemangioblastomas contain proliferative blood vessels or hemangioblasts and occur in the third and fourth decades of life. They often have cystic and solid components with a mural nodule. Magnetic resonance imaging can clearly identify the cystic component of tumor and the solid mural nodule that are

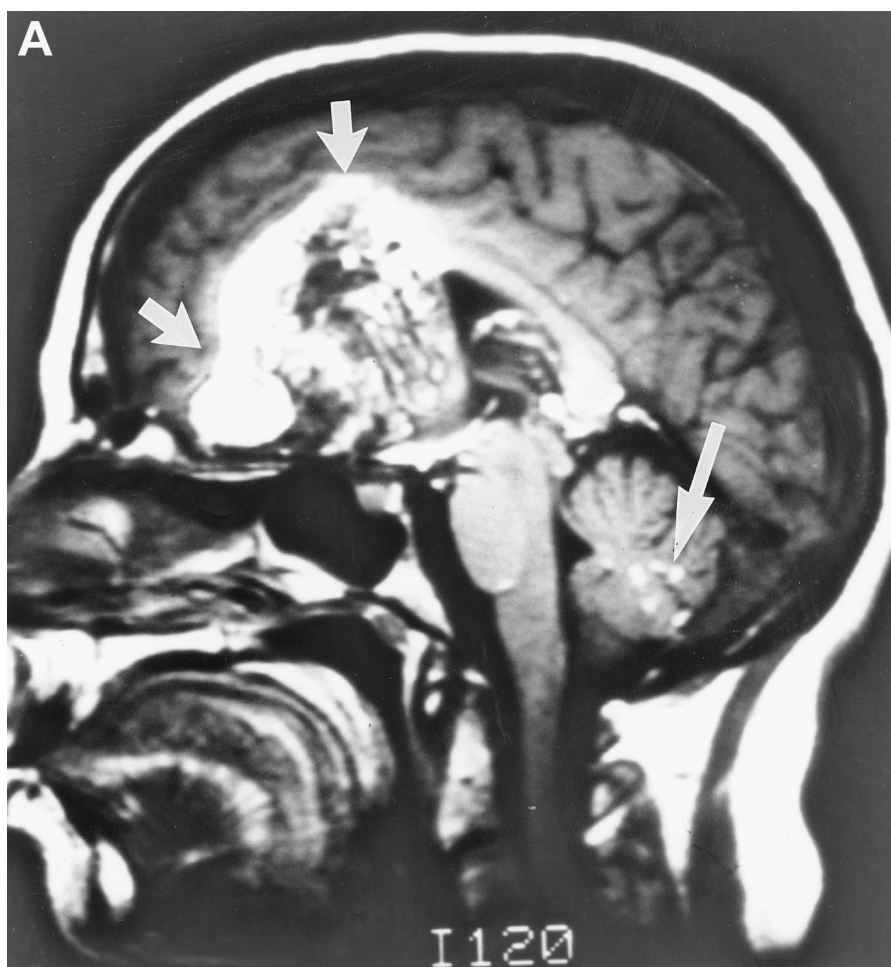


Figure 1-16. Dermoid cyst. Sagittal T₁-weighted images of the brain (A,B). Huge frontal lobe dermoid cyst (arrows) with fatty tumor rupturing into the ventricular cavity with fat-CSF level (fat, small white arrow; CSF, black arrow in B) and into the subarachnoid space of the posterior fossa (large arrow in A). (*continued*)

enhanced strikingly with a contrast medium. Hemangioblastomas are highly vascular tumors, and a vascular nodule can be readily identified by angiography. Hemangioblastomas may be observed in younger patients with von Hippel-Lindau disease, a familial disorder that is composed of angiomatosis retinae and pancreatic cysts and that can result in renal cell carcinoma. Hemangioblastomas often occur as multiple lesions. Cerebral angiography may be required to confirm their diagnosis even if only a solitary lesion has been identified on CT or MRI examination.

Cavernous Angiomas

Cavernous angiomas can present as an intracranial mass and may mimic a neoplasm. These lesions often contain blood, and MRI signal characteristics are able to differentiate old blood from new areas of hemorrhage. These malformations also contain calcifications. Unlike primary gliomas and metastases, cavernous angiomas do not grow rapidly, and follow-up examinations may be useful in differentiating cavernous angiomas from neoplasms. They also do not

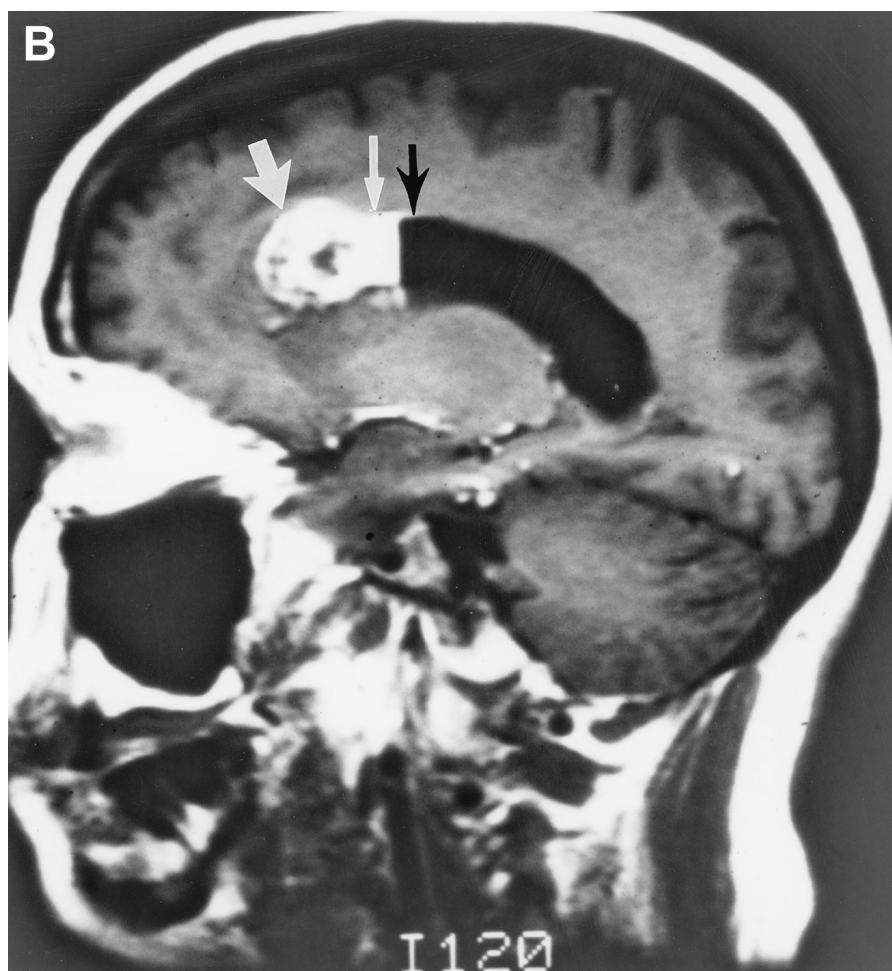


Figure 1-16. (Continued)

usually show contrast enhancement and frequently occur as multiple lesions.

Tumors of Mesodermal Origin

Meningiomas

Meningiomas account for 15% of all intracranial tumors and are the most common type of extra-axial benign neoplasm. They originate from the dura or arachnoid and occur in middle-aged adults. The tumors grow slowly and may be present for years before symptoms are evident. Meningiomas commonly occur in the parasagittal region; over the cortex, sphenoid wings, parasellar region, and cerebello-pontine angle; and from the tentorium.

Meningiomas can be easily recognized on CT scans. In non-contrast CT, meningiomas appear dense, and in post-contrast images, intense enhancement is evident. The tumors also frequently contain calcification and induce reactive hyperostosis of adjacent bone, which is a characteristic feature of meningioma. Magnetic resonance imaging is also sensitive in detecting meningiomas (Fig. 1-18). The extra-axial nature of the meningioma can be easily depicted by MRI examination. Meningiomas are highly vascular and demonstrate homogeneous tumor blush on angiography. A meningeal reaction (meningeal tag) is often observed and may be secondary to tumor involvement or a reaction to the presence of the neoplasm.



Figure 1–17. An incidental lipoma of the brain. Non-contrast axial MRI of the brain at the level of the midbrain. A bright signal intensity mass (arrow) is seen posterior to the midbrain within the quadrigeminal plate cistern, producing no mass effect. Note that the signal intensity of the mass is similar to that in subcutaneous fatty tissue of the calvarium (arrow) in this T₁-weighted pulse sequence. The mass also behaved like the signal intensity of fat in a T₂-weighted pulse sequence. The lesion did not enhance with contrast.

IMAGING OF SPINAL CORD TUMORS

Intramedullary Primary Tumors

Astrocytomas

Astrocytomas represent 40% of spinal cord neoplasms. Astrocytomas in the spinal cord are often less malignant than those that occur within the brain. Small cord astrocytomas occur most often in patients between 30 and 40 years of age. The usual clinical symptoms are spasticity, stiffness in the legs, sensory changes, and urinary incontinence.

Magnetic resonance imaging is extremely sensitive in the detection of primary spinal cord neoplasms. Combined sagittal and axial post-contrast images with gadopentetic acid clearly outline the intramedullary location of the tumor, which is enhanced following

administration of an IV contrast medium (Fig. 1–19). Magnetic resonance imaging is also useful in differentiating the solid from the cystic components of this tumor. These neoplasms are often infiltrating with poorly defined margins. In addition, cystic components are common above, below, or within the neoplasm. Approximately 75% of the lesions occur at the thoracic and cervical levels. Lumbar lesions are uncommon.

Ependymomas

Ependymomas are slow-growing, benign neoplasms that arise from the ependymal cells in the central canal or in ependymal rests that are present in the filum terminale. Ependymomas represent 60% to 70% of spinal cord tumors. They typically occur between the third and sixth decades of life. They are fre-

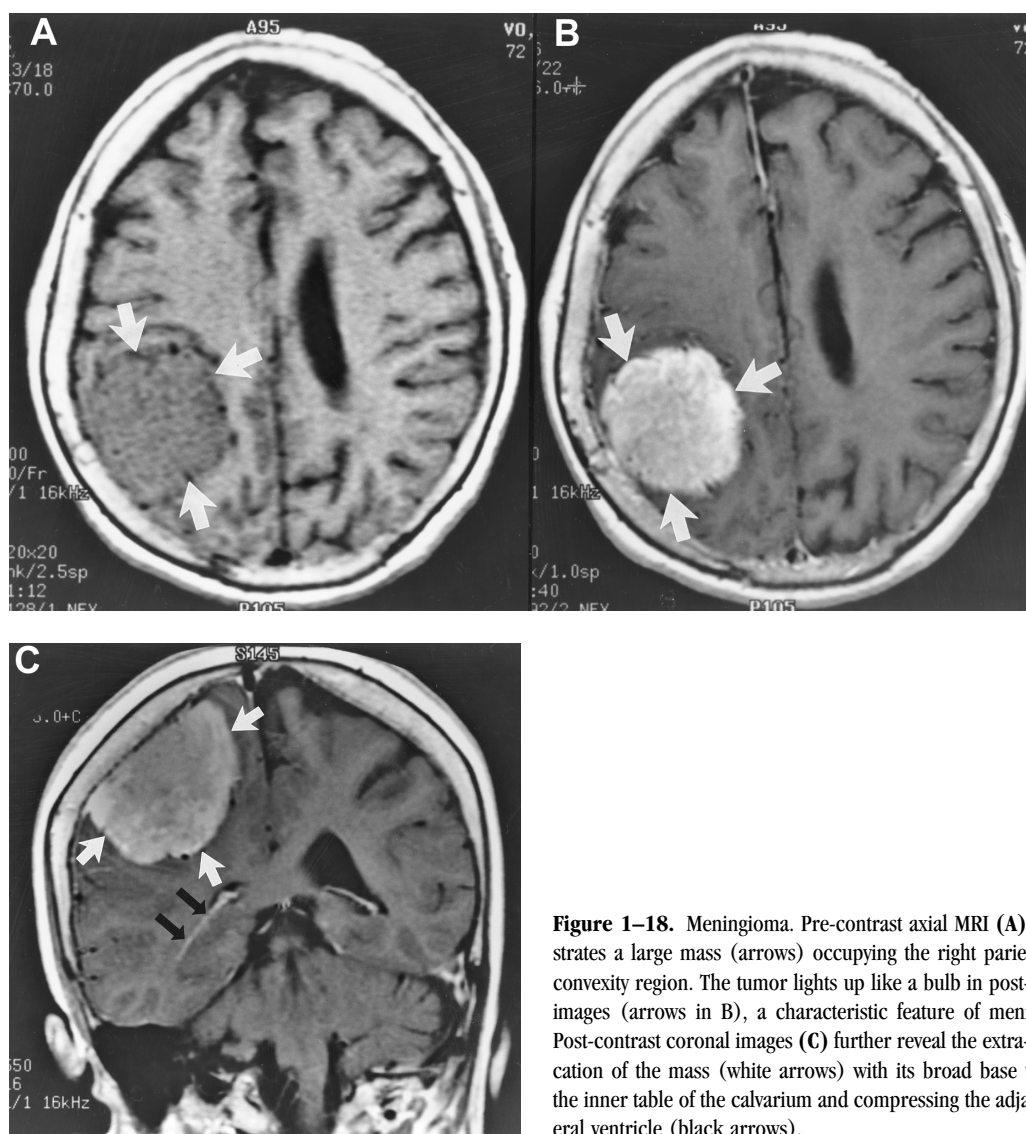


Figure 1-18. Meningioma. Pre-contrast axial MRI (A) demonstrates a large mass (arrows) occupying the right parietal high-convexity region. The tumor lights up like a bulb in post-contrast images (arrows in B), a characteristic feature of meningioma. Post-contrast coronal images (C) further reveal the extra-axial location of the mass (white arrows) with its broad base touching the inner table of the calvarium and compressing the adjacent lateral ventricle (black arrows).

quently well circumscribed, surgically resectable, and potentially curable. Ependymomas may occur anywhere in the spinal cord. Sixty percent commonly occur within the cauda equina or filum terminale. Contrast-enhanced MRI scans clearly outline these tumors (Fig. 1-20).

Hemangioblastomas

Hemangioblastoma, as described previously, is a benign tumor that originates from endothelial cells. The

tumor, composed of a dense network of capillary and sinus channels, may present as a solitary lesion or as multiple tumors and is associated with von Hippel-Lindau disease in young patients. Patients with this disorder have angiomas of the retina and pancreatic cysts and may develop renal cell carcinoma. Hemangioblastomas characteristically have a cystic component with a mural nodule. Magnetic resonance imaging is useful in identifying the cystic component of the tumor and the mural nodule, which intensely enhances with contrast.

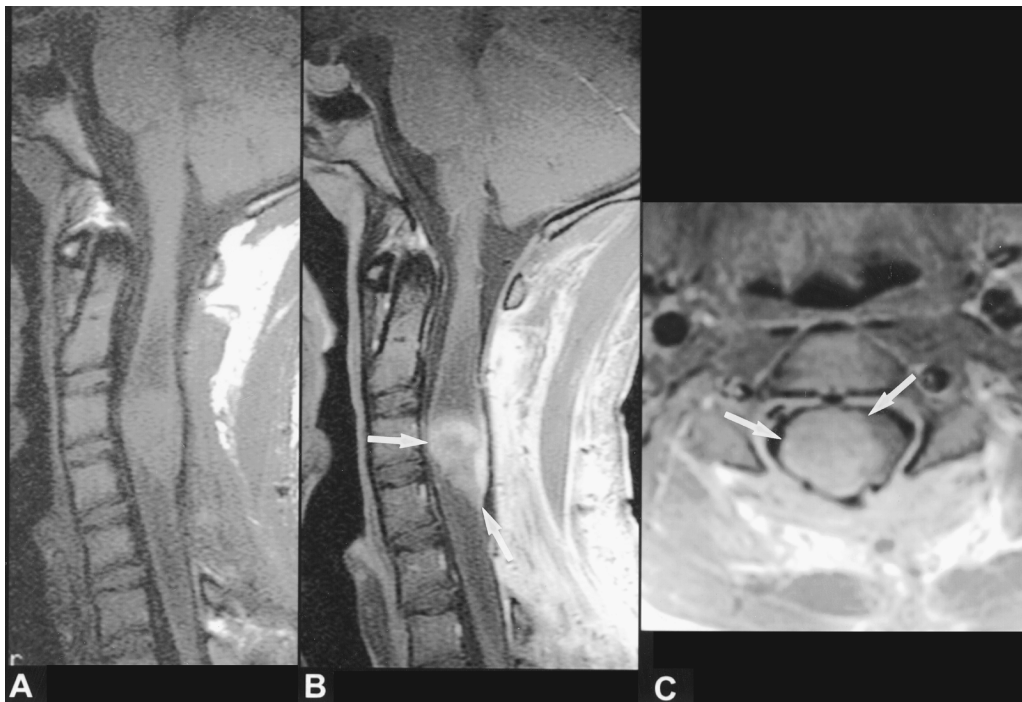


Figure 1-19. Astrocytoma of the cervical cord. Pre-contrast (A) and post-contrast (B) sagittal and axial (C) T₁-weighted images of the cervical cord show enhancing intramedullary tumor (arrows in B and C).

Intramedullary Spinal Cord Metastasis

Metastasis to the spinal cord is a rare occurrence, observed in 1% to 3% of patients with tumors. Common systemic tumors are lung and breast cancers. Melanoma and lymphoma can also metastasize to the spinal cord. Tumors metastasize to the spinal cord via the hematogenous route and by leptomeningeal tumor spread with penetration into the spinal cord. Leptomeningeal tumors are pathologically characterized by sheets of tumor cells coating the leptomeninges (Fig. 1-21). The clinical presentation includes backache, plexopathy, myelopathy, and cranial nerve defects. The most common primary CNS tumors are glioblastoma multiforme, ependymoma, and medulloblastoma. Dissemination is typically via the subarachnoid space and, less often, via the central canal.

Post-contrast MRI scans reveal solitary and multiple metastatic sites that are seen as enhancing nodules or linear bands reflecting pial involvement (Fig. 1-22). Leptomeningeal tumor infiltration is readily recognized in the entire subarachnoid space, although it is more common in the lumbar area. Infil-

tration is identified by the presence of enhancing tumor nodules, matting, and irregular nodular thickening of nerve roots.

Intradural Extramedullary Tumors

Meningiomas

Meningiomas occur most commonly in females and in adults, with a peak incidence at 45 years. They often occur in the thoracic spinal canal. On post-contrast MRI scans, meningiomas are clearly visualized as a homogeneously enhancing intradural mass that is usually situated dorsally. The extent of cord compression by these tumors can be readily evaluated through MRI scanning.

Schwannomas

Schwannomas (neurinomas) are benign nerve sheath tumors that usually originate from the sensory nerve roots. Neurinomas predominantly occur in males. Intraspinous neurinomas can protrude into the

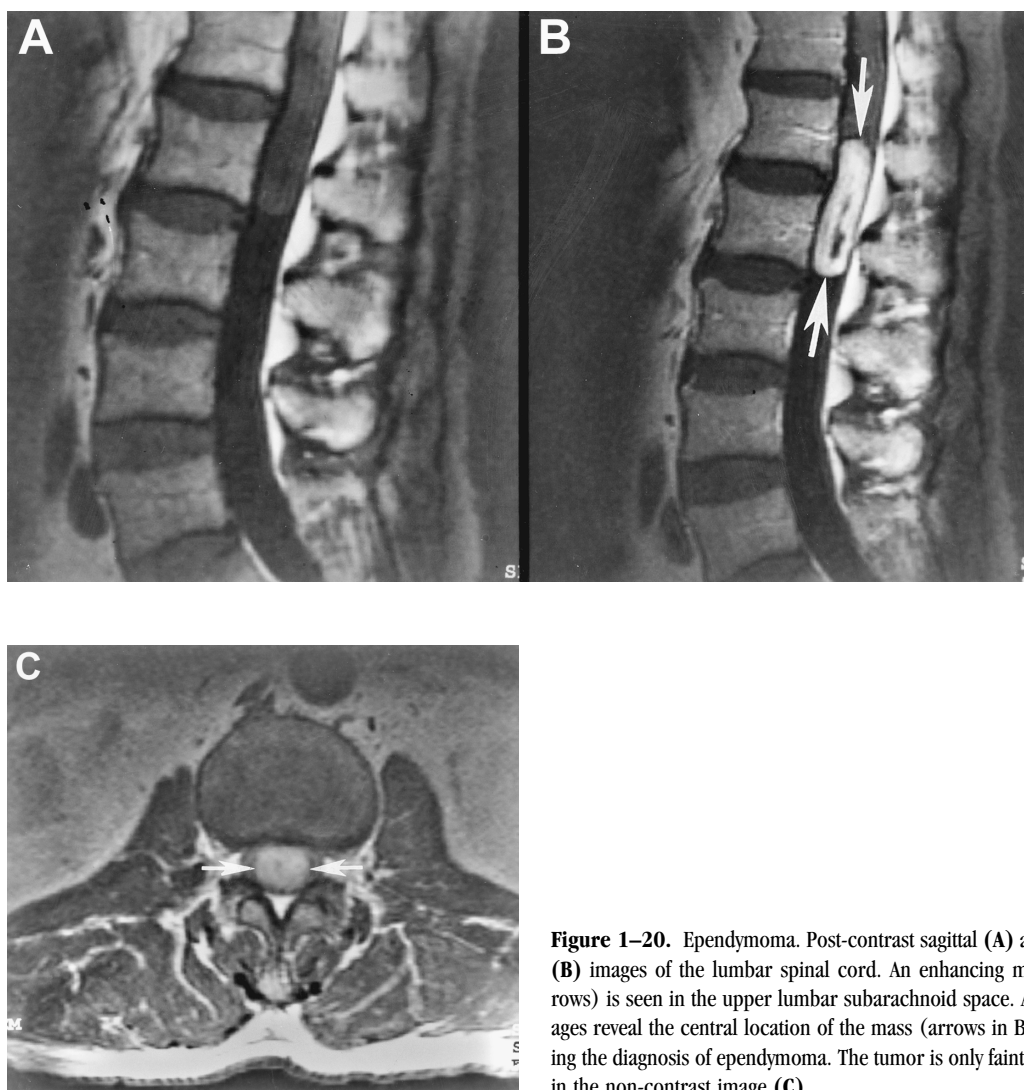


Figure 1-20. Ependymoma. Post-contrast sagittal (A) and axial (B) images of the lumbar spinal cord. An enhancing mass (arrows) is seen in the upper lumbar subarachnoid space. Axial images reveal the central location of the mass (arrows in B), favoring the diagnosis of ependymoma. The tumor is only faintly visible in the non-contrast image (C).

paraspinal region through an enlarged neural foramen, and the tumors often take on a dumbbell-like shape. On post-contrast MRI, neurinomas appear as a well-defined, intradural enhancing mass.

Neurofibromatosis

Multiple cranial and spinal nerve neurofibromas are associated with neurofibromatosis type 1 (Fig. 1-23). Astrocytomas and ependymomas can also occur in neurofibromatosis. Neurofibroma can undergo malignant degeneration into neurofibrosarcoma.

Congenital Tumors

Teratomas, epidermoid tumors, and dermoid tumors are congenital tumors that arise within the spinal cord. Teratomas, although rare, may be readily diagnosed by MRI, which can distinguish various components of the tumor, fat, bone, and teeth. A fatty mass combined with solid and cystic components of tumor, particularly located in the sacro-coccygeal region, are classic characteristics of teratomas. These tumors may be seen at birth. Magnetic resonance imaging can distinguish various components of the tumor.

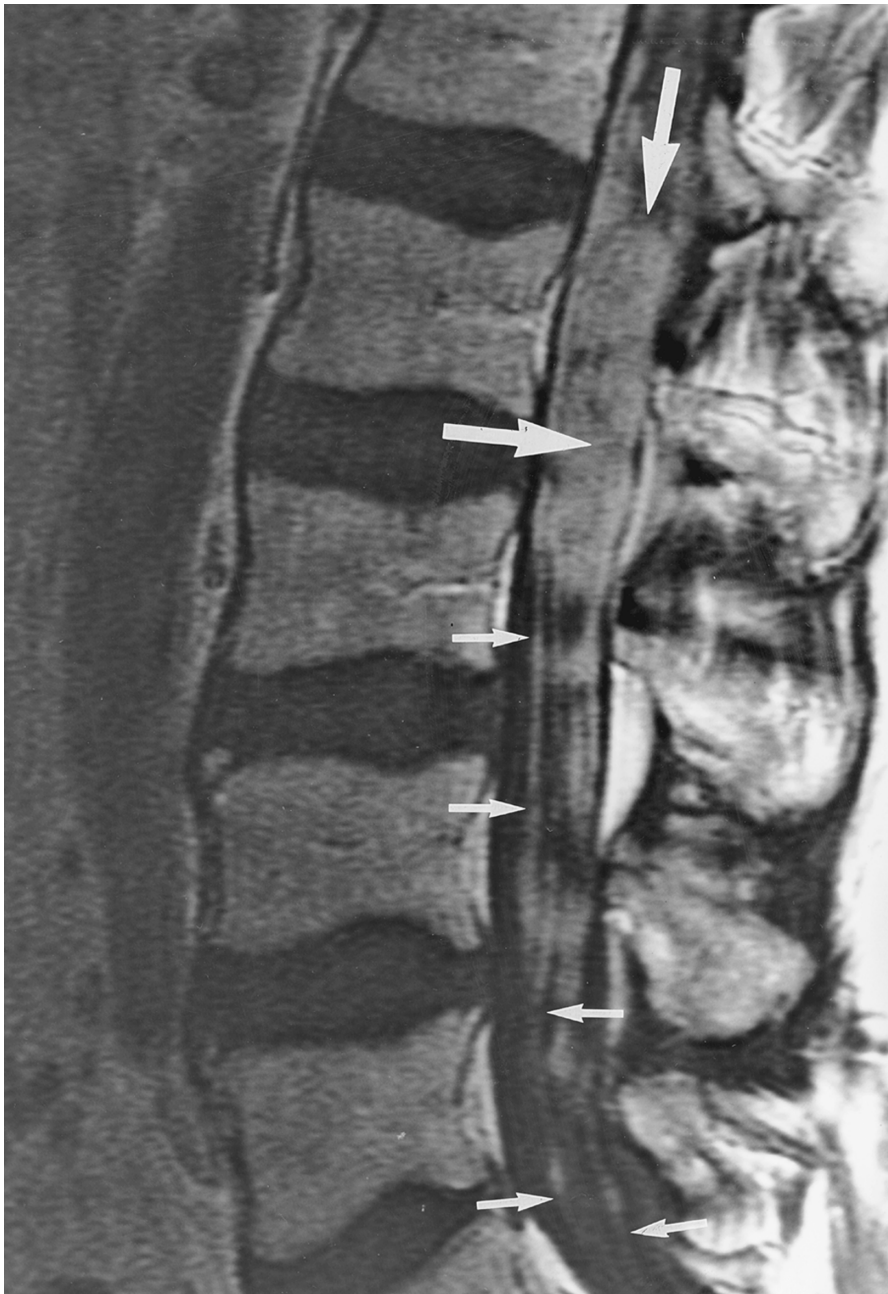


Figure 1–21. Melanoma with leptomeningeal metastatic tumor infiltration of the lumbar nerve roots. Post-contrast sagittal MRI scan shows that the lumbar subarachnoid space is filled with metastatic tumor (arrows). Lumbar nerve roots are markedly thickened with nodular enhancement (small arrows), indicating tumor infiltration.

IMAGING OF BRAIN METASTASES

Metastatic tumor growth, as in most neoplasms, depends on angiogenesis, which is the development of new blood vessels. Blood and Zetter (1990) found

that secondary tumors will grow only 1 to 2 mm if no angiogenesis is present. When Frank et al. (1987) injected VX2 rabbit carcinoma cells into the internal carotid artery of rabbits, 93% developed metastases; ocular metastases appeared in 86% of animals, with

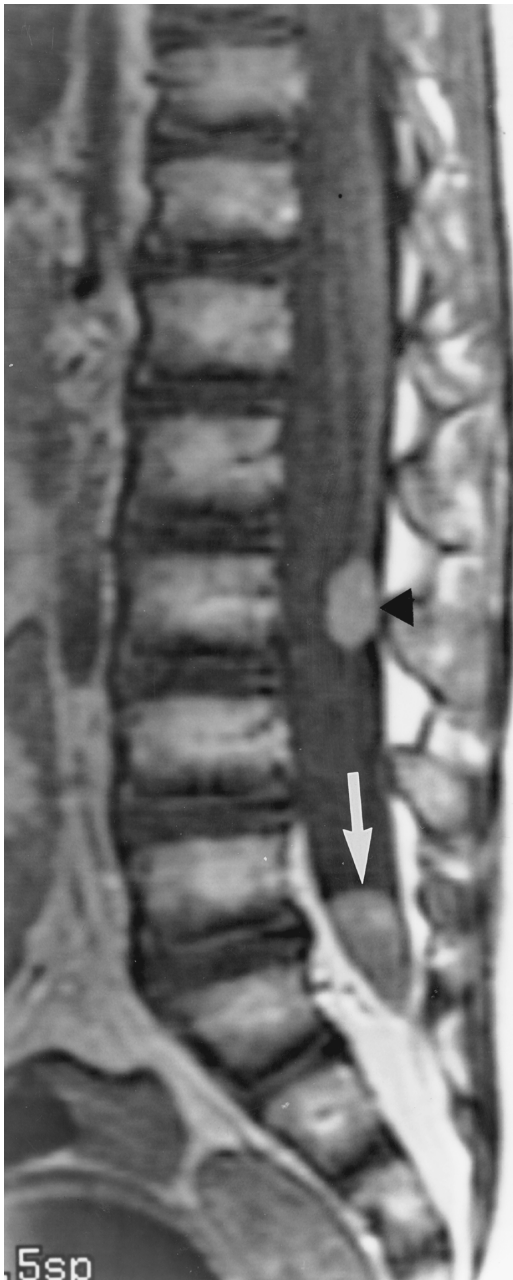


Figure 1–22. Medulloblastoma with dropped metastasis to the lumbar subarachnoid space. Post-contrast sagittal T₁-weighted images of the spine reveal dropped metastasis to the caudal end of the lumbar subarachnoid space (arrow) and at the L3 level (arrowhead).

anterior chamber involvement observed by the third day. These tumors were as large as 6 mm in diameter and demonstrated contrast enhancement after administration of IV gadopentetic acid, evidence that tumor endothelial cells were leakier than the blood–brain or blood–ocular barriers.

Either delaying the time between injection and scan or increasing the amount of contrast medium administered can enhance the appearance of a tumor on a CT scan. Davis et al. (1991) demonstrated that double doses delayed contrast infusion and that CT scans detected more lesions and provided additional information in 67% of cases examined.

Similar approaches in MRI have also yielded better detection of brain metastases. Yuh et al. (1992) examined 51 patients with MRI immediately after the administration of gadoteridol (Squibb, Princeton, NJ) in single and triple doses. No adverse effects were observed. In 10 of 27 cases examined with the triple-dose technique, improved lesion conspicuity and new lesion detection resulted in alterations to these patients' therapeutic regimens. Schorner et al. (1986) demonstrated the advantages of delaying imaging after IV contrast infusion during MRI by up to 68.5 minutes and found optimum imaging between 8.5 and 30 minutes after injection. Under these conditions, perifocal edema was minimally enhanced and was often visually less intense than normal brain, whereas necrosis was characterized by a slow, continuous increase in signal intensity, with maximum intensity reached toward the end of the examination but still continuing to rise. This effect probably reflects changes in variable tumor capillary permeability.

Sze et al. (1990) recommended that the MRI of the patient suspected of metastases should first include a pre-contrast axial short TR scan to determine if bone lesions or hemorrhage are present. Intravenous contrast should then be administered, followed by long TR scans and then by a short TR scan to demonstrate the presence of abnormal accumulations of contrast enhancement.

Elster and Chen (1992), in a study of patients with systemic cancer, demonstrated that nonenhancing white matter lesions have little chance of being a metastatic focus. Heier and Zimmerman (1992), in their comment on the Elster and Chen paper, are in general agreement with the caveat; however, they also concluded that white matter lesions without contrast enhancement that are localized, sharply defined, in proximity to subcortical U fibers, and have neurologic symptoms could be metastatic lesions.

Figure 1–23. Plexiform neurofibromatosis involving the cervical and thoracic spinal canal in a patient with neurofibromatosis. **(A)** Post-contrast sagittal T₁-weighted image of the cervical spine reveals an intradural neurofibroma (large white arrows) at the C1–C2 level, causing cervical cord compression (open arrow). Multiple neurofibromas are also seen at the C4, C5, C6, and C7 levels (small white arrows). **(B)** Pre-contrast axial T₁-weighted image at the C1–C2 level reveals a bilateral dumbbell-shaped neurofibroma with intraspinal (large white arrows) and extraspinal (black arrows) components passing through and enlarging the neural foramen (arrowheads). Note that the spinal cord (open arrows) is being squeezed on either side by bilateral neurofibromas. **(C)** Post-contrast sagittal T₁-weighted image of the thoracic spine reveals neurofibromas originating from the nerve roots at levels T11 and T12 (arrows). (*continued*)

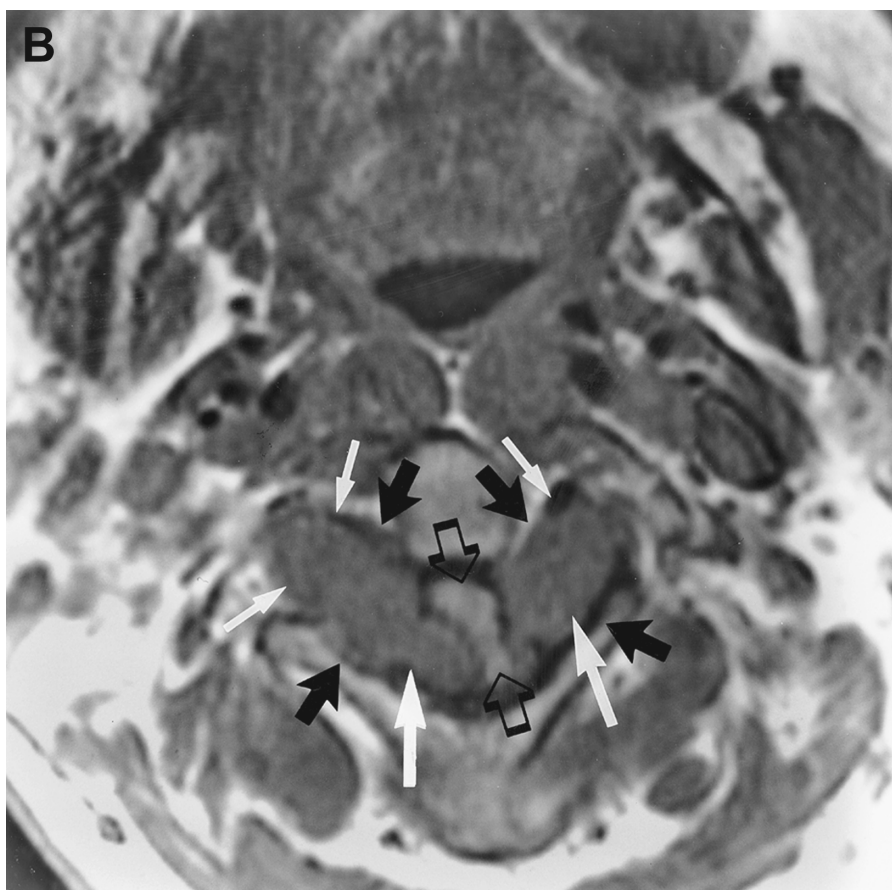




Figure 1-23. (Continued)

Presentation of Metastases

Tumors that metastasize to the brain have myriad appearances. They are often visualized as multiple metastatic foci of different sizes located on the meningeal surface in proximity to the subcortical U fibers or at the corticomedullary junction, with variable amounts of surrounding edema (Fig. 1-24). Lesions are solitary in as many as 50% of cases (Fig. 1-25). Intratumoral hemorrhage is observed, particularly in patients with melanoma (Fig. 1-26) and germ cell tumors (Fig. 1-27). In some instances, these hemorrhagic lesions must be distinguished from cavernous angiomas (Fig. 1-26). The edema pattern, according to Cowley (1983), migrates along short- and long-association bundles. The corpus callosum, although a major white matter tract, tends to be resistant because of a variation in makeup unless directly affected.

Leptomeningeal metastasis indicates involvement of the subarachnoid space. The outer border of the

subarachnoid space is formed by the arachnoid mater. The inner border represents pia mater that is closely applied to the surface of the brain and the accompanying sulci. Leptomeningeal spread of metastases may occur in systemic neoplasms in either localized or diffuse patterns (Fig. 1-28). These lesions have to be distinguished from infections, stroke, and postoperative occurrences with meningeal enhancement following shunt procedures, multiple lumbar punctures, and the presence of postural hypotension. Infective lesions often appear identical to leptomeningeal metastasis, so a history may be helpful. Because cancer patients are often immunocompromised, however, infections as well as neoplastic spread may develop. In stroke patients, differential features include gyral prominence on T₂-weighted images and enhancement patterns with visualization of affected arteries in the region early in the disease course. In another group of patients, lesions principally affect the dura mater and are usually unchanging.

Solitary nonmetastatic lesions, including inflammatory lesions, granulomas, and glioblastoma multiforme, may appear similar to metastatic lesions (Fig. 1-4), whereas multiple lesions on occasion may not be metastatic but rather are inflammatory, granuloma multifocal, or multicentric glioblastomas (Fig. 1-3). The presence of multicentric glioblastoma multiforme indicates that the tumor arises from separate sites of origin, whereas multifocal glioblastoma multiforme indicates that a communication exists between the multiple lesions. Calvarial metastases may be visualized on pre- and post-contrast imaging studies (Fig. 1-29). Cerebral abscess, glioblastoma multiforme, or metastasis may present on CT or MRI as a ring lesion. A simple ring lesion will usually be a metastasis or an abscess, but a complex ring lesion is usually a glioblastoma multiforme (Figs. 1-2 and 1-3).

Triple-dose examinations may be indicated for patients with solitary lesions who have negative single-dose studies but a positive history (Fig. 1-30) to exclude the presence of more lesions or to confirm whether a questionable lesion is a tumor (Yuh et al., 1992).

METASTASIS TO THE SPINE AND EPIDURAL TUMORS

Disease that is metastatic to vertebral bodies is usually blood borne. In pelvic neoplasms, the transport of tumor cells via the lumbar spine is secondary to

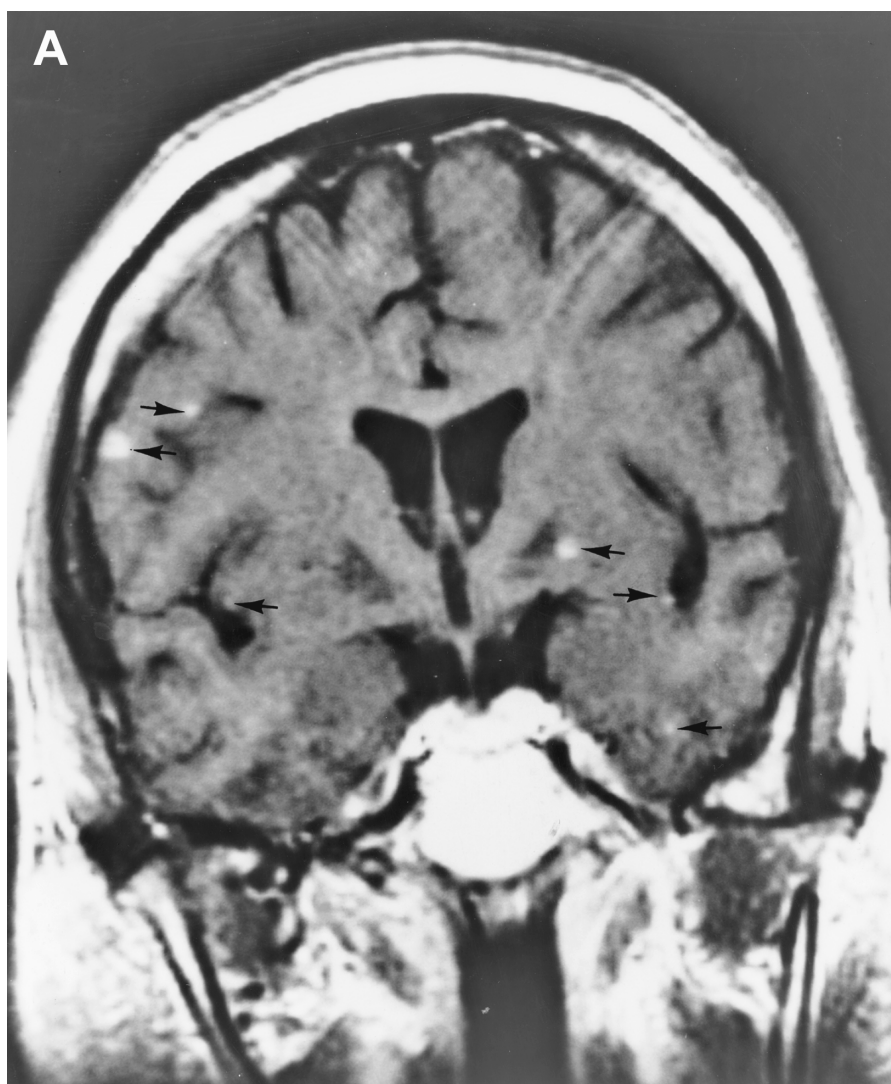


Figure 1–24. Multiple melanoma metastases. Post-contrast coronal T₁-weighted images (A,B) reveal multiple metastases of variable size (arrows). (*continued*)

transport via Batson's venous plexus. The spinal canal is involved secondarily, with epidural tumor producing spinal cord compression. Magnetic resonance imaging is very sensitive in detecting spinal vertebral body metastasis, including the presence of an epidural component and the degree of spinal cord compression. Primary tumors of the bone affecting the spinal canal are rare; however, tumors such as chordoma (Fig. 1–31) and aneurysmal bone cysts can produce expansile destructive changes in the

bone, giving rise to epidural tumors with subsequent spinal cord compression. The entire spinal column can be easily studied without invasive procedures. Thus, MRI has proved to be the imaging modality of choice when dealing with patients who present with symptoms of acute spinal cord compression.

Carcinomas of the breast, lung, kidney, and prostate most commonly metastasize to the spine. Others include sarcomas, neuroblastomas, and melanomas. Most metastatic tumors are destructive (os-

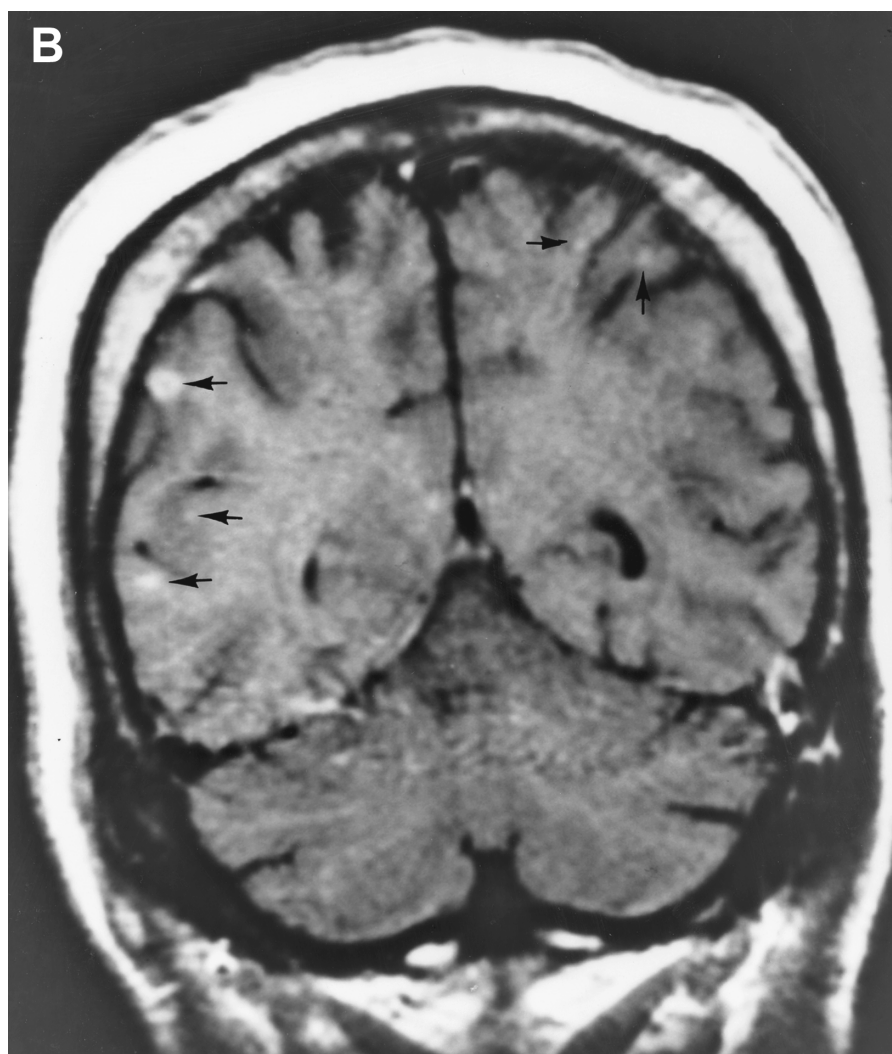


Figure 1-24. (Continued)

teolytic) in nature (Fig. 1-32). Common osteoblastic metastases are prostate and breast (Fig. 1-33). Because it demonstrates marrow replacement, MRI is more sensitive than ^{99m}Tc Technetium bone scanning in detecting early bone marrow metastasis before destructive changes take place.

Lymphoma readily infiltrates the vertebral marrow cavity, and the replacement of marrow by tumor cells can be easily diagnosed using MRI scans. Lymphoma can also infiltrate the epidural space, spinal cord, and roots (Fig. 1-34). A characteristic feature of epidural lymphoma is the long extent of the tumor.

Multiple myeloma comprises approximately 34% of malignant bone tumors, with a peak incidence at 50 to 70 years of age. Malignant proliferation of plasma cells in the bone marrow of the spine results in tumor replacement of normal marrow. The involved vertebral body may show localized masses and pathologic fracture. The presence of epidural tumor and spinal cord compression may be best evaluated through MRI. Early identification of vertebral body involvement by myeloma may permit prevention of many neurologic sequelae by directing the early institution of radiotherapy or chemotherapy.

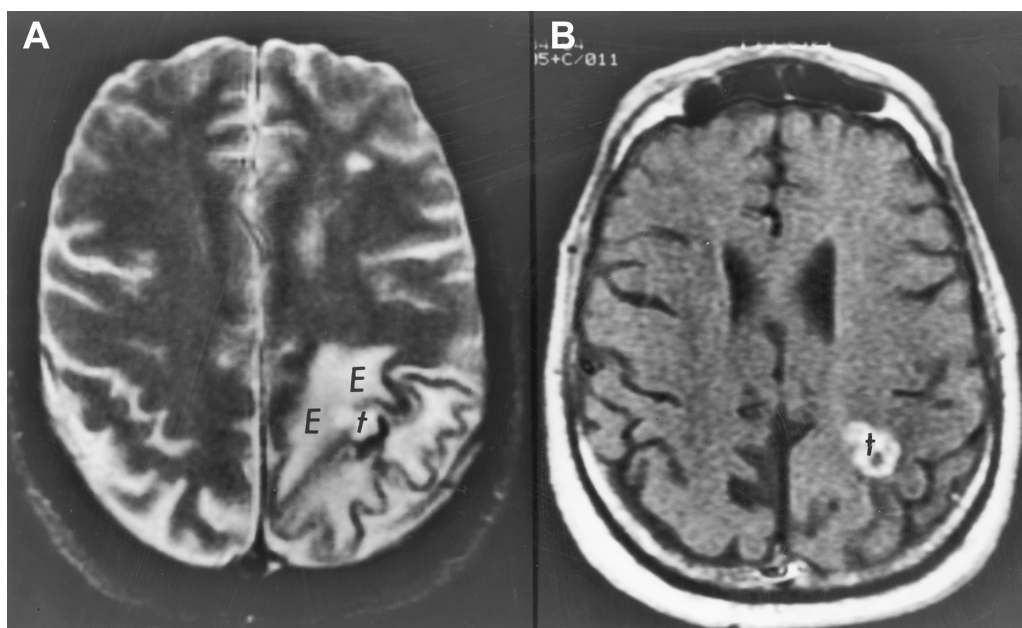


Figure 1-25. Solitary metastasis in a patient with non-small cell lung cancer. An axial T₂-weighted image (A) reveals multilobulated tumor (*t*) with surrounding edema (*E*). The post-contrast axial T₁-weighted image (B) reveals a focal multilobular-enhancing lesion with a central low-intensity zone representing necrosis.

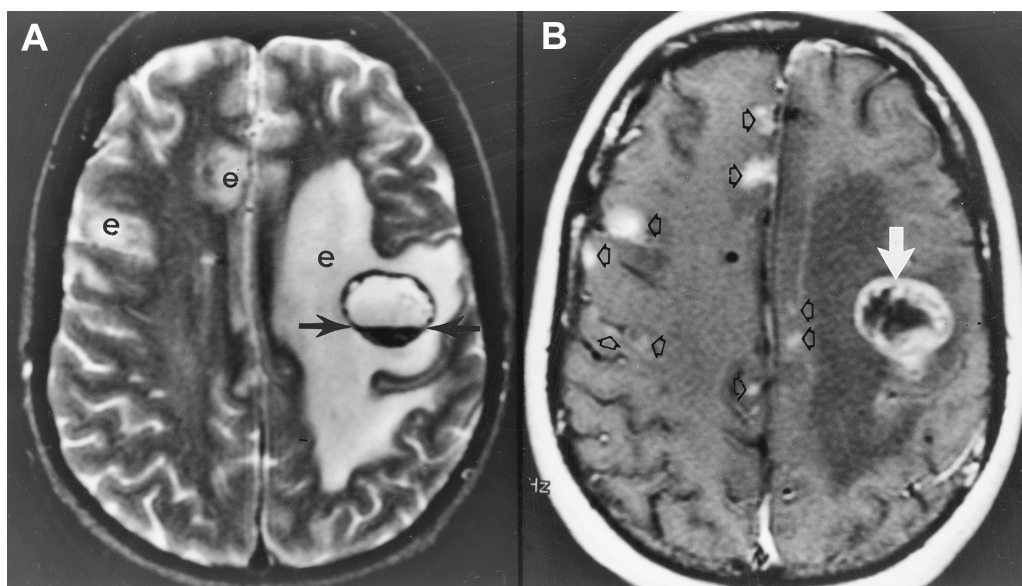


Figure 1-26. Multiple melanoma metastases with hemorrhage and leptomeningeal metastases. (A) Axial T₂-weighted image reveals multiple foci of edema of variable size (*e*) also with hemorrhagic metastasis and fluid level (black arrows). (B) Post-contrast axial T₁-weighted image at almost the same level with parenchymal metastases (white arrow) and leptomeningeal metastases (open arrows). (C) Axial T₂-weighted image at the ventricular level demonstrates multiple foci of edema (*e*) as well as a focus of heterogeneous signal intensity on the left with both hyperintensity and hypointensity in the region of the basal ganglia–paraventricular region (black arrowhead) and a paraventricular focus on the right (black arrowhead). (D) Post-contrast axial T₁-weighted image at the ventricular level reveals diffuse leptomeningeal disease involving arachnoid and pia mater (open arrows) and also arising from the ependyma of the lateral ventricles (closed arrows). (*continued*)

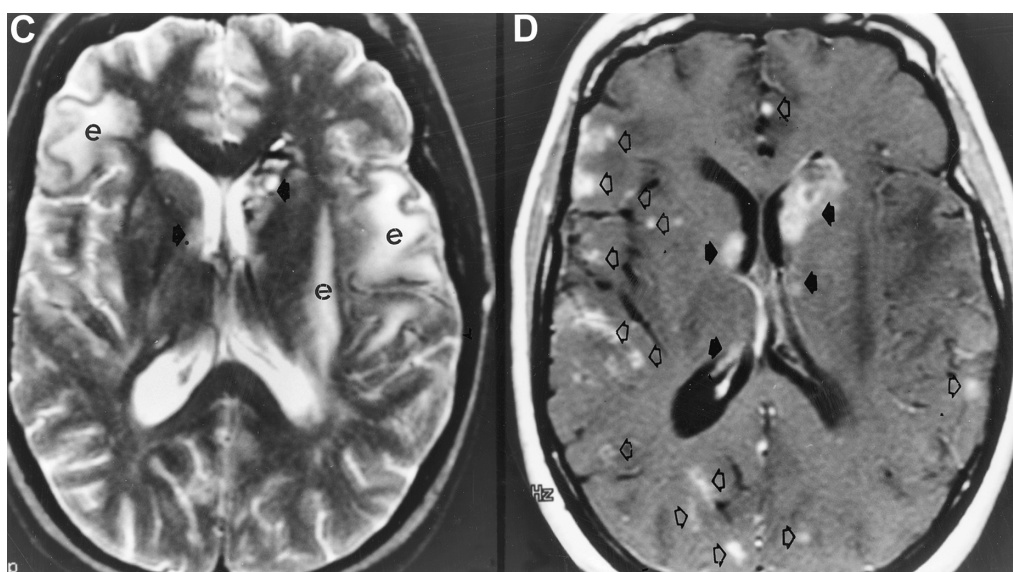


Figure 1-26. (Continued)

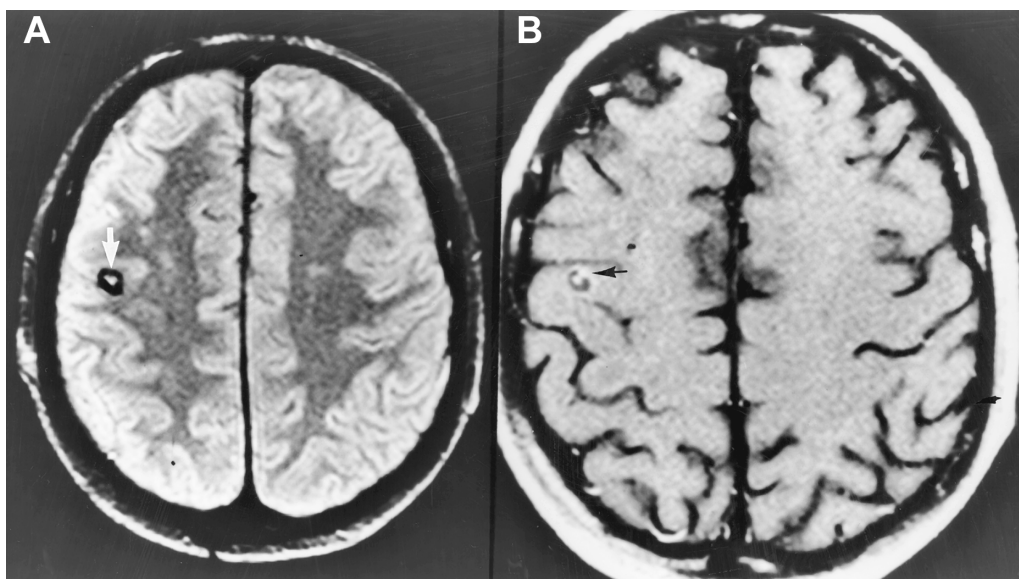


Figure 1-27. A patient with a metastatic germ cell tumor. Proton density-weighted image at the level of the centrum semiovale (**A**) reveals a target lesion with a hypointense black rim (arrow) and a central hyperintensity. This image raised the possibility of a cavernous angioma. (**B**) The post-contrast T₁-weighted image reveals contrast enhancement medially and superiorly (arrow). The hypointense margin is less distinct, although the central hypointensity is unchanged. The contrast enhancement favors the diagnosis of hemorrhagic metastases rather than cavernous angioma.



Figure 1–28. Child with medulloblastoma and leptomeningeal seeding. Post-contrast T₁-weighted image reveals diffuse, dural–arachnoid (open arrows) and pial enhancement (black arrows).

PLEXOPATHY

Patients with CNS malignant tumors can present with symptoms similar to those that occur with nerve root compression. The most common cause of neuralgia in these patients is the coexisting herniated disc in the cervical or lumbar region. Magnetic resonance imaging can clearly distinguish nerve root compression caused by a herniated disc (Fig. 1–35) from

nerve root infiltration by malignant tumors (Fig. 1–21).

Magnetic resonance imaging is also sensitive in detecting lesions affecting nerve roots outside the spinal canal, such as brachial plexus (Fig. 1–36) and lumbosacral plexus. Lesions that can give rise to brachial plexus neuralgia are Pancoast tumors, metastatic lymphadenopathy, malignant spinal tumors, radiation fibrosis, and benign tumors such as nerve sheath tumors.

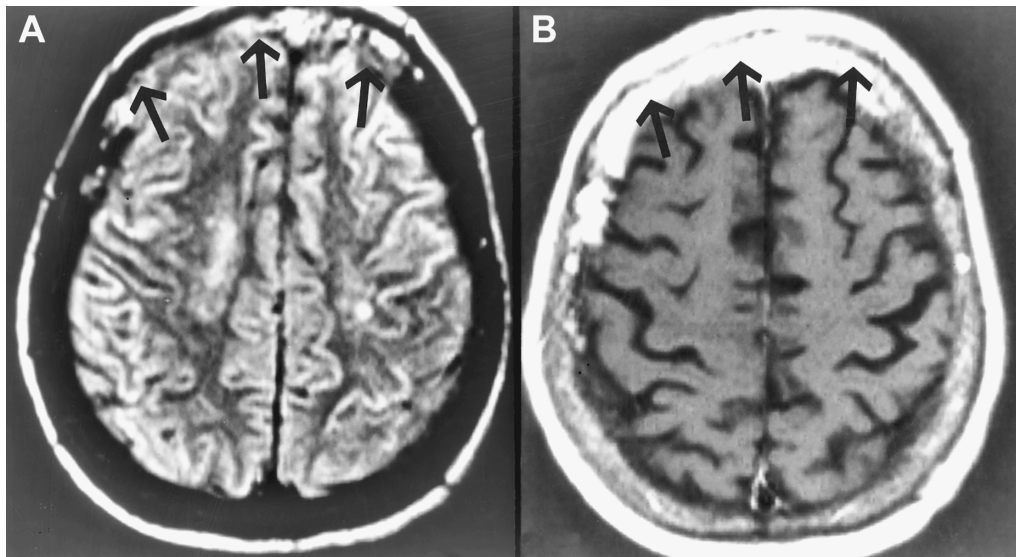


Figure 1-29. Calvarial metastases in a patient with breast cancer. **(A)** Axial proton density-weighted image shows extensive hyperintensity within frontal bone due to metastases (arrows), whereas uninvolved calvarium is hypointense (black). **(B)** The post-contrast axial T₁-weighted image shows contrast enhancement of the diffuse calvarial metastatic lesion (arrows) compared with the remainder of the calvarium, which shows heterogeneous hyperintensity reflecting marrow replacement by fat.

IMAGING OF RADIATION DAMAGE

Basis for Radiation Changes

Radiation damage to the CNS has been observed with increasing frequency because of treatment sequencing hyperfractionation, the use of radiation doses over 60 Gy, more older patients receiving radiation, adjunctive chemotherapy given during and after radiotherapy, and the increased duration of patient survival (Kyritsis et al., 1993; Fike et al., 1984; Ball et al., 1992; Burger and Boyko, 1991). Effects from radiation may be divided into early, early delayed, and delayed reactions (Hoffman et al., 1979; Fike et al., 1984; Ball et al., 1992; Burger and Boyko, 1991; Castel and Caille, 1989).

Early reactions are caused by acute or subacute effects that persist as long as 6 weeks after therapy. These reactions may follow conservative radiation treatment and leave no lingering effects, although in rare cases permanent sequelae or death may result. In early reactions a transient vasodilatation occurs with a breakdown of the BBB and development of vasogenic edema (Fike et al., 1984; Ball et al., 1992; Burger and Boyko, 1991; Castel and Caille, 1989).

In patients with early delayed injury, capillary vasodilatation, capillary permeability and breakdown of the BBB, vasogenic edema, and demyelination may develop, but may be transient (Hoffman et al., 1979; Ball et al., 1992; Burger and Boyko, 1991). The risk period is generally considered to be 4 to 18 weeks after the completion of irradiation (Hoffman et al., 1979).

A delayed reaction can occur months to more than a decade following treatment. In patients with delayed injury, severe changes occur, which tend to be permanent. Among these are vascular endothelial injury with infarction and white matter changes, including focal or diffuse demyelination or necrosis (Ball et al., 1992). The mechanisms that contribute to the resultant brain damage are incompletely understood, but likely include alterations of fibrinolytic enzymes, direct injury to white matter, direct damage to glial cells, immune mechanisms, and vascular-related effects.

Authors disagree about which pathologic changes occur first. Although one factor might be more important than another, it is most probable that a combination of changes occur simultaneously as a reactive cascade of events. Vascular changes are obviously important because they result in ischemia, infarction,

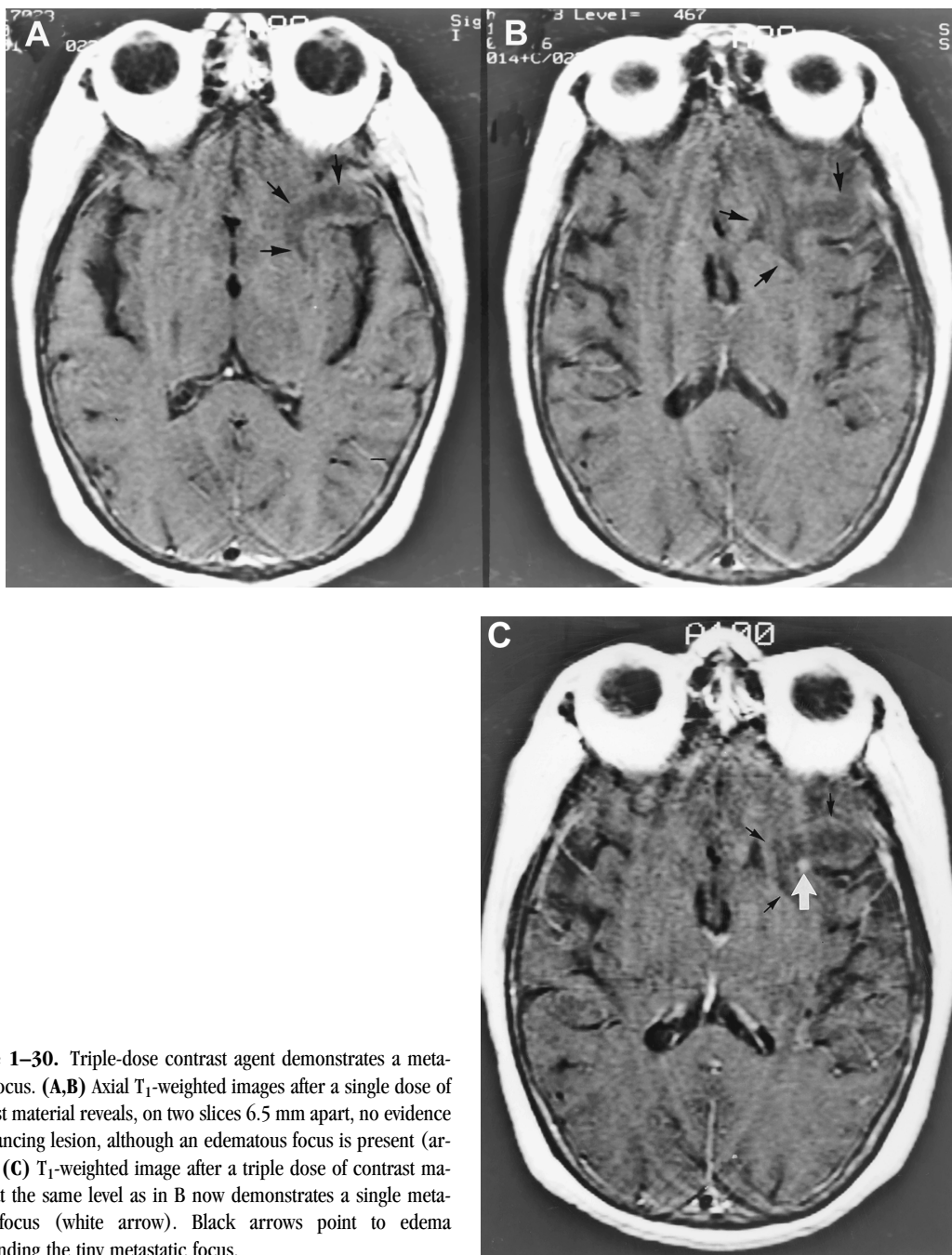


Figure 1-30. Triple-dose contrast agent demonstrates a metastatic focus. (A,B) Axial T₁-weighted images after a single dose of contrast material reveals, on two slices 6.5 mm apart, no evidence of enhancing lesion, although an edematous focus is present (arrows). (C) T₁-weighted image after a triple dose of contrast material at the same level as in B now demonstrates a single metastatic focus (white arrow). Black arrows point to edema surrounding the tiny metastatic focus.

and edema. Positron emission tomography (PET) studies demonstrate significant effects on metabolic activity (Doyle et al., 1987; Valk and Dillon, 1991). Oligodendrocytes, which have a large composition of myelin, are damaged early (Fike et al., 1984). Myelin

is hydrophobic, and its loss is associated with increased extracellular fluid (Fike et al., 1984). Direct injury to cerebral tissue causes structural changes that result in decreased brain volume (Ball et al., 1992).



Figure 1–31. Chordoma involving the clivus (black arrow), C1, and C2 vertebral bodies. The chordoma is associated with a large epidural tumor (black arrow), producing cervical cord compression (open arrows). There is also a prevertebral soft tissue tumor (white arrows). Curved white arrows point to artifacts created by surgical clips.

Radiation-Induced Damage to the Brain

Magnetic resonance imaging is far more sensitive than CT in detecting radiation-induced damage to the brain. The severe form of radiation-induced damage to the brain is radiation necrosis, the end result of perivascular coagulative necrosis affecting the white matter. As would be expected, radiation necrosis occurs most commonly at the site of max-

imum radiation delivery in the immediate vicinity of the tumor site and surrounding the surgical cavity of a partially or totally resected tumor (Fig. 1–37). Radiation necrosis can resemble recurrent tumor on MR or CT imaging because of the following shared characteristics: (1) origin at or close to the original tumor site, (2) contrast enhancement, (3) growth over time, (4) edema, and (5) exertion of mass effect.

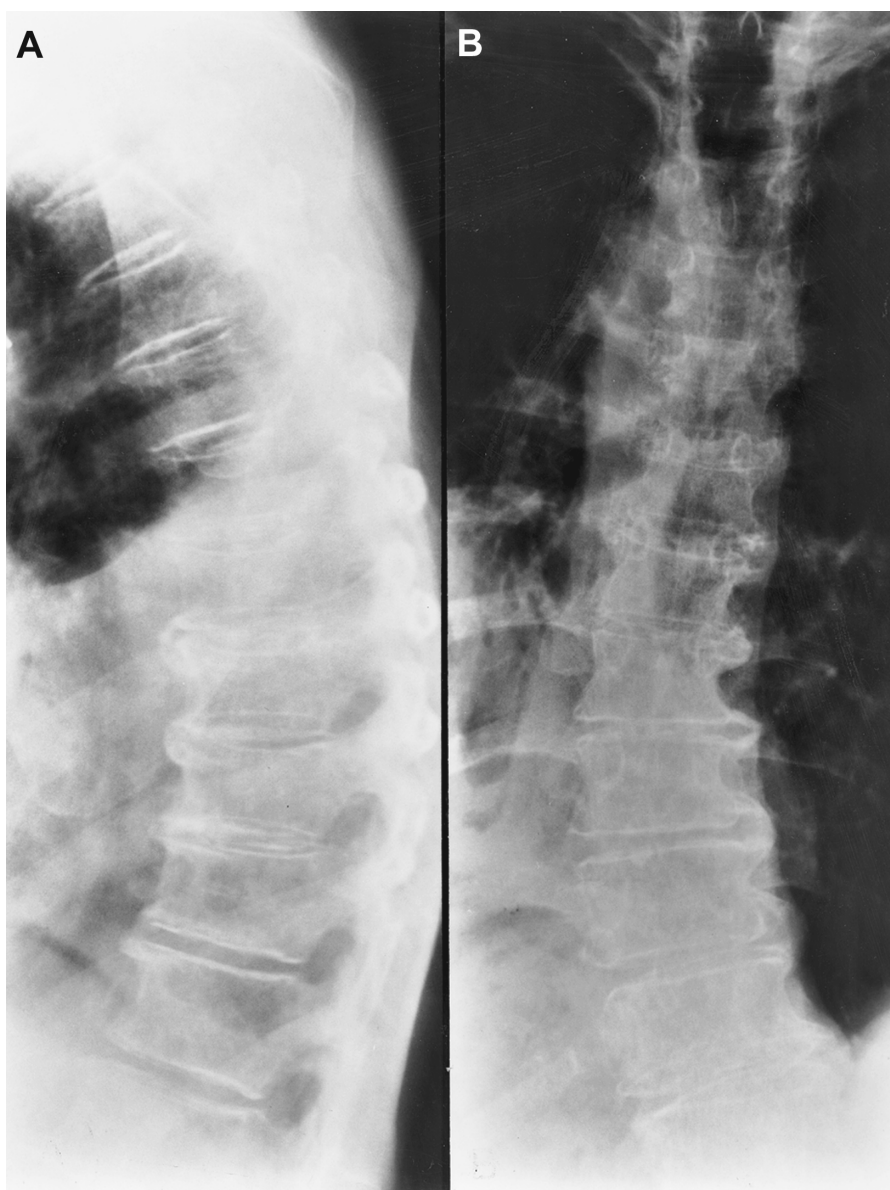


Figure 1-32. Patient with carcinoma of the breast with a history of back pain and osteolytic metastases. **(A,B)** Plain roentgenograms of the thoracic spine in the lateral and anterior posterior projections were normal. A bone scan was also normal. **(C)** Sagittal multiplanar-gradient echo T₂-weighted image reveals multiple hyperintense foci (arrows) indicating osteolytic metastases. **(D,E)** Sagittal T₁-weighted images of thoracic and lumbar spine reveal multiple hypointense foci (arrows) affecting almost all of the visualized vertebral bodies. (*continued*)

With respect to the MRI characteristics of radiation necrosis, most lesions consist of an enhancing mass (Figs. 1-37 to 1-42) with a central area of necrosis. The lesions are single or multiple. The enhancing characteristics of radiation necrosis com-

monly seen are a ring lesion with a central “soap bubble”-like interior (Fig. 1-38E), solid lesions (Fig. 1-40), or a “Swiss cheese”-like interior (Fig. 1-41A,B). Contrast enhancement of these lesions is secondary to radiation-induced endothelial damage,

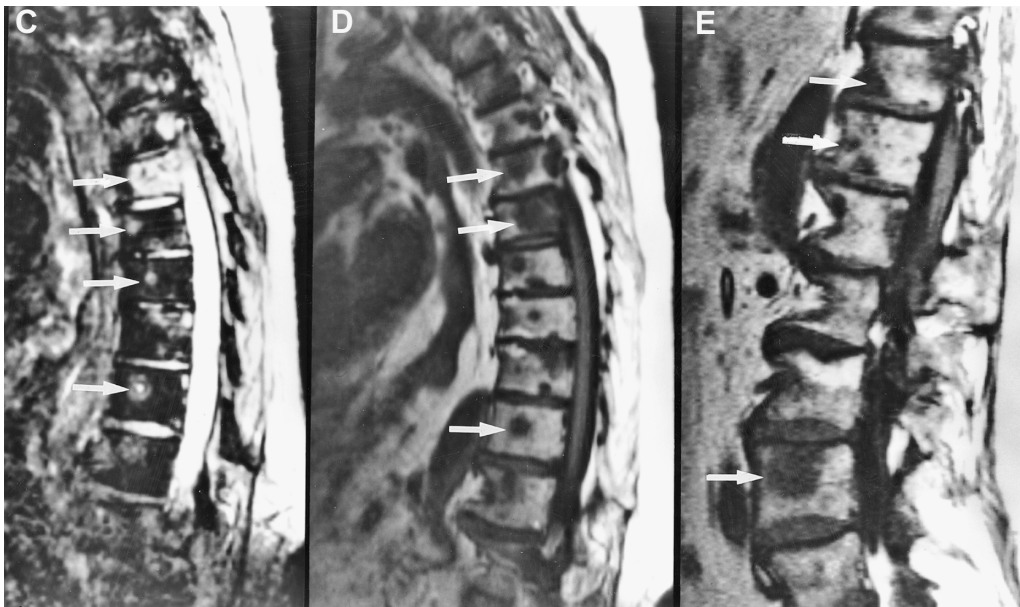


Figure 1-32. (Continued)

which leads to the breakdown of the BBB. The use of platinum-based chemotherapy drugs such as cisplatin and carboplatin combined with radiation therapy (RT) may contribute to the development of radiation-induced necrosis (Kumar et al., 2000).

In addition to the most common form of radiation necrosis, which consists of a single lesion arising at the site of the original primary tumor (Fig. 1-37), other less common patterns may be observed, such as (1) multiple lesions (Fig. 1-41); (2) lesions occurring within the ipsilateral hemisphere distant from the site of primary tumor (Fig. 1-38A-E); (3) lesions in the contralateral hemisphere (Fig. 1-39); and (4) lesions arising remotely from a primary site, for example in the cerebellum (Fig. 1-40), brain stem (Fig. 1-37), and subependymal lesions. Periventricular white matter is especially vulnerable to radiation necrosis. This neuroanatomic region has a relatively poor blood supply from long medullary arteries that lack collateral vessels, creating a susceptibility to ischemic effects produced by postradiation vasculopathy (Moody et al., 1990; Nelson et al., 1991). The corpus callosum is also vulnerable to radiation necrosis.

The incidence of radiation necrosis after conventional therapy ranges from 5% to 24%, with higher rates at autopsy (Burger et al., 1979; Marks et al.,

1981). Kumar et al. (2000) have reported results from a cohort of 148 adult patients who underwent surgical resection of malignant brain (glial) tumors. The patients were subsequently entered into a research protocol that consisted of accelerated RT with carboplatin followed by chemotherapy (procarbazine, lomustine, vincristine). Pure radiation necrosis developed in 20 patients (13.5%). Sixteen patients (10.8%) manifested a mixture predominantly of radiation necrosis with limited recurrent and/or residual tumor (less than 20% of resected tissue). These findings were demonstrated by histopathologic examination at surgery or autopsy in 22 of the 56 patients with anaplastic gliomas (VA Levin, unpublished information, 2001) and in 14 of the 92 patients with glioblastomas under protocols DM 88-133 (Levin et al., 1995). The necrosis of the brain was attributed to the combined effects of RT and chemotherapy.

Radiation-induced necrosis is a dynamic pathophysiologic process with several possible clinical outcomes. Although continued necrotic growth with attendant cytologic edema and mass effect is commonly seen, lethal progression is not inevitable. Some lesions will stabilize, whereas others will regress (Fig. 1-42). In some cases, surgery may be required to reduce mass effect and, despite advances in special imaging techniques, to establish an accurate histo-

logic diagnosis. Finally, even after gross total surgical resection, radiation necrosis recurrence will be observed in some cases. The MRI spectrum of RT-induced injury to the brain includes, in addition to necrosis, radiation-induced vasculopathy, white matter demyelination (Fig. 1–43), radiation-induced cranial neuropathy, mineralizing microangiopathy (Fig. 1–44), and radiation-induced neoplasms. The role of single-photon emission tomography and PET in distinguishing recurrent brain tumor from radiation necrosis is discussed in more detail in Chapter 2.

ADVANCED MAGNETIC RESONANCE IMAGING TECHNIQUES IN NEUROIMAGING

From the mid-1980s through the mid-1990s, proton density-weighted (PDW), T₁-weighted (T₁W) with and without contrast agent enhancement, and T₂-weighted (T₂W) acquisitions provided the standard set of MR images with which intracranial lesions were evaluated. In the mid-1990s, fluid attenuated inversion recovery (FLAIR) and magnetization transfer contrast sequences were added to, or used in place of, one or more of the standard set of PDW, T₁W, and T₂W images.

The FLAIR images have significantly improved visualization of neoplasm versus edema, cortical strokes, and periventricular multiple sclerosis plaques, for example, where magnetization transfer contrast images have been reported to improve the conspicuity of small metastases. These two additional sequences are not, however, radical departures from the standard imaging sequences used since the mid-1980s. Instead, they have essentially been made robust and rapid enough for routine clinical applications.

In the late 1990s significant improvements were made in the magnetic gradient field subsystems of commercial scanners. The maximum gradient field amplitudes (Tesla/meter, T/m) increased by a factor of 2 to 4, and the time required to switch the gradient fields on and off (the rise time, in seconds) decreased by nearly equal factors. This results in gradient field slew rates (T/m/sec) that increased by factors of 4 to 16. Coupled with improvements in the data acquisition sampling rates, these gradient subsystem changes resulted in scan times as rapid as 30



Figure 1–33. Patient with prostatic cancer and multiple osteoblastic metastases within the lumbar spine. **(A)** Antero-posterior projection of lumbar spine reveals multiple large and small nodules of increased density within the lumbar spine and sacrum, which look like cotton balls. **(B)** Sagittal T₁-weighted image of the lumbar spine shows multiple hypointense foci (arrows) affecting all lumbar vertebral bodies and the sacrum. **(C)** Sagittal T₂-weighted image reveals that all lesions remain hypointense, indicating that the lesions are osteoblastic metastases. (*continued*)

to 50 msec/image. Such acquisition rates have opened up entirely new neuroimaging options that result in images that depict not only anatomy but function. This section discusses some of these new options in neuroimaging, each of which depends on high-speed image acquisition techniques. In addition, advances in

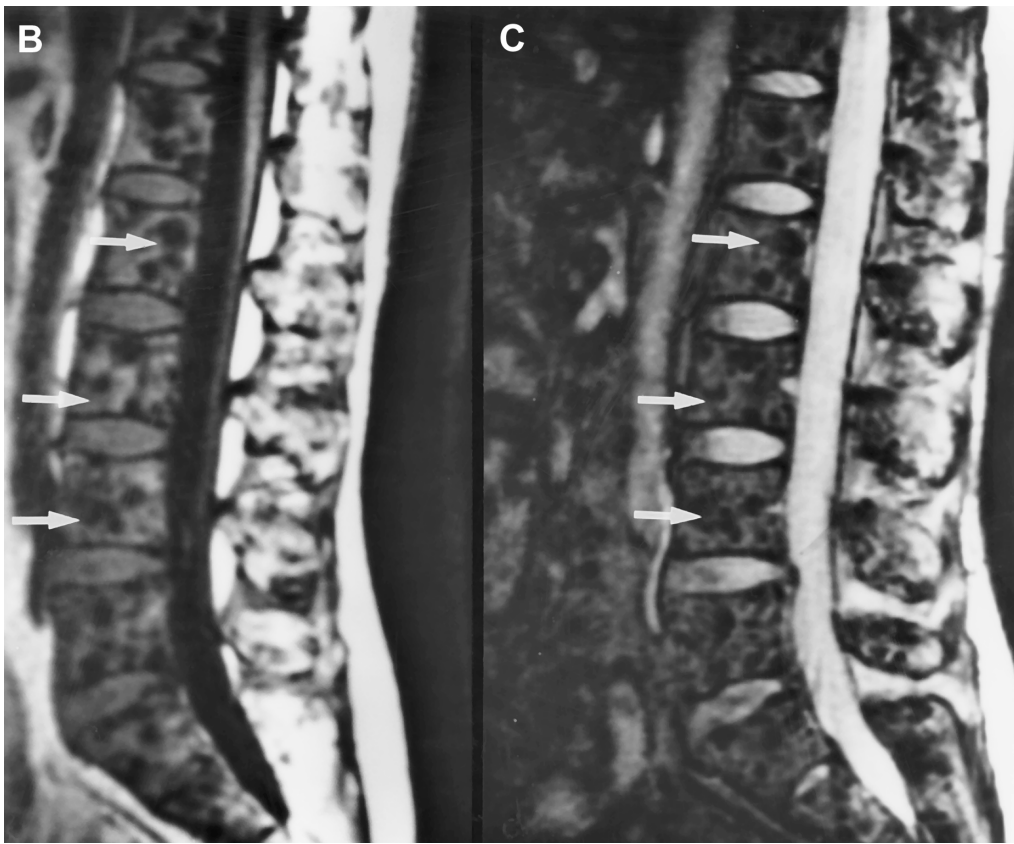


Figure 1-33. (Continued)

spectroscopic data acquisition and processing capabilities, which may have important applications in the management of tumor patients, are briefly reviewed.

Perfusion Imaging Pulse Sequences

It is commonly accepted that tumors cannot grow beyond a few millimeters in diameter without altering the local vascular environment. Furthermore, tumors with highly permeable and plentiful blood vessels appear to be more likely to metastasize and, in general, are associated with a poorer prognosis. Treatment-related changes, on the other hand, are variably associated with increases in vascular density and permeability. Therefore, the ability to assess vascular volume, flow, and permeability may be highly valuable in the noninvasive characterization of intracranial lesions and may provide a means of more reliably determining tumor progression versus treatment-related changes that are often difficult or

impossible to distinguish even with the wide range of image contrasts provided by standard MRI techniques. Techniques available to noninvasively monitor tissue vascularity should prove highly useful for assessing the efficacy of antiangiogenic agents currently in clinical trials.

Two MR-based techniques have been developed for mapping regional cerebral blood flow (rCBF) and regional cerebral blood volume (rCBV). The first technique, often referred to as *dynamic susceptibility contrast* (DSC) mapping, takes advantage of the transient susceptibility change that occurs as a bolus of paramagnetic contrast agent passes through the microvascular vessels (Sanders and Orrison, 1995; Ostergaard et al., 1996a,b; Sorensen and Rosen, 1996; Sorensen et al., 1997). These transient susceptibility changes are manifested as short-lived, localized, inhomogeneities in the local magnetic field. Such changes cause enhanced dephasing of the local nuclear spins by decreasing the “apparent” T_2 relax-

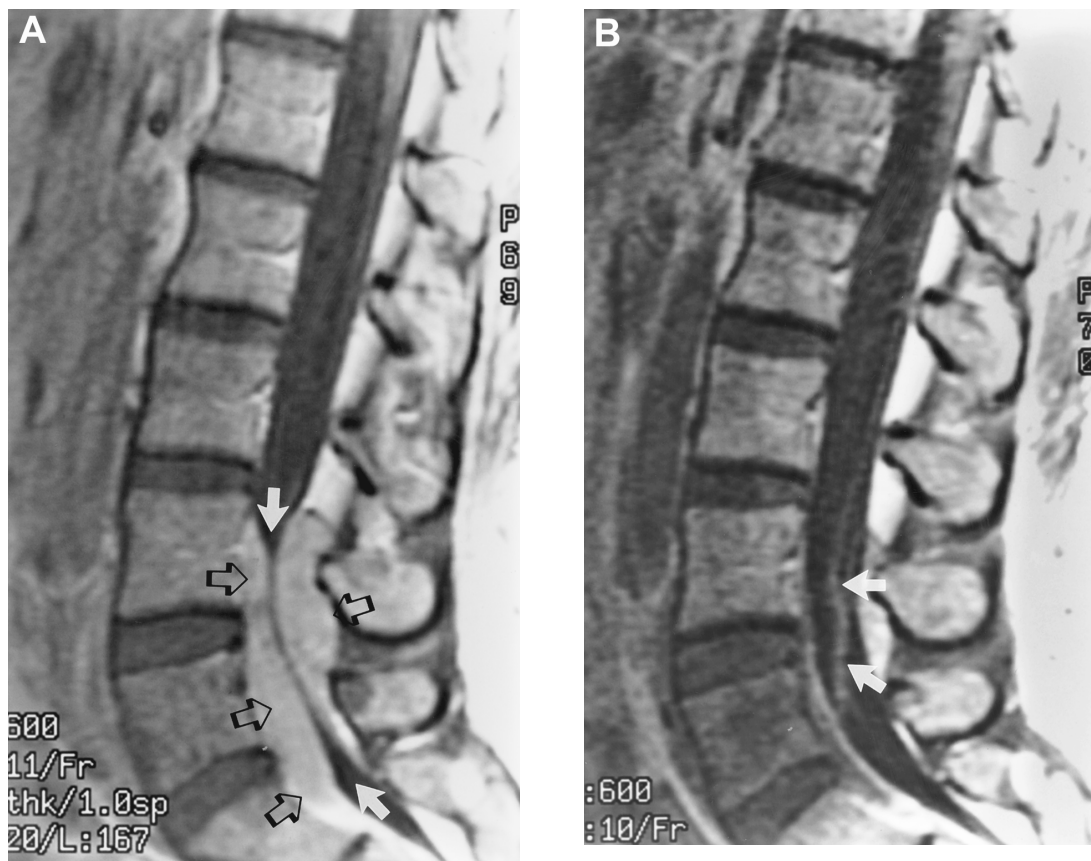


Figure 1-34. Hodgkin's disease of the lumbar spinal canal with epidural mass. **(A,B)** Post-contrast sagittal T₁-weighted images. **(A)** There is extensive ventral and dorsal epidural tumor (open arrows) squeezing the lumbar subarachnoid space and nerve roots (white arrows). **(B)** Post-radiation therapy follow-up MRI scan reveals near-complete disappearance of the epidural tumor with expansion of the lumbar subarachnoid space, which shows an excellent response to therapy. Some residual thickening of the nerve roots (arrows) is noted.

ation time (T_2^*). This dephasing results in a transient decrease in signal intensity on T₂W or T₂*W images as the bolus passes (Fig. 1-45). The higher the rCBV, the greater the magnitude of the transient signal loss. Assuming that the contrast agent remains in the vasculature, that is, there is no BBB breakdown, such images can be used to construct maps of rCBV (Fig. 1-46). If, however, the BBB is fenestrated and contrast agent "leaks" from the vascular to the interstitial space, the DSC mapping technique can underestimate the rCBV measures due to loss of compartmentalization of the contrast agent and local decreases in the T₁ relaxation times (Sorensen and Rosen, 1996).

This can be particularly problematic with the current class of commonly utilized paramagnetic con-

trast agents that are FDA approved for clinical use. All three of these agents, gadolinium dimeglumine, gadodiamide, and gadoteridol, have relatively small molecular weights (on the order of 600 daltons) and readily extravasate in cases of BBB fenestration. Several higher molecular weight (greater than 25,000 dalton) contrast agents are currently in phase I and phase II clinical trials and promise to greatly expand the use of DSC mapping of vascular volume and flow in both neuroimaging applications and body imaging applications, where the absence of a BBB exacerbates the contrast leakage problem. An advantage of the DSC technique, however, is the favorable signal-to-noise ratio of the resulting rCBV maps, particularly if double-dose bolus injections are utilized. If the mean transit time (MTT) of the contrast agent can be de-



Figure 1–35. Patient with melanoma who presented with acute radiating pain to the arm. Sagittal T₁-weighted image of the cervical spine reveals a herniated disc at the C4–C5 level (white arrow) with cervical cord compression (black arrow). A smaller herniated disc is also seen at the C6–C7 level (open arrow).

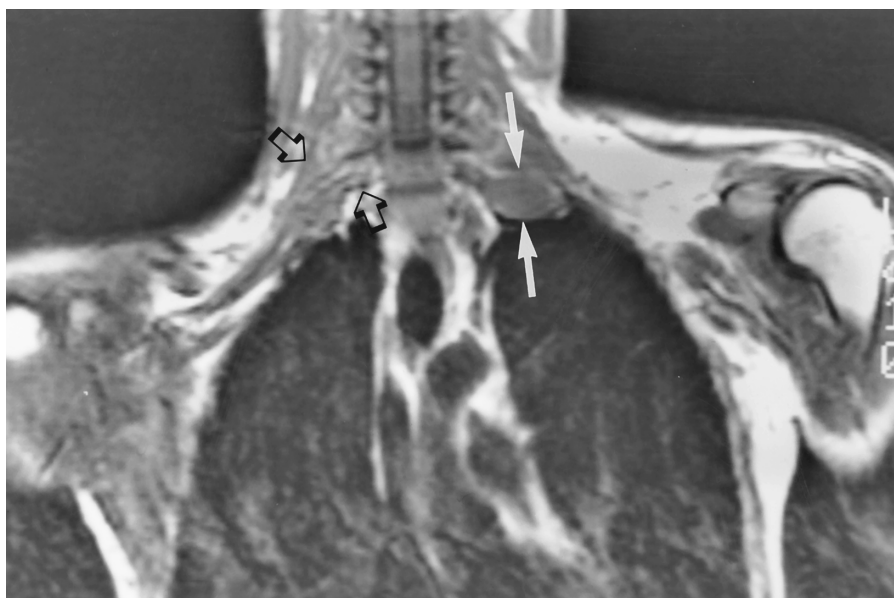


Figure 1–36. Dumbbell-shaped neurofibroma involving the right brachial plexus. There is a large neurofibroma originating from the left brachial plexus (white arrows) compared with the normal brachial plexus on the right (open arrows).

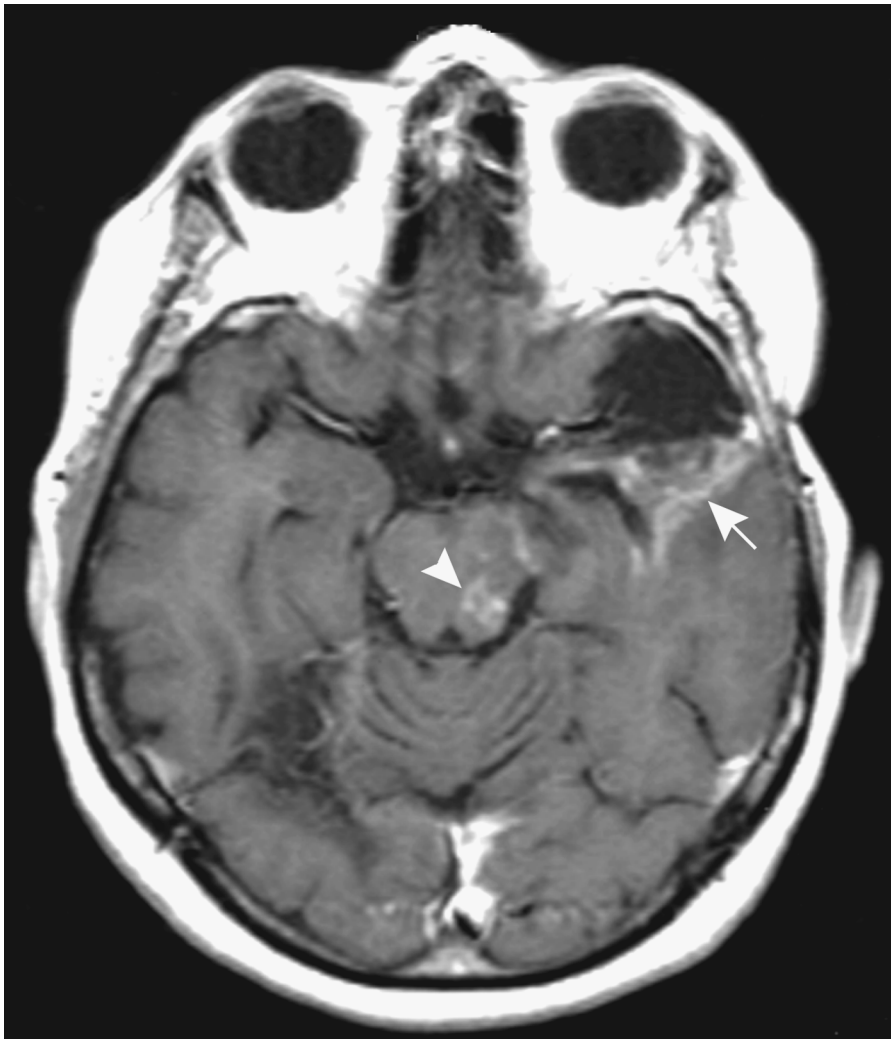


Figure 1-37. Post-contrast axial T₁-weighted MR image. Irregular enhancing lesions (arrow) posterior to the surgical cavity within the left temporal lobe and in the midbrain (arrowhead) were proved to be radiation necrosis at autopsy. The patient was status postsurgery with accelerated radiation therapy and chemotherapy for an anaplastic astrocytoma.

terminated (e.g., from the signal intensity change in an intracranial artery) then the rCBV can be converted to rCBF using the central volume theorem, $rCBF = rCBV/MTT$.

The second MR technique used for assessing cerebral microvascular changes requires no exogenous contrast agent. This technique, known as *arterial spin tagging* (AST), relies on time-of-flight signal loss in an imaging section that occurs from inversion of flowing spins in a section a few centimeters away (Detre et al., 1992; Edelman et al., 1994; Alsop and Detre, 1996). The inverted spins from the “tagged” sec-

tion yield decreased signal intensity when imaged in the section of interest. Knowing the location of the tagging section, the T₁ relaxation times in the section of interest, and the blood–tissue partition coefficient (approximately constant with a value of ~0.9), rCBF can be computed in the section of interest. The totally noninvasive nature of the AST rCBF measures makes this approach more advantageous than the DSC approach described above. The signal-to-noise ratio of the DSC technique is significantly higher, however, and obtaining good-quality AST measures of rCBF from multiple sections is more difficult due to mag-

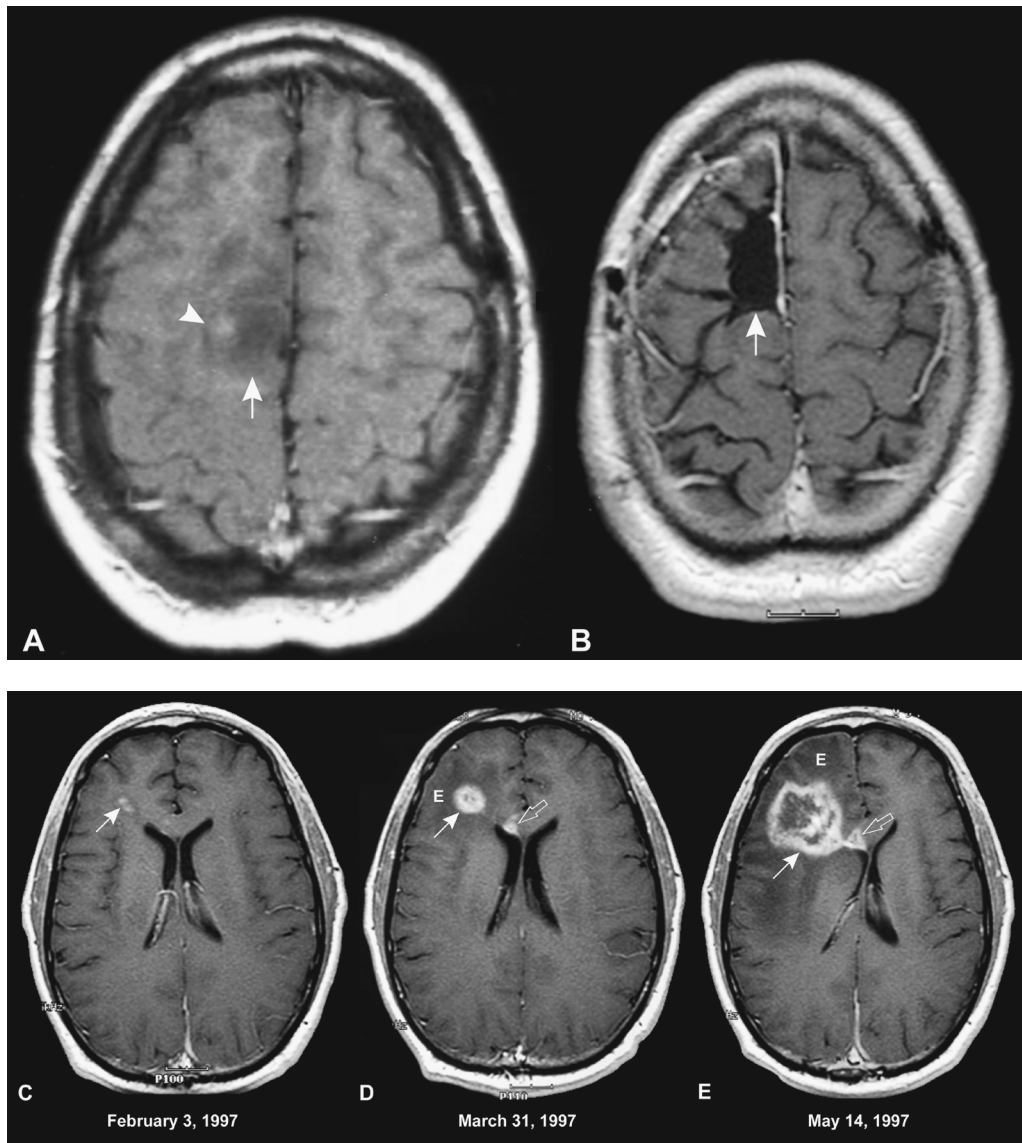


Figure 1-38. Post-contrast MR images (A-E). A nonenhancing tumor (arrow) with an enhancing nodule (arrowhead) occupying the right frontal lobe high-convexity region was noted in a 29-year-old male (A). The tumor was resected (resection cavity is shown in B, arrow). The tumor was an oligodendroglioma, and the patient was treated with radiation therapy (RT) and chemotherapy. The patient developed a small enhancing lesion in the right frontal lobe 8 months after completion of RT (arrow in C) that progressively increased in size in follow-up studies (arrows in D and E). There is also a progressive increase in the degree of edema (E) and mass effect on the right lateral ventricle. Surgical excision of the mass at this point revealed extensive radiation necrosis. Radiation necrosis affecting the corpus callosum is also shown (open arrows in D and E). Note that the radiation necrosis within the right frontal lobe (C-E) occurred remotely from the primary tumor (A).

netization transfer effects. Because of the lower signal-to-noise ratio, obtaining AST acquisitions is currently more time consuming than obtaining DSC acquisitions. More recent ultra-high-field systems, with

static magnetic fields at or greater than 3 Tesla, however, may provide adequate AST signal-to-noise ratios in scan times that begin to rival those required for current DSC techniques.

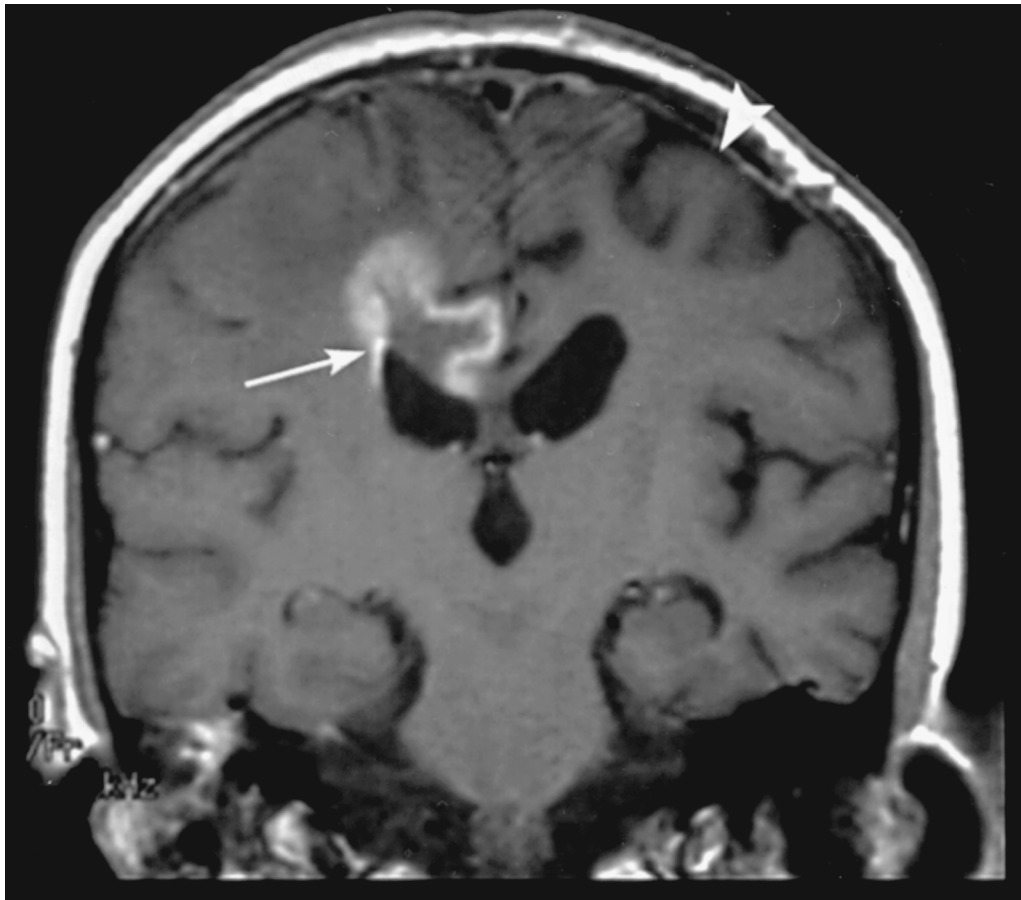


Figure 1–39. Post-contrast coronal T₁-weighted MRI of the brain. Biopsy-proven radiation necrosis affected the contralateral hemisphere (arrow) and involved the corpus callosum (C). The patient was status post-resection of glioblastoma in the left frontal lobe (arrowhead points to craniotomy site) followed by radiation and chemotherapy.

It should be noted that both the DSC and AST techniques for mapping rCBV and/or rCBF require very rapid imaging capabilities. Typically, this is best achieved using systems capable of single-shot, spin-echo, echo-planar imaging (EPI) techniques, which allow image acquisition rates as high as 50 msec/image.

Dynamic Contrast Magnetic Resonance Imaging Techniques

The use of static pre- and post-contrast agent-enhanced MR scans has been routine in neuroimaging since the mid-1980s. However, the kinetics of contrast agent uptake are infrequently used. The rapid acquisition of T1W images before, during, and after

the infusion of a bolus of paramagnetic contrast agent, however, allows the rates of contrast agent uptake and washout between a lesion and the vasculature to be assessed. In theory, simple two-compartment pharmacokinetic modeling of the contrast agent kinetics can be used to (1) map the fractional plasma volume (vascular volume), (2) determine endothelial transfer coefficient (permeability–surface area product) when contrast leakage is not flow rate limited, (3) assess extraction-flow product when leakage is great enough to be flow limited (Tofts, 1997), and (4) obtain the contrast agent reflux rate. Such non-invasive measures of vascular endothelial parameters might be highly useful in determining the penetration of novel chemotherapeutic agents, assessing the efficacy of novel antiangiogenic agents, and more specif-

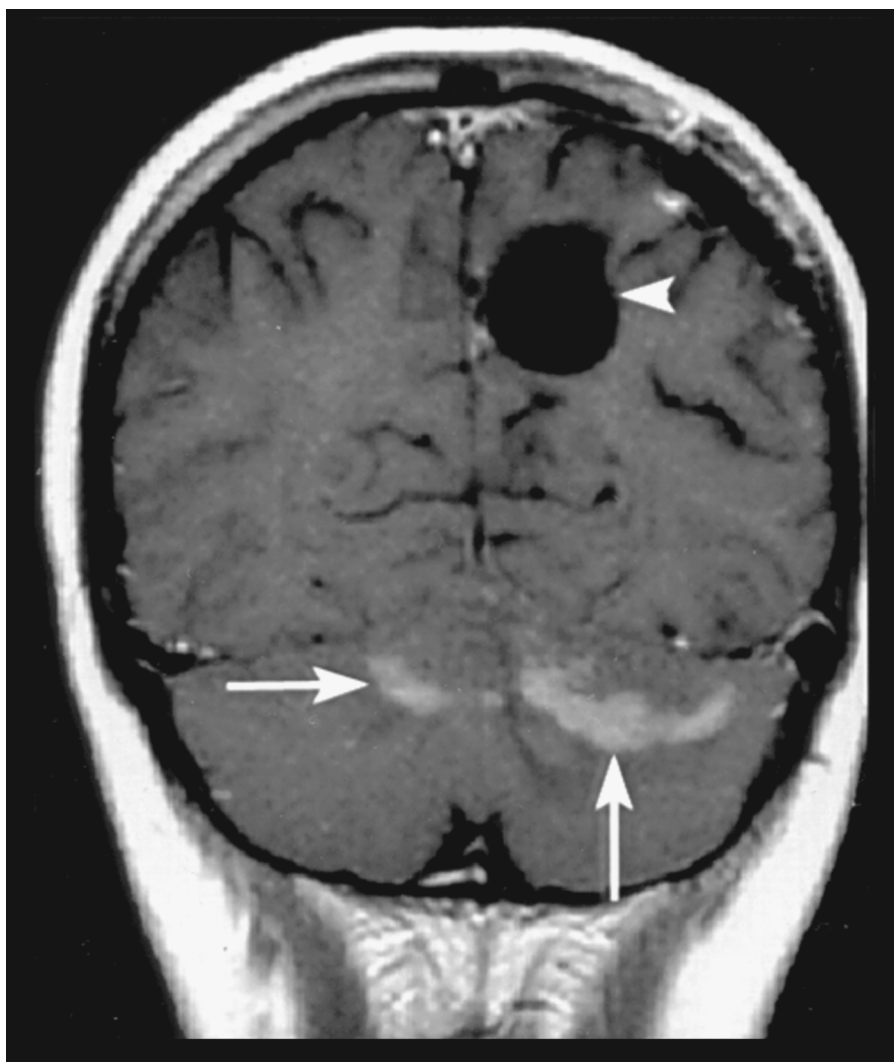


Figure 1-40. Post-contrast coronal T₁-weighted MRI of the brain shows radiation necrosis of the cerebellar hemispheres (arrows) that developed after resection of a parietal lobe glioblastoma and accelerated radiation therapy with chemotherapy to the brain (arrowhead points to the surgical cavity).

ically characterizing lesions in a noninvasive manner (e.g., differentiating between tumor progression and treatment-related changes).

Qualitative or semiquantitative applications of dynamic contrast agent-enhanced MRI to neuroimaging of patients with intracranial neoplasms have been previously reported. The utility of such scans in differentiating treatment-related changes from primary brain tumors, metastases, and meningiomas has been previously described (Hazle et al., 1997), and significant correlations between outcome measures and dy-

namic contrast MRI measures in anaplastic astrocytoma and glioblastoma multiforme patients have been reported by Wong et al. (1998). In addition to these studies based on empirical modeling of the dynamic data, several pharmacokinetic studies have been reported in which the endothelial transfer coefficient, contrast reflux rate, and fractional plasma volume have been determined (Larsson et al., 1990; Tofts and Kermode, 1991; Tofts, 1997; Parker and Tofts, 1999). When such calculations are performed on a pixel-by-pixel basis, the rapidly acquired source images can

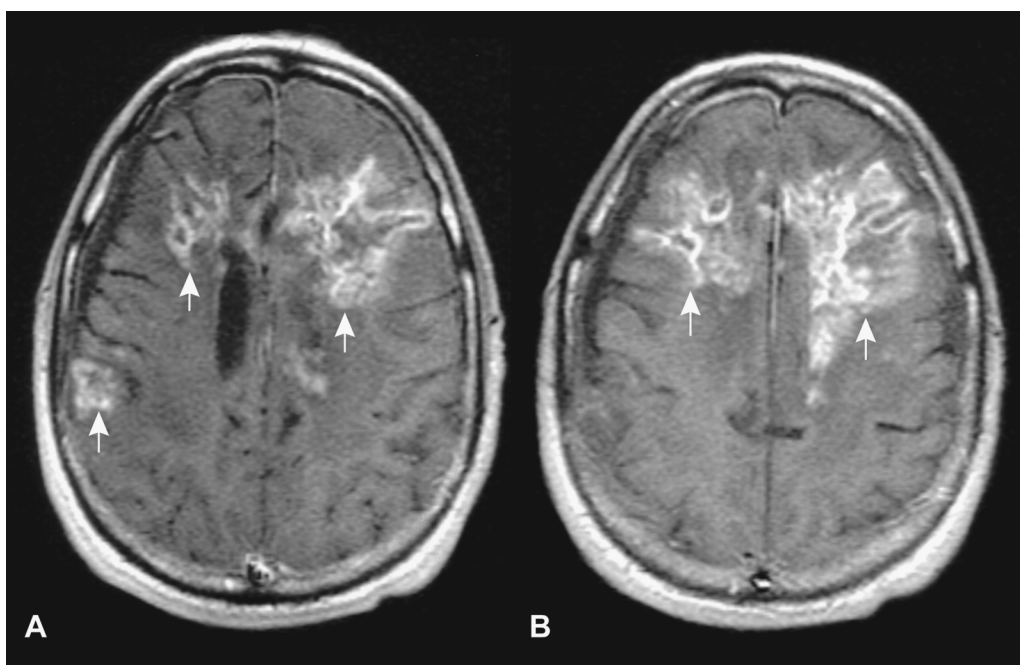


Figure 1-41. Post-contrast coronal T₁-weighted MR images (A,B) of the brain show extensive heterogeneous enhancing lesions involving both frontal lobes (arrows) with “Swiss cheese”-like interior, produced by radiation necrosis. Despite the large sized lesions, there is no mass effect secondary to involution of the brain. The patient was status postsurgery with accelerated radiation therapy and chemotherapy for a right frontal lobe anaplastic astrocytoma.

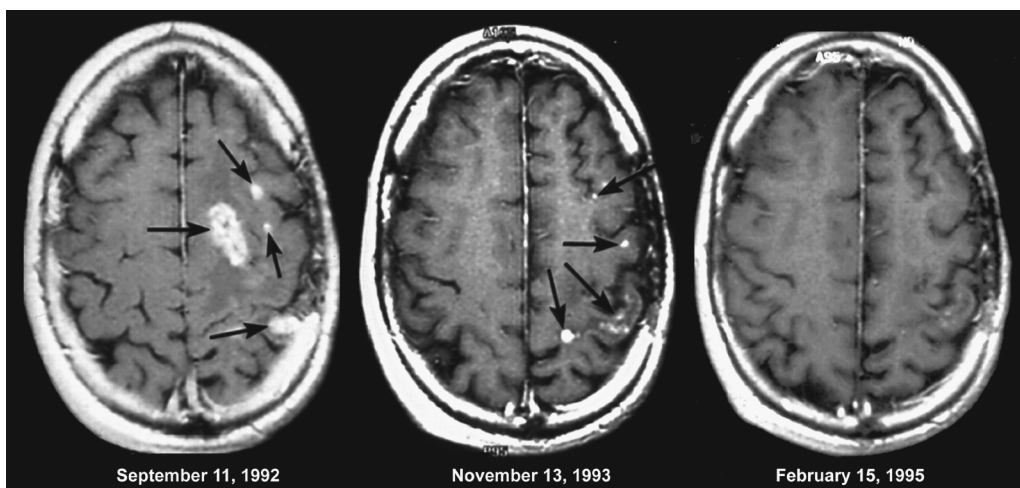


Figure 1-42. Post-contrast axial T₁-weighted MR images of the brain show spontaneous regression of radiation-induced enhancing lesions (arrows) within lesions in the left frontoparietal lobe. The patient is status postsurgery with accelerated radiation therapy and chemotherapy for a nonenhancing anaplastic astrocytoma involving the parietal lobe.

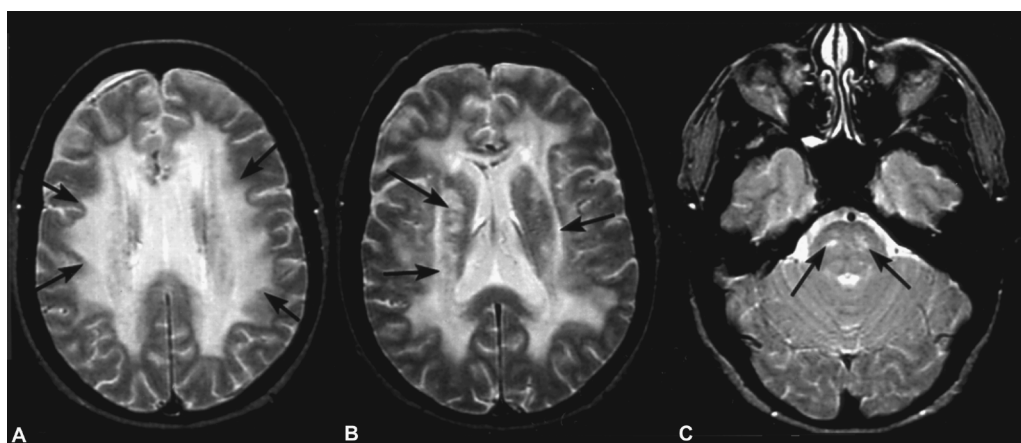


Figure 1-43. Axial T₂-weighted images (A–C) of the brain demonstrate radiation- and chemotherapy-induced periventricular leukoencephalopathy affecting the white matter (arrows in A) and two tracts (arrows in B and C).

be used to generate maps of each of the above parameters (Parker et al., 1997). Such *parametric maps* allow for improved assessment of lesion heterogeneity, thereby avoiding the potential for “sampling error,” which is commonly a point of concern in histopathologic analyses of tissue samples. Examples of parametric maps of fractional plasma volume and endothelial transfer coefficient in a patient with pathologically proven anaplastic astrocytoma are shown in Color Figure 1-47.

As with perfusion imaging techniques, dynamic contrast agent-enhanced scans require rapid image acquisition rates, particularly to obtain fractional plasma volume measures. Furthermore, if accurate measures of permeability–surface area product are desired, contrast agents with larger molecular weights than those currently available may be required for lesions associated with significant BBB breakdown. Otherwise, as mentioned above, contrast agent extravasation may be flow limited, leading to possible erroneous permeability–surface area measurements. As an example, extracranial lesion studies in animals have previously demonstrated improved correlations between permeability–surface area product and fractional plasma volume with histopathologic results when using higher molecular weight agents (~90,000 daltons) compared with FDA-approved low molecular weight agents (~600 daltons) (Daldrup et al., 1998).

Diffusion Imaging Techniques

If appropriate gradient pulses are applied within the echo time of a spin-echo EPI sequence, the resulting image contrast can be made to depend strongly on the rate of diffusion, or Brownian motion, of the nuclear spins of interest. The larger the area under the applied diffusion-sensitizing gradients, the greater the influence of diffusion on the image contrast. This area is directly related to the often-quoted “*b*-factor” value. More specifically, the degree of attenuation of the signal from a given tissue in diffusion-weighted images is proportional to e^{-bD} , where *b* is the *b*-factor value and *D* is the diffusion coefficient. Thus, for a given *b*-factor, larger diffusion coefficient levels are associated with larger degrees of signal attenuation. Similarly, for a given diffusion coefficient level, the degree of signal attenuation increases with increasing values of *b*. Therefore, in *diffusion-weighted images*, regions where diffusion is more restricted are hyperintense relative to regions of unrestricted diffusion.

In general, to obtain the degree of diffusion sensitization necessary for acceptable image contrast, the *b*-factor values must be rather large (e.g., 1000 sec/mm²). Therefore, the areas of the diffusion-sensitizing gradient pulses are large, and the minimum echo time is relatively long, resulting in T2W source image contrast. Because the images are T2W, substances with long T₂ values may not be as hy-



Figure 1-44. Radiation-induced mineralizing microangiopathy in a 13-year-old girl who underwent resection of an astrocytoma of the vermis followed by 45 Gy to the posterior fossa and 30 Gy to the whole brain. The patient developed multifocal calcifications 3 years after treatment. Non-contrast axial CT scan of the brain at that time revealed dense calcifications involving the basal ganglion (arrows) and subcortical white matter (arrowheads).

pointense as expected based solely on the rate of diffusion, resulting in “T₂ shine-through” of such substances in the diffusion-weighted images. To remove such confounding shine-through effects, image contrast may be based on the “apparent diffusion coefficient” (or ADC) (Le Bihan et al., 1992; Le Bihan and Turner, 1993; Sanders and Orrison, 1995). The ADC images are computed from a set of diffusion-weighted

images obtained with multiple (~ 2 to 5), *b*-factor values. Of note is the fact that the contrast on *ADC*-weighted images is the inverse of the contrast obtained on diffusion-weighted images; regions where diffusion is restricted are hypointense, and regions where diffusion is unrestricted are hyperintense.

Of importance also is the fact that diffusion in some tissues is anisotropic (Moseley et al., 1990). For ex-

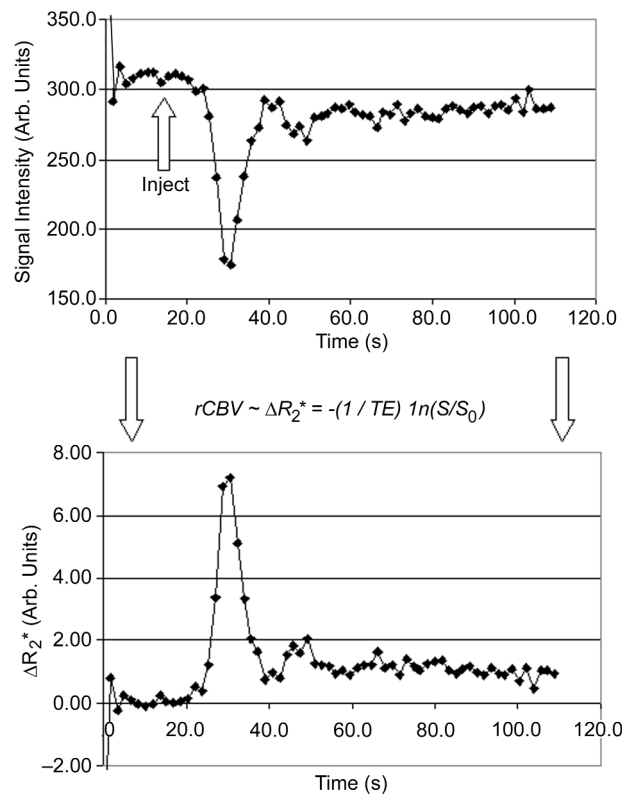


Figure 1-45. Dynamic susceptibility contrast (DSC) regional cerebral blood volume (rCBV) mapping. **(Top)** A typical signal intensity versus time curve from a region of interest in the parietal cortex. Note the dramatic signal loss in the cortex during the bolus transit and the recovery to baseline following the first pass. **(Bottom)** The change in signal intensity can be converted to a change in apparent T_2 relaxation rate (ΔR_2^*). Because $rCBV \propto [Gd] \propto \Delta R_2^*$, the regional cerebral blood volume can then be determined (see Ostergaard et al., 1996b, for complete details.)

ample, diffusion along white matter tracts is much less restricted than diffusion across the tracts (Fig. 1-48). Therefore, if diffusion-sensitizing gradient pulses are applied only in one direction, it is difficult to know if signal variations in the image plane are due to true differences in diffusion rates or to white matter diffusion anisotropy. To remove this confound, diffusion-sensitizing gradients are typically applied in each of the three orthogonal directions, and the results are averaged together to yield the average or “trace” diffusion-weighted image in which the anisotropic diffusion rate information is suppressed (Fig. 1-48). On the other hand, the fact that white matter tract diffusion is anisotropic does allow the use of diffusion tensor imaging techniques for non-invasively mapping the white matter tracts (Fig. 1-49)

(Pierpaoli et al., 1996; Pajevic and Pierpaoli, 1999; Virta et al., 1999).

Thus far, the primary clinical application of diffusion imaging has been the detection of acute stroke (van Gelderen et al., 1994; Sorensen and Rosen, 1996; Beauchamp et al., 1998). On diffusion-weighted images, areas of restricted extracellular water diffusion, secondary to increased cellular volume, appear hyperintense in acute ischemic injury. These signal changes have been shown to occur well before detectable changes occur on T2W or FLAIR images and have been useful in the detection and staging of ischemic injury. Coupled with perfusion imaging techniques, diffusion imaging techniques might permit assessment of the ischemic penumbra and assist in treatment decisions using current and novel stroke

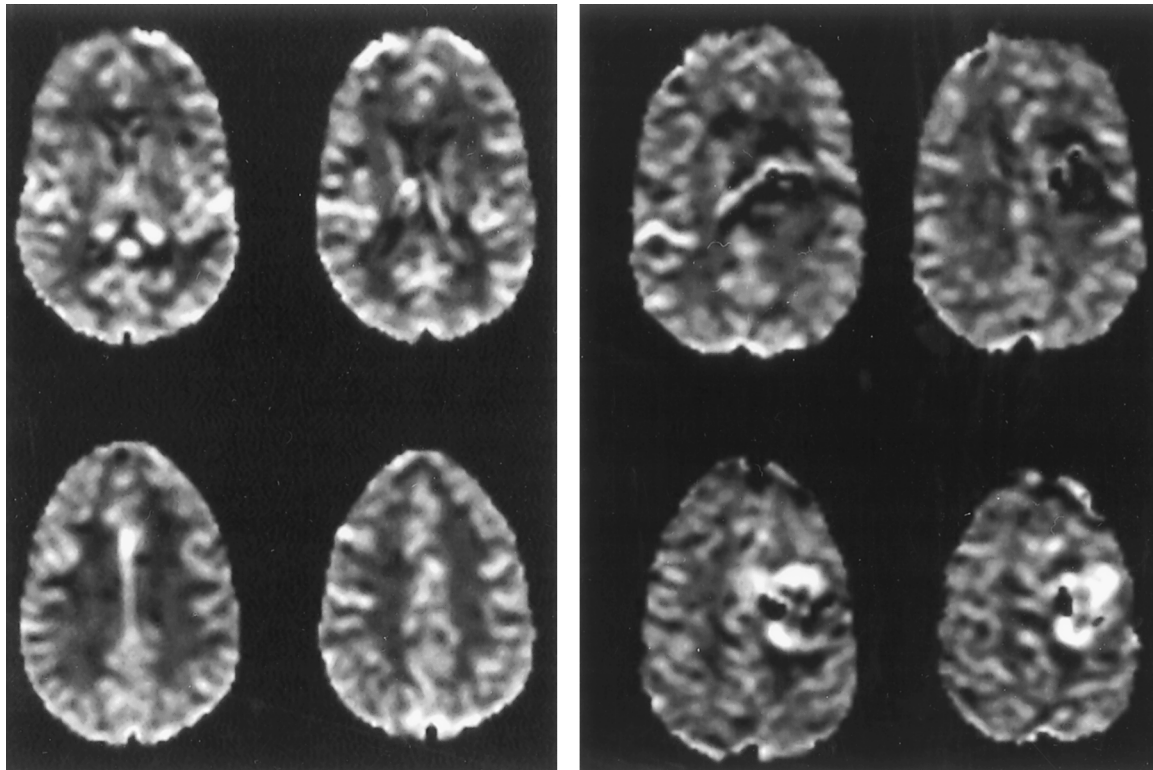


Figure 1-46. Dynamic susceptibility contrast (DSC) regional cerebral blood volume (rCBV) maps showing normal perfusion contrast (**left**) and increased rCBV (**right**) in a patient with pathologically proven anaplastic astrocytoma (right).

therapies (Beauchamp et al., 1998). Furthermore, quantitative diffusion imaging, by providing a means of noninvasively assessing the degree of cellularity (Chenevert et al., 1997), may prove useful in improved characterization of intracranial lesions.

As with perfusion imaging techniques, diffusion imaging requires very high-speed imaging capabilities. In fact, of all of the current advanced neuroimaging techniques, diffusion imaging is the most demanding of the MR scanner hardware. The large gradient field pulses push the limit of even state-of-the-art scanners and typically require relatively long echo times, potentially increasing the T_2 shine-through problem. Furthermore, the large amplitude of rapidly switched gradient field pulses requires good eddy current compensation performance to prevent unacceptable levels of artifact. (Eddy currents induced in the surrounding metallic components in the magnet give rise to transient magnetic fields that oppose the applied gradient fields and limit the speed with which the images can be acquired without sub-

stantial artifacts.) Typically, single-shot, spin-echo EPI sequences are used for diffusion imaging to capture the small-scale motion represented by the diffusion process in a background of larger scale motions due to involuntary and voluntary patient motion and motion due to CSF pulsation.

Functional Imaging of Neuronal Task Activation

Before recent developments in MRI, the only image modality that was capable of imaging areas of neuronal function was PET. Other techniques for mapping areas of activation (e.g., electroencephalography [EEG] and magnetoencephalography [MEG]), were not image based, and spatial localization of the activated areas was coarse, at best. In 1991 and 1992, two new functional MRI (fMRI) techniques for indirectly mapping areas of neuronal activation in response to a visual stimulus were reported (Belliveau et al., 1991; Kwong et al., 1992). The underlying phys-

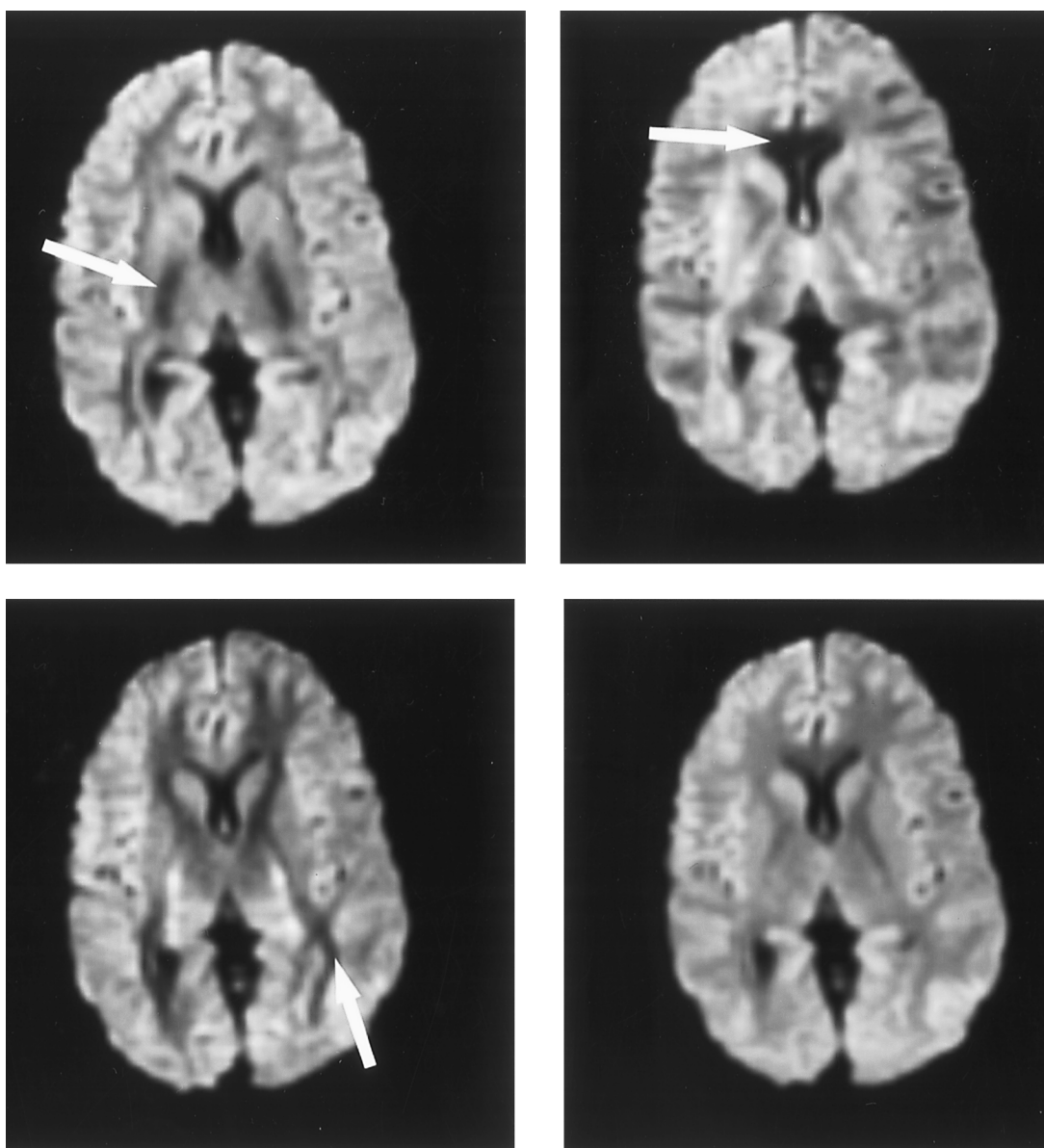


Figure 1-48. Diffusion-weighted MR images with diffusion-sensitizing gradients applied in the superoinferior (**top left**), right-left (**top right**), and anteroposterior (**bottom left**) directions. Note the dramatic differences in image appearance due to the anisotropic nature of water diffusion within the white matter tracts (arrows). Signal intensity is hypointense in directions of less restricted diffusion (along the tracts). The trace image (**lower right**) does not exhibit such anisotropic effects.

iologic principle of both techniques is that the neuronal activation that occurs in response to a stimulus, such as a visual task, results in local vasodilatation and a concomitant local increase in rCBV and rCBF. The first fMRI technique used to map this increase was the bolus contrast agent-enhanced DSC

perfusion imaging acquisition discussed previously. First, a resting rCBV map was acquired. Then, during a given functional task, a second bolus of contrast agent was administered and a second rCBV map was obtained. The difference in the two images provided a map of areas of the brain that exhibited increased

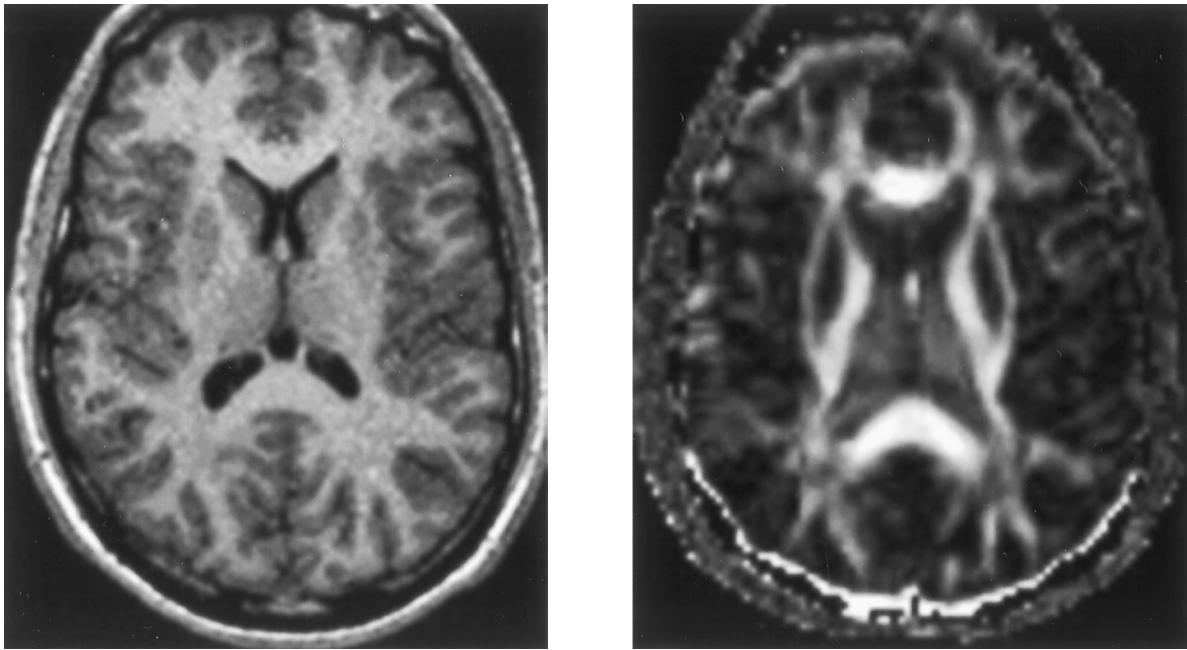


Figure 1-49. Diffusion tensor imaging to depict white matter tracts. **(Left)** T1W image. **(Right)** MR "tractogram."

rCBV during the task. The advantage of the DSC fMRI technique is that the signal intensity change between rest and activation is approximately 30% at 1.5 Tesla. The disadvantage of this technique is that it requires two contrast agent infusions per set of functional images and limits the number of tasks that can be evaluated in a single imaging session as well as how soon sessions can be repeated.

The second fMRI technique is based on *blood oxygen level dependent* (BOLD) contrast and is currently the most commonly used approach for imaging areas of neuronal activation. In this technique, no exogenous contrast agent is administered. Instead, advantage is made of the fact that deoxyhemoglobin is a paramagnetic substance and oxyhemoglobin is a diamagnetic substance. As noted with the DSC perfusion imaging technique, paramagnetic substances cause increased dephasing of the MR signal on T2W or T2*W images due to susceptibility effects. On the other hand, diamagnetic substances have minimal effect on signal dephasing. Therefore, a given amount of deoxyhemoglobin (paramagnetic) results in more signal loss relative to the same amount of oxyhemoglobin (diamagnetic). In regions of neuronal activation, local increases in rCBV and rCBF result in local increases in the oxyhemoglobin concentration, and,

as shown by previous PET studies (Fox and Raichle, 1986), the rate of oxygen extraction is significantly less than the rate of oxyhemoglobin delivery. Therefore, in areas of activation, there is a net increase in the oxyhemoglobin/deoxyhemoglobin ratio and a concomitant increase in signal intensity on T2W and T2*W images.

The key advantages of this technique are that it is totally noninvasive and the resolution of the resulting activation maps is on the order of 1.5 to 2.0 mm, significantly better than those obtained using PET. However, the change in signal intensity at 1.5 Tesla is only about 1% to 3%, requiring excellent stability of the MR scanner and well-designed test paradigms and signal processing strategies. (The BOLD signal increases supralinearly with field strength, and much of the recent interest in 3 and 4 Tesla scanners stems primarily from the improved BOLD signal response relative to 1.5 Tesla scanners.)

Since the publication of the first fMRI studies of neuronal function in 1991, there have been many reports of BOLD fMRI studies for widely varying applications, including studies of visual stimulation, auditory stimulation, memory, language, sensorimotor stimulation, psychiatric disorders, and pain (e.g., Sanders and Orrison, 1995; Sorensen and Rosen,

1996; Buckner and Koutstaal, 1998; Tootell et al., 1998; Turner et al., 1998; and references therein). Examples of fMRI mapping for presurgical planning purposes are given in Color Figure 1–50.

In Vivo Spectroscopic Techniques

One of the earliest practical applications of the nuclear magnetic resonance phenomenon was the determination of chemical structure based on MR spectral data. It is not surprising, therefore, that investigators began developing and attempting to apply in vivo MR spectroscopy (MRS) techniques to whole-body scanners as soon as they were commercially available (in the mid-1980s). Clinical MRS applications have, however, lagged significantly behind rapidly advancing imaging capabilities. Nevertheless, the promise of being able to obtain biochemical information in a completely noninvasive manner continues to drive the transition of in vivo MRS from a research tool to a clinical application. Furthermore, many of the advances in scanner hardware that have allowed imaging techniques to evolve from a means of obtaining purely anatomic information to a means of obtaining physiologic information have also greatly improved MRS capabilities on state-of-the-art scanners.

It is well beyond the scope of this section to provide detailed descriptions of the acquisition, processing, and clinical applications of in vivo MRS. Instead, each of these topics is briefly reviewed and references are made to the rather extensive literature available on these subjects.

There are three basic requirements for performing an in vivo MRS examination on a clinical imaging system. First, an appropriate non-zero spin nucleus must be selected, and the system must be capable of transmitting and receiving signals at the frequency appropriate for the chosen nucleus of interest. Although it is theoretically possible to obtain MRS data from a range of different nuclei in the human body, natural abundance and relative MR sensitivity considerations generally limit clinical applications to ^1H and ^{31}P studies. The second basic requirement is a means of accurately localizing the region from which the MRS data are obtained. Numerous localization schemes have been proposed, but the most commonly used techniques in clinical applications are the single voxel (SV) technique and the spectroscopic imaging (SI) technique (Fig. 1–51). In the SV technique, spectral

data are acquired from a single volume of interest (VOI) at a time. (An SV ^1H spectrum from a patient with glioblastoma multiforme is shown in Fig. 1–52.) On the other hand, SI techniques acquire spectral data from a number of VOIs simultaneously.

Both techniques have advantages and disadvantages. For example, one key criterion for obtaining good quality spectral data is that the magnetic field in the VOI is highly uniform. The magnetic field homogeneity can typically be better optimized on a small volume of tissue, like the VOI in an SV acquisition, than the larger volume typically examined using SI techniques. The SI technique, however, allows for obtaining spectra from multiple VOIs that are individually much smaller than an SV VOI, thereby permitting assessment of the heterogeneity of a given lesion and surrounding tissue. Furthermore, low-resolution “metabolite maps” can be computed from the SI data, allowing visualization of the spatial distribution of various compounds (Color Figs. 1–53 and 1–54). An additional requirement of the chosen acquisition technique, at least for ^1H MRS acquisitions, is the ability to suppress the signal from water, as the concentrations of the compounds of interest are typically 5000 to 10,000 times less than the concentration of water.

The third basic requirement for clinical MRS examinations is a means of analyzing the spectral data. Spectral data can be analyzed in three primary ways. The first is visual inspection of the spectral peaks—clearly the simplest, but most highly subjective, method to implement. The second commonly used method is to form ratios of spectral peak heights, or areas, with respect to a chosen reference peak. With ^1H brain spectra, for example, the most common reference peak is the creatine/phosphocreatine resonance, which varies minimally with spatial position within the brain. This approach is more quantitative and less subjective than the visual inspection method. In disease processes, however, changes in spectral peak ratios may reflect concentration changes in the compound of interest, in the reference compound, or in both.

The third method for analyzing spectral data is to obtain absolute metabolite concentrations from the associated spectral peak areas. Although obviously the most objective technique, this method of analysis is notoriously difficult. To convert from peak areas to absolute concentration requires a reference peak from a compound with known concentration. This

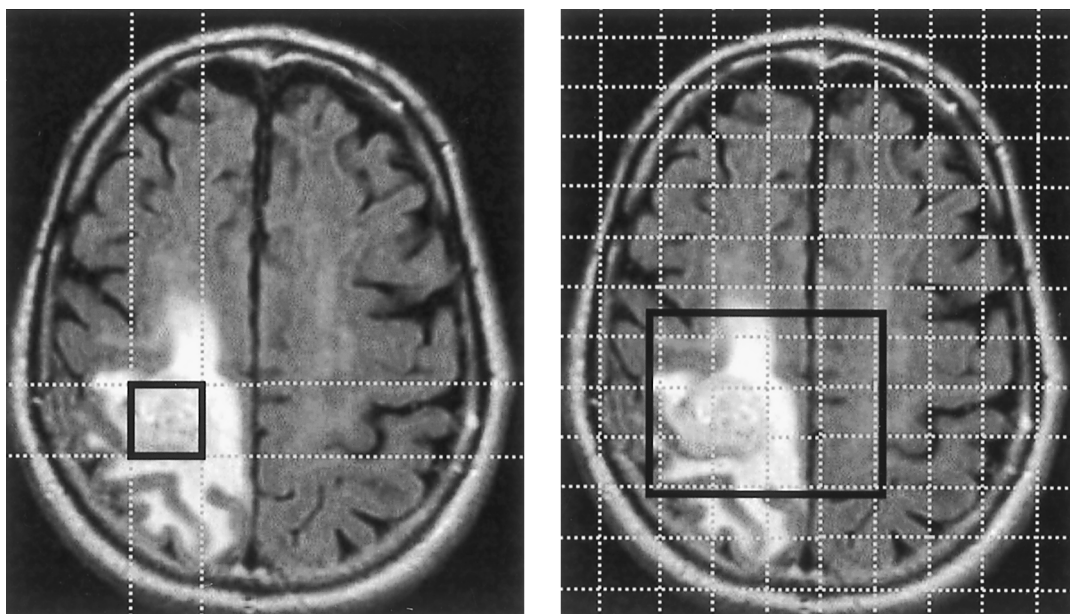


Figure 1-51. Proton MRS localization techniques. **(Left)** Single voxel (SV) technique used to acquire spectral data from one volume of at a time. The intersection of three planes, defined by the through-plane slice and two orthogonal “slices” (dotted lines), defines the VOI (black square). **(Right)** Spectroscopic imaging (SI) technique used to obtain spectral data from multiple VOIs in a single acquisition. Typically, a large volume is initially defined as in the SV technique (black rectangle). Phase-encoding techniques are then used to obtain individual spectra from multiple VOIs within the large volume of interest.

reference compound may be either an internal—most commonly water—or an external standard from which a spectrum is obtained just before or just after in vivo MRS data acquisition. The internal standard approach may be problematic in disease states where the internal reference compound concentra-

tion changes, whereas in the external standard approach it can be difficult to position and obtain a spectrum from the reference standard under the same conditions that occurred during in vivo MRS acquisition. Given the lack of objectivity of the visual inspection technique and the inherent difficulties of the

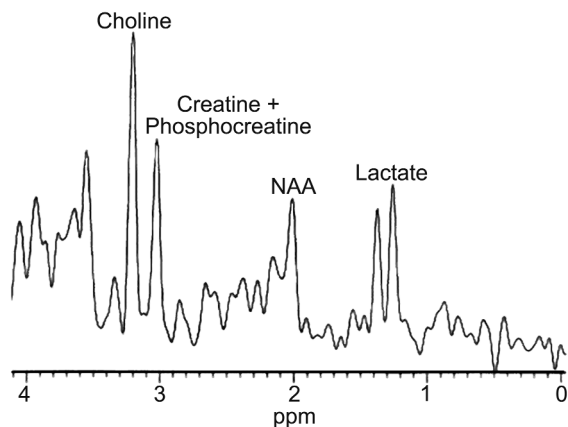


Figure 1-52. SV spectrum (echo time = 30 ms, repetition time = 2000 ms) from a glioblastoma multiforme showing greatly decreased levels of *N*-acetylaspartate, elevated lactate, and elevated choline.

absolute concentration technique, many investigators have settled on spectral peak ratios as the method of choice for routine analysis of spectral data. Because the T_1 and T_2 relaxation times of the various compounds of interest vary, however, it should be noted that the spectral peak heights, areas, and ratios depend strongly on echo time (TE) and, to a lesser degree, on repetition time (TR). Therefore, when comparing spectral data to literature values or between examinations, it is most important to take the TE and TR values into account. Several review articles and texts describe the wide range of clinical applications of in vivo MRS (Cady, 1990; Negendank, 1992; Barker et al., 1993; Howe et al., 1993; Ross and Michaelis, 1994, 1996; Vion-Dury et al., 1994; Cox, 1996; Falini et al., 1996; Danielsen and Ross, 1999; Jackson, 1999; Nelson et al., 1999).

Although many research investigations using both ^1H and ^{31}P MRS, as well as other less abundant nuclei, have been reported, undoubtedly the most common clinical application is ^1H MRS of the brain. In a normal human brain spectrum, the most prominent spectral peak is due to *N*-acetylaspartate (NAA). Although the exact biochemical role of NAA has yet to be fully elucidated, it is present in abundance only in viable neurons (Birken and Oldendorf, 1989). Reductions in the normal levels of NAA are sensitive indicators of neuronal degradation, but are nonspecific. The next most prominent spectral peaks in the normal brain spectrum are due to creatine/phosphocreatine and choline-containing compounds. Less prominent peaks due to *myo*-inositol and, for short TE spectra, glutamate/glutamine, are also visible. Lactate peaks are typically below detection limits in normal brain tissue, but may be visible in disease states, including ischemic injury and some neoplasms. Spectral peaks from lipids, abundant in the myelin, are not seen in normal brain due to the rigid structure of the lipids within the myelin. In some disease states, however, lipid peaks and peaks from macromolecular breakdown products may be present in spectra acquired with short echo times. (The effective T_2 relaxation times of these breakdown products are relatively short, resulting in the absence of peaks in spectra such as are acquired with long echo times.) In neoplastic lesions, the most common findings are elevated levels of choline-containing compounds, decreased levels of creatine/phosphocreatine, and decreased levels of NAA. Lactate peaks may, or may not, be present. Therefore, using the spectral peak ratio

method of analysis, the most common finding in neoplastic lesions is elevated choline/creatine and choline/NAA ratios relative to normal brain tissue levels. Treatment-related changes, such as radiation necrosis, do not typically demonstrate such highly elevated choline/creatine ratios and are often associated with the presence of peaks due to lipids and other macromolecular breakdown products (in short TE spectra).

Outside of the brain, the most common clinical oncologic application of in vivo MRS has been in the prostate, where the level of citrate in ^1H spectra has been used to differentiate between benign prostate hyperplasia and neoplasm (Hahn et al., 1997; Heerschap et al., 1997; Liney et al., 1999).

Summary of Advanced MRI Techniques

In the last 5 years, significant improvements in MR scanner technology have allowed for new neuroimaging techniques, which have changed MRI from a means of acquiring images with exquisite anatomic detail and soft tissue contrast to a means of acquiring images of tissue function. Whereas many of these functional imaging techniques are currently in a transitional stage from basic research to clinical practice, several are poised to make a significant impact on clinical patient management and outcome. Newer imaging techniques, including more specific contrast agents and novel image contrast mechanisms, will undoubtedly continue to propel the expanding use of MRI in neuroimaging applications. In addition, significant improvements in automated SV and SI in vivo MRS data acquisition and processing techniques have allowed for "routine" acquisition of biochemical information that can be used, for example, to aid in the often difficult differentiation between tumor progression and treatment-related changes.

REFERENCES

- Alsop DC, Detre JA. 1996. Reduced transit-time sensitivity in noninvasive magnetic resonance imaging of human cerebral blood flow. *J Cereb Blood Flow Metab* 16:1236–1249.
- Ball WS, Jr, Prenger EC, Ballard ET. 1992. Neurotoxicity of radio/chemotherapy in children: pathologic and MR correlation. *Am J Neuroradiol* 13:761–776.
- Barker PB, Glickson JD, Bryan RN. 1993. In vivo magnetic resonance spectroscopy of human brain tumors. *Top Magn Reson Imaging* 5:32–45.

- Beauchamp NJ, Jr, Ulug AM, Passe TJ, van Zijl PC. 1998. MR diffusion imaging in stroke: review and controversies. *RadioGraphics* 18:1269–1283.
- Belliveau JW, Kennedy DN, Jr, McKinstry RC, et al. 1991. Functional mapping of the human visual cortex by magnetic resonance imaging. *Science* 254:716–719.
- Birken DL, Oldendorf WH. 1989. *N*-acetyl-L-aspartic acid: a literature review of a compound prominent in ^1H -NMR spectroscopic studies of brain. *Neurosci Biobehav Rev* 13:23–31.
- Blood CH, Zetter BR. 1990. Tumor interactions with vasculature angiogenesis and tumor metastasis. *Biochim Biophys Acta* 1032:89–118.
- Buckner RL, Koutstaal W. 1998. Functional neuroimaging studies of encoding, priming, and explicit memory retrieval. *Proc Natl Acad Sci USA* 95:891–898.
- Burger PC, Boyko OB. 1991. The pathology of central nervous system radiation injury. In: Gutin PH, Leibel SA, Sheline GE (eds), *Radiation Injury to the Nervous System*. New York: Raven Press, p 191.
- Burger PC, Mahley MS, Jr, Dudka L, Vogel FS. 1979. The morphologic effects of radiation administered therapeutically for intracranial gliomas: a postmortem study of 25 cases. *Cancer* 44:1256–1272.
- Cady EB. 1990. *Clinical Magnetic Resonance Spectroscopy*. New York: Plenum Press, 278 pp.
- Castel JC, Caille JM. 1989. Imaging of irradiated brain tumours. Value of magnetic resonance imaging. *J Neuroradiol* 16:81–132.
- Chenevert TL, McKeever PE, Ross BD. 1997. Monitoring early response of experimental brain tumors to therapy using diffusion magnetic resonance imaging. *Clin Cancer Res* 3:1457–1466.
- Choucair AK, Levin VA, Gutin PH, et al. 1986. Development of multiple lesions during radiation therapy and chemotherapy in patients with gliomas. *J Neurosurg* 65:654–658.
- Cowley AR. 1983. Influence of fiber tracts on the CT appearance of cerebral edema: anatomic pathologic correlation. *AJNR (Am J Neuroradiol)* 4:915–925.
- Cox IJ. 1996. Development and applications of in vivo clinical magnetic resonance spectroscopy. *Prog Biophys Mol Biol* 65:45–81.
- Daldrup H, Shames DM, Wendland M, et al. 1998. Correlation of dynamic contrast-enhanced MR imaging with histologic tumor grade: comparison of macromolecular and small-molecular contrast media. *AJR (Am J Roentgenol)* 171:941–949.
- Danielsen ER, Ross BD. 1999. Clinical cases. In: Danielsen ER, Ross B (eds), *Magnetic Resonance Spectroscopy Diagnosis of Neurological Diseases*. New York: Marcel Dekker, pp 53–302.
- Davis PC, Hudgins PA, Peterman SB, Hoffman JC, Jr. 1991. Diagnosis of cerebral metastases: double dose delayed CT vs contrast-enhanced MR imaging. *AJNR (Am J Neuroradiol)* 12:293–300.
- Detre JA, Leigh JS, Williams DS, Koretsky AP. 1992. Perfusion imaging. *Magn Reson Med* 23:37–45.
- Doyle WK, Budinger TF, Valk PE, Levin VA, Gutin PH. 1987. Differentiation of cerebral radiation necrosis from tumor recurrence by ^{18}F FDG and ^{82}Rb positron emission tomography. *J Comput Assist Tomogr* 11(4):563–570.
- Ebner F, Ranner G, Slavic I et al. 1989. MR findings in methotrexate induced CNS abnormalities. *AJR (Am J Roentgenol)* 153:1283–1288.
- Edelman RR, Siewert B, Darby DG, et al. 1994. Qualitative mapping of cerebral blood flow and functional localization with echo-planar MR imaging and signal targeting with alternating radio frequency. *Radiology* 192:513–520.
- Elster AD, Chen MY. 1992. Can nonenhancing white matter lesions in cancer patients be disregarded? *AJNR (Am J Neuroradiol)* 13:1309–1318.
- Falini A, Calabrese G, Origgi D, et al. 1996. Proton magnetic resonance spectroscopy and intracranial tumours: clinical perspectives. *J Neurol* 243:706–714.
- Fike JR, Sheline GE, Cann CE, David RL. 1984. Radiation necrosis. *Prog Exp Tumor Res* 28:136–151.
- Fox PT, Raichle ME. 1986. Focal physiological uncoupling of cerebral blood flow and oxidative metabolism during somatosensory stimulation in human subjects. *Proc Natl Acad Sci USA* 83:1140–1144.
- Frank JA, Gorton M, Dwyer AJ, et al. 1987. Ocular and cerebral metastases in the VX2 rabbit tumor model: contrast-enhanced MR imaging. *Radiology* 164:527–530.
- Hahn P, Smith IC, Leboldus L, Littman C, Somorjai RL, Bezabeh T. 1997. The classification of benign and malignant human prostate tissue by multivariate analysis of ^1H magnetic resonance spectra. *Cancer Res* 57:3398–3401.
- Hazle JD, Jackson EF, Schomer DF, Leeds NE. 1997. Dynamic imaging of intracranial lesions using fast spin-echo imaging: differentiation of brain tumors and treatment effects. *J Magn Reson Imaging* 7:1084–1093.
- Heerschap A, Jager GJ, van der Graaf M, et al. 1997. In vivo proton MR spectroscopy reveals altered metabolite content in malignant prostate tissue. *Anticancer Res* 17:1455–1460.
- Heier LA, Zimmerman RD. 1992. Commentary: can nonenhancing white matter lesions be disregarded? *Am J Neuroradiol* 13:1316.
- Hoffman WF, Levin VA, Wilson CB. 1979. Evaluation of malignant glioma patients during the postirradiation period. *J Neurosurg* 50:624–628.
- Howe FA, Maxwell RJ, Saunders DE, Brown MM, Griffiths JR. 1993. Proton spectroscopy in vivo. *Magn Reson Q* 9:31–59.
- Jackson EF. 1999. Magnetic resonance spectroscopy: physical principles and applications. In: Kim EE, Jackson EF (eds), *Molecular Imaging in Oncology: PET, MRI, and MRS*. Berlin: Springer, pp 47–70.
- Kumar AJ, Leeds NE, Fuller GN, et al. 2000. Malignant gliomas: MR imaging spectrum of radiation therapy- and chemotherapy-induced necrosis of the brain after treatment. *Radiology* 217:377–384.
- Kwong KK, Belliveau JW, Chesler DA, et al. 1992. Dynamic magnetic resonance imaging of human brain activity during primary sensory stimulation. *Proc Natl Acad Sci USA* 89:5675–5679.
- Kyritsis AP, Levin VA, Yung WK, Leeds NE. 1993. Imaging patterns of multifocal gliomas. *Eur J Radiol* 16:163–170.
- Larsson HB, Stubgaard M, Frederiksen JL, Jensen M, Henriksen O, Paulson OB. 1990. Quantitation of blood-brain barrier defect by magnetic resonance imaging and gadolinium-DTPA in patients with multiple sclerosis and brain tumors. *Magn Reson Med* 16:117–131.
- Le Bihan D, Turner R. 1993. Diffusion and perfusion nuclear magnetic resonance imaging. In: Potchen EJ, Haacke EM,

- Siebert JE, Gottschalk A (eds), *Magnetic Resonance Angiography. Concepts and Applications*. St Louis: Mosby Year Book, pp 323–342.
- Le Bihan D, Turner R, Dovek P, Patronas N. 1992. Diffusion MR imaging: clinical applications. *AJR (Am J Roentgenol)* 159:591–599.
- Levin VA, Maor MH, Thall PF, et al. 1995. Phase II study of accelerated fractionation radiation therapy with carboplatin followed by vincristine chemotherapy for the treatment of glioblastoma multiforme. *Int J Radiat Oncol Biol Phys* 33:357–364.
- Liney GP, Turnbull LW, Knowles AJ. 1999. In vivo magnetic resonance spectroscopy and dynamic contrast enhanced imaging of the prostate gland. *NMR Biomed* 12:39–44.
- Marks JE, Baglan RJ, Prassad SC, Blank WF. 1981. Cerebral radionecrosis: incidence and risk in relation to dose, time, fractionation and volume. *Int J Radiat Oncol Biol Phys* 7:243–252.
- Moody DM, Bell MA, Challa VR. 1990. Features of the cerebral vascular pattern that predict vulnerability to perfusion or oxygenation deficiency: an anatomic study. *AJNR (Am J Neuroradiol)* 11:431–439.
- Moseley ME, Cohen Y, Kucharczyk J. 1990. Diffusion-weighted MR imaging of anisotropic water diffusion in cat central nervous system. *Radiology* 176:439–445.
- Negendank W. 1992. Studies of human tumors by MRS: a review. *NMR Biomed* 5:303–324.
- Nelson MD, Jr, Gonzalez-Gomez I, Gilles FH. 1991. Dyke award. The search for human telencephalic ventriculofugal arteries. *AJNR (Am J Neuroradiol)* 12:215–222.
- Nelson SJ, Vigneron DB, Dillon WP. 1999. Serial evaluation of patients with brain tumors using volume MRI and 3D ¹H MRSI. *NMR Biomed* 12:123–138.
- Ostergaard L, Sorensen AG, Kwong KK, Weisskoff RM, Gyldensted C, Rosen BR. 1996a. High resolution measurement of cerebral blood flow using intravascular tracer bolus passages. Part II: Experimental comparison and preliminary results. *Magn Reson Med* 36:726–736.
- Ostergaard L, Weisskoff RM, Chesler DA, Gyldensted C, Rosen BR. 1996b. High resolution measurement of cerebral blood flow using intravascular tracer bolus passages. Part I: Mathematical approach and statistical analysis. *Magn Reson Med* 36:715–725.
- Pajevic S, Pierpaoli C. 1999. Color schemes to represent the orientation of anisotropic tissues from diffusion tensor data: application to white matter fiber tract mapping in the human brain. *Magn Reson Med* 42:526–540.
- Parker GJ, Suckling J, Tanner SF, et al. 1997. Probing tumor microvasculature by measurement, analysis and display of contrast agent uptake kinetics. *J Magn Reson Imaging* 7:564–574.
- Parker GJ, Tofts PS. 1999. Pharmacokinetic analysis of neoplasms using contrast-enhanced dynamic magnetic resonance imaging. *Top Magn Reson Imaging* 10:130–142.
- Pierpaoli C, Jezzard P, Basser PJ, Barnett A, Di Chiro G. 1996. Diffusion tensor MR imaging of the human brain. *Radiology* 201:637–648.
- Ross B, Michaelis T. 1994. Clinical applications of magnetic resonance spectroscopy. *Magn Reson Q* 10:191–247.
- Ross B, Michaelis T. 1996. MR spectroscopy of the brain: neurospectroscopy. In: Edelman RR, Hesselink JR, Zlatkin M (eds), *Clinical Magnetic Resonance Imaging*. Philadelphia: WB Saunders, pp 928–981.
- Sanders JA, Orrison WW, Jr. 1995. Functional magnetic resonance imaging. In: Orrison WW, Jr, Lewine JD, Sanders JA, Hartshorne MF (eds), *Functional Brain Imaging*. St Louis: Mosby Year Book, pp 239–326.
- Schorner W, Laniado M, Niendorf HP, Schubert C, Felix R. 1986. Time-dependent changes in image contrast in brain tumors after gadolinium-DTPA. *AJNR (Am J Neuroradiol)* 7:1013–1020.
- Sorensen AG, Rosen BR. 1996. Functional MRI of the brain. In: Atlas SW (ed), *Magnetic Resonance Imaging of the Brain and Spine*. New York: Raven Press, pp 1501–1545.
- Sorensen AG, Tievsky AL, Ostergaard L, Weisskoff RM, Rosen BR. 1997. Contrast agents in functional MR imaging. *J Magn Reson Imaging* 7:47–55.
- Sze G, Milano E, Johnson C, Heier L. 1990. Detection of brain metastases: comparison of contrast-enhanced MR with unenhanced MR and enhanced CT. *AJNR (Am J Neuroradiol)* 11:785–791.
- Sze G, Soletsky S, Bronen R, Krol G. 1989. MR imaging of the cranial meninges with emphasis on contrast enhancement and meningeal carcinomatosis. *AJR (Am J Roentgenol)* 153:1039–1049.
- Tofts PS. 1997. Modeling tracer kinetics in dynamic Gd-DTPA MR imaging. *J Magn Reson Imaging* 7:91–101.
- Tofts PS, Kermode AG. 1991. Measurement of the blood–brain barrier permeability and leakage space using dynamic MR imaging. I. Fundamental concepts. *Magn Reson Med* 17:357–367.
- Tootell RB, Hadjikhani NK, Vanduffel W, et al. 1998. Functional analysis of primary visual cortex (V1) in humans. *Proc Natl Acad Sci USA* 95:811–817.
- Turner R, Howseman A, Rees GE, Josephus O, Friston K. 1998. Functional magnetic resonance imaging of the human brain: data acquisition and analysis. *Exp Brain Res* 123:5–12.
- Valk PE, Dillon WP. 1991. Radiation injury of the brain. *AJNR (Am J Neuroradiol)* 12:45–62.
- van Gelderen P, de Vleeschouwer MH, DesPres D, Pekar J, van Zijl PC, Moonen CT. 1994. Water diffusion and acute stroke. *Magn Reson Med* 31:154–163.
- Virta A, Barnett A, Pierpaoli C. 1999. Visualizing and characterizing white matter fiber structure and architecture in the human pyramidal tract using diffusion tensor MRI. *Magn Reson Imaging* 17:1121–1133.
- Vion-Dury J, Meyerhoff DJ, Cozzone PJ, et al. 1994. What might be the impact on neurology of the analysis of brain metabolism by in vivo magnetic resonance spectroscopy? *J Neurol* 241:354–371.
- Wong ET, Jackson EF, Hess KR, et al. 1998. Correlation between dynamic MRI and outcome in patients with malignant glioma. *Neurology* 50:777–781.
- Yuh WT, Engelken JD, Muhonen MG, Mayr NA, Fisher DJ, Erhardt JC. 1992. Experience with high-dose gadolinium MR imaging in the evaluation of brain metastases. *AJNR (Am J Neuroradiol)* 13:335–345.